ÉCOLE CENTRALE LYON

THESE de DOCTORAT DE L'UNIVERSITE DE LYON

opérée au sein de l'Ecole centrale de Lyon

École Doctorale MEGA
Spécialité Mécanique des Fluides

Donato Vallefuoco

Numerical study of unconfined and confined anisotropic turbulence

Jury:	P.-P. Cortet	Examinateur
	S. Galtier	Examinateur
	F.S. Godeferd	Directeur
	A. Naso	Examinatrice, co-encadrante
	Y. Ponty	Rapporteur
	P. Sagaut	Rapporteur
	J.F. Scott	Examinateur

Abstract

In turbulent flows of practical interest, turbulence interacts with confinement and external forces, leading to statistical inhomogeneity and anisotropy. Isolating their contributions to some targeted statistics is indispensable for understanding the underlying physical phenomena. The aim of this thesis has therefore been to gain further insight into direction- and scale-dependent anisotropy in a set of idealized and realistic contexts.

Both spectral space and separation space statistical characterizations have been employed. The spectral characterization concerns the anisotropic statistics of turbulence under the form of directional energy, polarization and helicity spectra. The separation space characterization is built on two-point second- and third-order velocity increment moments, and two-point velocity correlations.

First, we studied the effect of large-scale spectral forcing. The considered forcing methods are the non-helical and the helical Euler scheme, and the ABC-scheme. We showed that both forcings have a drawback in that, if the number of sufficiently excited modes is too low, anisotropy is bound to arise even at small scales. In the case of Euler forcing, this depends on both the range of forcing wavenumbers and its helicity contents. The ABC forcing, for which the amount of injected helicity cannot be controlled, excites only six modes and therefore always generates anisotropy at all resolved scales.

Our second step was to analyze the scale- and direction-dependent anisotropy of homogeneous rotating turbulence. Surprisingly, anisotropy arises at all scales even at low rotation rate. In particular, we identified two anisotropic ranges with different features. In the large scales, directional anisotropy is larger and decreases with wavenumber. At smaller scales, it is much weaker—although still significant—and slowly increases with wavenumber all the way to the dissipative scales. Another interesting and original conclusion of this part of the work concerns the role of the Zeman scale and its link with the flow scale-dependent anisotropy. The Zeman scale was previously argued to be the characteristic lengthscale separating rotation-affected scales

from isotropic ones. Upon closer investigation using several simulations at different parameters, we found that the separating scale between large and weak anisotropy is rather the characteristic lengthscale at which rotation and dissipation effects balance. This result, however, does not contradict Zeman's argument about isotropy recovery in the asymptotic limit of vanishing viscosity, since the separating scale vanishes at infinite Reynolds number, and therefore only the decreasing anisotropy range should persist and scales much smaller than the Zeman one may recover isotropy.

Finally, we considered the von Kármán flow between two counter-rotating bladed disks in a cylindrical cavity. We repeated the separation space analysis in different small sub-regions, in order to question the possible analogies in the flow dynamics with that of homogeneous rotating turbulence. We found that, in the regions of the domain where the mean flow has a larger average rotation rate, the distributions of the statistics in separation space display some of the features typical of rotating turbulence.

Résumé

Pour les écoulements turbulents d'intérêt pratique, la turbulence interagit avec le confinement et les forces externes, ce qui cause inhomogénéité et anisotropie statistiques. Isoler leur contributions à des statistiques ciblées est indispensable pour comprendre les différents phénomènes physiques. Le but de cette thèse a donc étè d'acquérir une meilleure connaissance de l'anisotropie en fonction de la direction et de l'échelle dans un ensemble de contextes idéalisés et réalistes.

On a utilisé une caractérisation statistique dans l'espace spectral ainsi que dans l'espace de séparation. Le caractérisation dans l'espace spectral concerne les statistiques anisotropes de turbulence sous forme de spectres directionnels d'énergie, polarisation et hélicité. La caractérisation dans l'espace de séparation s'appuie sur les moments des incréments de vitesse à deux points du deuxième et troisième ordre, et sur les corrélations de vitesse à deux points.

Tout d'abord, on a étudié l'effet du forçage spectral de grandes échelles. Les schémas de forçage considérés sont le schéma de forçage de type Euler, non hélicitaire et hélicitaire, et le schéma ABC. On a montré que les deux forçages ont un inconvénient, dans le sens que, si le nombre de modes suffisamment excités est petit, de l'anisotropie se produit même aux petites échelles. Dans le cas du forçage Euler, cela dépend de la gamme de nombres d'onde forcés ainsi que de leur hélicité. Le forçage ABC, pour lequel le niveau d'hélicité injectée ne peut pas être controlé, n'excite que six modes et donc il produit toujours de l'anisotropie et à toutes les échelles résolues.

Ensuite, on a analysé l'anisotropie en fonction de l'échelle et de la direction pour la turbulence homogène en rotation. Chose étonnante, l'anisotropie se produit à toutes les échelles même si la rotation est faible. En particulier, on a identifié deux gammes d'échelles anisotropes qualitativement différentes. Aux grandes échelles, l'anisotropie directionnelle est plus grande et décroit avec le nombre d'onde. Aux petites échelles, elle est beaucoup plus faible—mais encore significative—et croit lentement avec le nombre d'onde jusq'aux échelles dissipatives. Une autre conclusion intéressante et originale de cette partie du travail concerne le role de l'échelle de Ze-

man et son lien avec l'anisotropie aux différentes échelles de l'écoulement. D'après des travaux précédents, l'échelle de Zeman devrait être l'échelle de longueur caractéristique qui sépare les échelles affectées par la rotation par les échelles isotropes. Après une plus ample investigation, en utilisant simulations à differents paramètres, on a découvert que l'échelle de séparation entre grande et faible anisotropie est plutôt l'échelle de longueur caractéristique pour laquelle les effets de rotation et de dissipation s'équilibrent. Ce résultat, toutefois, n'est pas en contradiction avec l'argument de Zeman sur le rétablissement de l'isotropie dans la limite asymptotique de viscosité nulle, comme l'échelle de séparation s'annule à nombre de Reynolds infini, et donc seulement la gamme d'anisotropie décroissante devrait persister et les échelles beaucoup plus petite que celle de Zeman pourraient récupérer l'isotropie.

Enfin, on a considéré l'écoulement de von Kármán entre deux disques équipés de pales en contre-rotation dans une cavité cylindrique. On a répété l'analyse dans l'espace de separation dans plusieures petites sous-régions, afin d'inquêter les analogies possibles entre la dynamique de l'écoulement et celle de la turbulence homogène en rotation. On a découvert que, dans les régions du domain où l'écoulement a un taux de rotation moyen plus grand, les distributions des statistiques dans l'espace de séparation montrent certaines des caractéristiques typiques de la turbulence en rotation.

Acknowledgements

Firstly, I am grateful to my supervisor Fabien Godeferd and to Aurore Naso for these years of support and advice, their experience was fundamental to conduct this research. I would like to thank the jury members for their sharp questions and comments during the PhD defence, and in particular the two reviewers for having read and reviewed the manuscript. I also wish to thank my colleagues who took some time for discussions about turbulence and helped me broaden my scientific knowledge. A special thanks goes to my friends, who have always been a major source of moral support. The simulations were run on the local mesocenter of the *École centrale de Lyon*, a member of the *Fédération Lyonnaise de Modélisation et Simulation Numérique*, and on the supercomputer of CINES, the french national computing center of the Ministry of Research and Education, with a CPU grant allocated by GENCI.

Contents

Introduction

The understanding of turbulence is fundamental in a wide range of applications, including for instance atmospheric and oceanic currents, flows around vehicles, chemical reactors, and other engineering applications. These flows are usually highly complex and often involve mixed or coupled phenomena, so that a holistic approach is rarely possible. Complexity can come from their geometry, and some studies have shown that boundary layers can pilot to some extent the evolution of the inner turbulent flows. Complexity can also come from coupled phenomena, as for instance in flows of conducting fluid subject to a magnetic field inducing a Lorentz force. In geophysical flows, the coupling can be due to the presence of buoyancy effects due to density gradients, or from the action of the Coriolis force. In both cases, there exists a regime in which wave nonlinear interaction is the dominant means of transfering energy. Therefore, in a rotating system, the fluid dynamics may be realized by mixed phenomena due to inertial waves and turbulence. In rotating confined systems, wave reflection can add to the level of complexity, so that the global system can hardly be grasped as a whole.

A researcher is therefore faced with a series of challenges in order to progress in the understanding of such flows. They first need to find a suitable conceptual representation of the turbulent flow, second they seek to characterize it in a way which is necessarily oriented towards a chosen reduced objective, and thirdly they have to propose models that can serve both as practical tools but also for improving our understanding of the flow dynamics.

The theory of turbulence relies mostly on the representation proposed by Richardson [71] of the turbulent cascade from large to small scales until eventually dissipation takes over. This description therefore suggests a separation between the largest turbulent scales and the smallest ones, with an inertial range in between. This is further supported by the theory of Kolmogorov [39, 40] wherein the Reynolds number is assumed so large that there is a perfect decoupling between the reservoir of energy—the energy containing scales—and the dissipative scales whose size is of order of the Kolmogorov lengthscale. Actual flows do not abide strictly by this concep-

tual picture, since they are confined and their Reynolds numbers are not infinitely large, even not always *very* large. For instance, the $-4/5$-th law for the third-order moment of velocity increment is an important exact statistical result obtained in the framework of Kolmogorov theory; but the actual convergence towards the predicted value when the Reynolds number increases is rather slow, and values of order 10^6 have to be reached before a good approximation is obtained [3].

Another assumption linked with the theory of Kolmogorov is isotropy, so that statistics do not depend on spatial direction, and, for instance, a unique two-point velocity correlation lengthscale can be used to characterize the size of turbulent structures, whatever their orientation. In real-life turbulence, this condition is rarely met, and anisotropy is ubiquitous. In the above-mentioned example of flows subject to an external force, its direction introduces a symmetry breaking, and additional direction-dependent statistics are called for a good characterization of the phenomena.

In this work, we are therefore addressing questions relative to these two features of actual turbulent flows: how does the anisotropy of the large scales influence that of the smaller scales, in flows in which the Reynolds number is moderately large? In addition, considering the effect of solid body rotation on turbulence, what is the amount of anisotropy due to the Coriolis force? In so doing, we state that our model of turbulence is rather simple, since we forget about the physical confinement of the flow and we assume statistical homogeneity in space. Only in the last chapter do we relax this latter assumption in order to investigate a more complex flow and test our statistical characterization method on the von Kármán flow.

The second point is therefore the choice of a given characterization for rotating homogeneous forced turbulence. Since the rotation rate vector introduces a preferential direction, the flow is statistically axisymmetric and significant anisotropy can arise in the turbulent dynamics. From existing studies, we know that rotating turbulence often exhibits structures elongated along the axis of symmetry, so that one requires a means of quantifying their anisotropy. We will analyze scale- and direction-dependent anisotropy by computing two-point velocity correlation spectra and second- and third-order moments of the velocity increment. This permits to consider a separation vector or a wavevector with a given norm—hence the scale dependence—and orientation—hence the dependence with direction. The choice of these precise statistics stems from two ideas. First, spectra contain the same information as the correlation itself, but in spectral space modal decomposition is far easier than in separation space. It is desirable to project the two-point velocity spectral tensor on given modes in order to exhibit the presence of different kinds of anisotropy, and thus to provide a very fine tool for analyzing the structure of

the flow. This decomposition brings the directional energy, polarization and helicity spectra [73]. Second, considering velocity increments permits to relate our study to existing theoretical or experimental results. For instance, the above-mentioned $-4/5$-th law of third-order moments of velocity increment can be used as a reference to measure the departure of the anisotropic flow dynamics from the exact high Reynolds number isotropic state. Along with the second-order moment and two-point velocity correlation, the third-order moments also permit to compute all the terms in the Kármán-Howarth-Monin equation, as we propose in Chapter 4. Accessing all the terms that balance this equation provides an alternate way of considering the flow dynamics with respect to the Lin-type equation for the energy spectral density, which is the Fourier transform of the Kármán-Howarth-Monin equation. In both equations each term corresponds to a precise mechanism: dissipation, nonlinear transfer, forcing or time-derivative term. Evaluating these terms is the key for investigating the dynamics of rotating turbulence with an emphasis on anisotropy. Previous characterizations are oriented towards the specific action of inertial waves [32], or are more focused on inertial-range scalings of horizontal or vertical spectra [18], or on a more phenomenological approach based on inertial waves propagation [75]. Experimental results for the chosen statistics were obtained in an experiment of towed-grid turbulence in a tank [21]. These experiments provide a reference for comparison, although they do not give access to the full three-dimensional space-resolved quantities, since, as in all experiments, the metrology has limited capacities.

The third ingredient in our methodology is finally the chosen model of forced homogeneous rotating turbulence. We have mentioned theory and experiments, but we will concentrate here on simulations. We choose to perform Direct Numerical Simulations (DNS), using a pseudo-spectral method, so that all the scales of the flow are resolved. This said with respect to *e.g.* large eddy simulation, which is valuable for achieving higher Reynolds numbers, but at the price of parameterized small scales. In our numerical simulations we use a periodic domain which is appropriate for representing statistically homogeneous turbulence, and a statistically stationary state is reached by introducing an external working force. We use large-scale spectral forcing so that an energy cascade towards smaller scales develops, in agreement with the concept of Richardson cascade. We choose two kinds of forcing which have been used in previous studies, referred to as ABC and Euler [52, 68]. However, since only a finite number of low wavenumbers are excited in such a discretized approach, anisotropy may develop from the forcing itself, and interfere with other physical sources of anisotropy, here the effect of rotation. Therefore, the first concern of this thesis work will be to detect this kind of artificial anistropy in the above-

mentioned forcing schemes, and to identify the conditions that allow it to develop, as well as the affected scales. We will explore a variety of regimes of rotating turbulence, characterized by the Reynolds and Rossby numbers. We expect that large Rossby number flows will be less affected by rotation, while low Rossby number ones will respond with strong anisotropy to the distorsion caused by rotation. Thanks to the above-mentioned directional statistics, we will be able to characterize this reponse in a qualitative as well as quantitative way. Several results are expected from our study, some of which shall confirm existing results, but original findings will also be obtained. For instance, the Zeman lengthscale has been identified in previous studies to be a key lengthscale indicative of the presence or not of anisotropy in the flow structure at given scales [25, 53], but we find that another characteristic lengthscale is also relevant in the investigated regimes. Another very important object is the third-order vector moment in separation space, its divergence being the dual of the spectral energy transfer in Fourier space, which has been measured experimentally [21] or for which a theoretical inertial expression is proposed by [30]. We compute this quantity, compare it to its predictions, and explain how one can reconcile seemingly contradictory trends. Finally, and as a last sample of the coming analysis, we show from both the third-order vector moment and the modal spectral decomposition that anisotropy can extend throughout all scales.

Thanks to the versatility of the simulation platform, it is also possible to change the flow configuration almost at will to progress towards more and more complex flows, the limit being the available computational power. (For instance in this work, since several values of the parameters and flow configurations had to be investigated in order to scan a wide parametric space, resolutions as high as 1024^3 were used.) We have chosen to consider a flow which can be thought of being closer to a real flow. This von Kármán flow is the flow between two counter-rotating bladed disks and enclosed within cylindrical walls [43]. It is both anisotropic and inhomogeneous, but since it contains two large-scale toroidal vortices (inducing opposite average rotation rates in the upper and lower halfs), its features could be compared to the more academic flow of rotating homogeneous turbulence. In addition, helicity is injected in the flow through the blades—as it is injected in ABC- and Euler-forced simulations. We note that this helical character is very important in some flows, for instance flows of conducting fluids, there again increasing complexity. Therefore, the von Kármán flow seems to be a logical extension of our work towards more complex flows. Although it is not homogeneous, velocity statistics can nonetheless be computed in different small sub-domains, so that the effect of inhomogeneity on the computed quantities can be estimated. In the last chapter, we thus show that valuable infor-

mation about anisotropy in turbulence can be drawn when comparing the statistics of our two homogeneous and inhomogeneous flows, also in a perspective of comparing with other studies based on separation space statistics in inhomogeneous shear flow.

The thesis is organized as follows. In Chapter 1 we introduce the relevant statistical quantities and analytical relations of homogeneous turbulence, and we describe the anisotropic features of rotating turbulence. Special attention is put on two-point second- and third-order statistics, in spectral space as well as in the space of the separation vectors in physical space. We decompose the velocity spectral tensor in three contributions linked to energy, helicity and polarization spectral densities. The evolution equations of the velocity spectral tensor—*i.e.* Craya's equation—and of the velocity correlation in physical space—Kármán-Howarth-Monin equation—are derived. We also recall the inertial exact expressions of the third-order vector moment in separation space, for both isotropic and rotating turbulence. In Chapter 2, we present the adopted numerical approach: the numerical methods we use in our simulations and how we treat boundary conditions, the computation of the direction- and scale-dependent statistics aimed at detecting anistropy, and the implementation of the forcing methods we use, *i.e.* the non-helical and the helical Euler scheme, and the ABC scheme. In Chapter 3, the anisotropy unnaturally induced by the spectral forcing is investigated through DNS. The use of angle-dependent energy, helicity, and polarization spectra allows a direction- and scale-dependent estimate of anisotropy. Chapter 4 is dedicated to the study of the anisotropy naturally induced by the Coriolis force. Distributions in both spectral and separation spaces are employed to characterize anisotropy at different scales, and to investigate the role of the characteristic scales related to rotation. The numerical results are also compared to experiments by Cortet & Moisy [21] and to the inertial laws. Finally, in Chapter 5, we consider the von Kármán flow and perform a similar statistical analysis in separation space. Since the flow is inhomogeneous, different features emerge from this analysis in different regions of the fluid domain.

Chapter 1

Homogeneous turbulence and homogeneous rotating turbulence

In this chapter the statistical quantities and analytical relations used in the following chapters are introduced. In particular we describe homogeneous turbulence with no mean flow with particular emphasis on turbulence subject to a background rotation. First, Fourier analysis is used to study homogeneous turbulence and to derive some important classical results in spectral space. Particular attention is put on the spectral velocity tensor, which fully characterizes second-order velocity correlations, and its evolution equation, i.e. Craya's equation. We also introduce a modal decomposition of the velocity spectral tensor suitable for statistically axisymmetric turbulence. Then, the evolution equation of the velocity correlation in separation space—the Kármán-Howarth-Monin equation—is derived, and its link with the energy spectral density equation is enlightened. We also recall the well-known Kolmogorov four-thirds or four-fifths law. Next, we introduce the characteristic lengthscales of rotating turbulence and describe its anisotropic features in both spectral and separation spaces. Finally, we recall the inertial law—corresponding to the Kolmogorov four-thirds law in the isotropic case—valid for rotating turbulence under some assumptions.

1.1 Spectral approach

1.1.1 Fourier transform

The goal of Fourier approach is to analyze functions as linear combinations of complex exponential functions. This tool results to be central in the study of homogeneous turbulence, and

therefore it is worth recalling here the definition of Fourier transform and its properties. The vector velocity field $\boldsymbol{u}$ is a function of three spatial coordinates $\boldsymbol{x}$ (in addition to time), and its statistical properties do not depend on the position in space. Nevertheless, for the sake of simplicity, in this section only scalar functions with one independent variable are considered.

The Fourier integral, or Fourier transform, of a function $u(x)$ is defined as

$$\hat{u}(k) = \frac{1}{2\pi} \int u(x) \mathrm{e}^{-\mathrm{i}kx} \, \mathrm{d}x \tag{1.1}$$

(the integral is over all x). In order for this integral to exist some conditions are required. For example, one possible sufficient condition is $u(x)$ to be absolutely integrable. However, when we deal with homogeneous turbulence, the velocity field is defined over all space, does not tend to zero as $|\boldsymbol{x}|$ increases, and thus its (spatial) Fourier integral does not converge. Of particular interest is then the approach in which Fourier analysis is tackled through the generalised functions theory, see [47]. According to this approach, $u(x)$ is defined by means of a sequence of functions $u_n(x)$, with $u(x) = \lim_{n\to\infty} u_n(x)$, and with the members of this sequence such that their Fourier transforms exist. Therefore, the Fourier transform of $u(x)$ is defined as the limit of the Fourier transform of $u_n(x)$ as n tends to infinity. Following Mathieu and Scott [49]—in the context of homogeneous-turbulence spectral-analysis—the convergence issue can be more directly solved by defining a finite-range Fourier transform,

$$\hat{u}_{\mathcal{L}}(k) = \frac{1}{2\pi} \int_{-\mathcal{L}}^{\mathcal{L}} u(x) \mathrm{e}^{-\mathrm{i}kx} \, \mathrm{d}x, \tag{1.2}$$

and then taking the limit of infinite $\mathcal{L}$, if it exists. In this chapter we use spectral analysis together with this tool to prove important results about homogeneous turbulence. In any case—in the limit of infinitely large $\mathcal{L}$—the properties of finite-range Fourier-transform do not formally change with respect to the conventional transform properties. Some of these classical properties (intended to be valid in the limit of infinitely large $\mathcal{L}$) are listed below:

$$\widehat{\frac{\partial u}{\partial x}} = \mathrm{i}k\hat{u} \tag{1.3}$$

$$\widehat{uv} = \hat{u} * \hat{v} \tag{1.4}$$

where v is another function of x and $*$ stands for convolution product. Furthermore, if $u(x)$ is real valued

$$\hat{u}(-k) = \hat{u}^*(k) \tag{1.5}$$

where $\hat{u}^*$ is the complex conjugate of $\hat{u}$.

In the present chapter, finite-range Fourier transforms are indicated through both a hat and a subscript $\mathcal{L}$, while when the subscript $\mathcal{L}$ is missing the limit of infinitely large $\mathcal{L}$ has been taken.

The quantities we deal with in homogeneous turbulence, typically the components of the velocity field, are statistically homogeneous random real-valued functions. Therefore, we derive here two useful results involving correlations that will be used in the next sections.

First, consider the ensemble averages $C(r) = \langle u(x)v(x+r)\rangle$ (if homogeneity holds, C depends only on r) and $\langle \hat{u}^*_{\mathcal{L}}(k)\hat{v}_{\mathcal{L}}(k)\rangle$, where now $u(x)$, $v(x)$ and their finite-range transforms are random functions. By definition (1.2) one can write

$$\langle \hat{u}^*_{\mathcal{L}}(k)\hat{v}_{\mathcal{L}}(k)\rangle = \left\langle \frac{1}{2\pi}\int_{-\mathcal{L}}^{\mathcal{L}} u(x)\mathrm{e}^{\mathrm{i}kx}\,\mathrm{d}x \frac{1}{2\pi}\int_{-\mathcal{L}}^{\mathcal{L}} v(x')\mathrm{e}^{-\mathrm{i}kx'}\,\mathrm{d}x' \right\rangle \tag{1.6}$$

$$= \frac{1}{(2\pi)^2}\int_{-\mathcal{L}}^{\mathcal{L}}\int_{-\mathcal{L}}^{\mathcal{L}} \langle u(x)v(x')\rangle\,\mathrm{e}^{-\mathrm{i}k(x'-x)}\,\mathrm{d}x'\,\mathrm{d}x. \tag{1.7}$$

By the change of variable $x' = x + r$

$$\langle \hat{u}^*_{\mathcal{L}}(k)\hat{v}_{\mathcal{L}}(k)\rangle = \frac{1}{(2\pi)^2}\int_{-\mathcal{L}}^{\mathcal{L}}\int_{-(x+\mathcal{L})}^{\mathcal{L}-x} \langle u(x)v(x+r)\rangle\,\mathrm{e}^{-\mathrm{i}kr}\,\mathrm{d}r\,\mathrm{d}x \tag{1.8}$$

and defining

$$\hat{C}_{\mathcal{L}}(k) = \frac{1}{2\pi}\int_{-(x+\mathcal{L})}^{\mathcal{L}-x} C(r)\mathrm{e}^{-\mathrm{i}kr}\,\mathrm{d}r \tag{1.9}$$

Eq. (1.8) becomes

$$\langle \hat{u}^*_{\mathcal{L}}(k)\hat{v}_{\mathcal{L}}(k)\rangle = \frac{\mathcal{L}}{\pi}\hat{C}_{\mathcal{L}}(k). \tag{1.10}$$

Note that, because of the modified limits of integration in Eq. (1.9), $\hat{C}_{\mathcal{L}}(k)$ is not exactly a finite-range Fourier-transform as defined by Eq. (1.2). However, if u and v decorrelate sufficiently rapidly as $r \to \infty$, and in the limit of infinite $\mathcal{L}$, both $\hat{C}_{\mathcal{L}}(k)$ and the finite-range transform of $C(r)$ tend to the conventional Fourier transform $\hat{C}(k)$.

Second, consider three random functions, say $u(x)$, $v(x)$ and $w(x)$, and write the averaged product of their transforms at wavenumbers $-k$, q, and $k-q$, $\langle \hat{u}_{\mathcal{L}}(-k)\hat{v}_{\mathcal{L}}(q)\hat{w}_{\mathcal{L}}(k-q)\rangle$. A procedure similar to the one used to derive Eq. (1.10) leads to

$$\langle \hat{u}_{\mathcal{L}}(-k)\hat{v}_{\mathcal{L}}(q)\hat{w}_{\mathcal{L}}(k-q)\rangle = \frac{1}{(2\pi)^3}\int_{-\mathcal{L}}^{\mathcal{L}}\int_{-(x+\mathcal{L})}^{\mathcal{L}-x}\int_{-(x+\mathcal{L})}^{\mathcal{L}-x} S(r,r')\mathrm{e}^{-\mathrm{i}qr}\mathrm{e}^{-\mathrm{i}(k-q)r'}\,\mathrm{d}r'\,\mathrm{d}r\,\mathrm{d}x \tag{1.11}$$

where

$$S(r,r') = \langle u(x)v(x+r)w(x+r')\rangle \tag{1.12}$$

and finally

$$\langle \hat{u}_{\mathcal{L}}(-k)\hat{v}_{\mathcal{L}}(q)\hat{w}_{\mathcal{L}}(k-q)\rangle = \frac{\mathcal{L}}{\pi}\hat{\hat{S}}_{\mathcal{L}}(q,k-q) \tag{1.13}$$

where $\hat{\hat{S}}_{\mathcal{L}}$ is the finite-range double transform of S, *i.e.*

$$\hat{\hat{S}}(q,k-q) = \frac{1}{(2\pi)^2}\iint S(r,r')\mathrm{e}^{-\mathrm{i}qr}\mathrm{e}^{-\mathrm{i}(k-q)r'}\,\mathrm{d}r'\,\mathrm{d}r. \tag{1.14}$$

Note that Eqs. (1.10) and (1.13) are special cases of more general results, *i.e.*

$$\langle \hat{u}^*_{\mathcal{L}}(k)\hat{v}_{\mathcal{L}}(k')\rangle = \delta_{\mathcal{L}}(k-k')\hat{C}_{\mathcal{L}}(k) \tag{1.15}$$

and

$$\langle \hat{u}_{\mathcal{L}}(k)\hat{v}_{\mathcal{L}}(k')\hat{w}_{\mathcal{L}}(k'')\rangle = \delta_{\mathcal{L}}(k+k'+k'')\hat{\hat{S}}_{\mathcal{L}}(k',k'') \tag{1.16}$$

(for details see Mathieu and Scott [49]), where the function

$$\delta_{\mathcal{L}}(k) = \frac{\sin(k\mathcal{L})}{\pi k} \tag{1.17}$$

tends to Dirac's delta as $\mathcal{L}$ increases.

1.1.2 Spectral velocity tensor

Given the space- and time-dependent random vector velocity field $u_i(\boldsymbol{x},t)$, the two-point velocity correlation tensor is defined as

$$R_{ij}(\boldsymbol{r},t) = \langle u_i(\boldsymbol{x},t)u_j(\boldsymbol{x}+\boldsymbol{r},t)\rangle, \tag{1.18}$$

where $\boldsymbol{x} = (x_1,x_2,x_3)$ is the Cartesian coordinate in physical space, $\boldsymbol{r}$ is the separation vector, t is time and $\langle\,\rangle$ represents ensemble averaging. Note that, because of statistical homogeneity, R_{ij} does not depend on $\boldsymbol{x}$. If R_{ij} tends to zero sufficiently rapidly as $|\boldsymbol{r}|$ increases, we can consider its Fourier transform, the velocity spectral tensor

$$\hat{R}_{ij}(\boldsymbol{k}) = \frac{1}{(2\pi)^3}\iiint R_{ij}(\boldsymbol{r})\mathrm{e}^{-\mathrm{i}\boldsymbol{k}\cdot\boldsymbol{r}}\mathrm{d}^3\boldsymbol{r} \tag{1.19}$$

(for simplicity, we drop here the dependence upon time t). From definition (1.18), the incompressibility condition $\nabla\cdot\boldsymbol{u} = 0$ implies $\partial R_{ij}(\boldsymbol{r})/\partial r_j = 0$ (the Einstein summation convention is used here), which by property (1.3) leads to $\hat{R}_{ij}(\boldsymbol{k})k_j = 0$. Furthermore, since $R_{ij}(\boldsymbol{r})$ is real

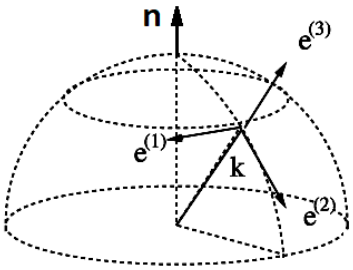

Figure 1.1: Craya-Herring frame of reference.

and $R_{ij}(\boldsymbol{r}) = R_{ji}(-\boldsymbol{r})$ from its definition and homogeneity, $\hat{R}_{ij}(\boldsymbol{k})$ is a Hermitian tensor, *i.e.* $\hat{R}^*_{ij}(\boldsymbol{k}) = \hat{R}_{ji}(\boldsymbol{k})$.

When dealing with statistically axisymmetric turbulence, it is useful to project the tensor $\hat{R}_{ij}$ onto a polar-spherical orthonormal basis $\{\boldsymbol{e}^{(1)},\boldsymbol{e}^{(2)},\boldsymbol{e}^{(3)}\}$ defined from the vector $\boldsymbol{n}$ bearing the axis of symmetry, with

$$\boldsymbol{e}^{(1)} = \frac{\boldsymbol{k}\times\boldsymbol{n}}{|\boldsymbol{k}\times\boldsymbol{n}|}, \quad \boldsymbol{e}^{(2)} = \boldsymbol{e}^{(3)}\times\boldsymbol{e}^{(1)}, \quad \boldsymbol{e}^{(3)} = \frac{\boldsymbol{k}}{k}, \tag{1.20}$$

which is the so-called Craya-Herring frame [22], and is illustrated in Fig. 1.1. $\boldsymbol{e}^{(1)}$ and $\boldsymbol{e}^{(2)}$ are referred to as *toroidal* and *poloidal* directions, respectively. From here on, $\boldsymbol{n}$ will be assumed to be in the x_3 direction (or to be "vertical"), without loss of generality. By enforcing incompressibility and Hermitian symmetry

$$\hat{R}_{ij}(\boldsymbol{k}) = \Phi^1(\boldsymbol{k})\boldsymbol{e}^{(1)}\boldsymbol{e}^{(1)} + \Phi^{12}(\boldsymbol{k})\boldsymbol{e}^{(1)}\boldsymbol{e}^{(2)} + \Phi^{12*}(\boldsymbol{k})\boldsymbol{e}^{(2)}\boldsymbol{e}^{(1)} + \Phi^2(\boldsymbol{k})\boldsymbol{e}^{(2)}\boldsymbol{e}^{(2)} \tag{1.21}$$

where $\Phi^1/2$ and $\Phi^2/2$ are the toroidal and the poloidal energy spectral densities.

The kinetic energy spectral density is defined as the Fourier transform of $\frac{1}{2}R_{ii}(\boldsymbol{r})$,

$$e(\boldsymbol{k}) = \frac{1}{(2\pi)^3}\iiint \frac{1}{2}R_{ii}(\boldsymbol{r})\mathrm{e}^{-\mathrm{i}\boldsymbol{k}\cdot\boldsymbol{r}}\,\mathrm{d}^3\boldsymbol{r} \tag{1.22}$$

or, using the components of the velocity spectral tensor in the Craya-Herring frame,

$$e(\boldsymbol{k}) = \frac{1}{2}\left(\Phi^1(\boldsymbol{k}) + \Phi^2(\boldsymbol{k})\right). \tag{1.23}$$

By the Fourier inversion theorem and definition (1.22)

$$\frac{1}{2}R_{ii}(\boldsymbol{r}) = \iiint e(\boldsymbol{k})\mathrm{e}^{\mathrm{i}\boldsymbol{k}\cdot\boldsymbol{r}}\,\mathrm{d}^3\boldsymbol{k} \tag{1.24}$$

so that, setting $\boldsymbol{r} = \boldsymbol{0}$, the integral of $e(\boldsymbol{k})$ equals the mean kinetic energy:

$$\frac{1}{2}\langle u_i u_i\rangle = \iiint e(\boldsymbol{k})\,\mathrm{d}^3\boldsymbol{k}. \tag{1.25}$$

(When the spatial or wavevector dependence is not explicit, variables are considered at the same point in physical or spectral space). Therefore, $e(\boldsymbol{k})$ represents the kinetic energy contents of wavevector $\boldsymbol{k}$. The energy spectrum $E(k)$ is obtained by integrating $e(\boldsymbol{k})$ over a sphere of radius k,

$$E(k) = \iiint e(\boldsymbol{k})\delta(|\boldsymbol{k}| - k)\,\mathrm{d}^3\boldsymbol{k}, \tag{1.26}$$

and it represents the energy contents of all wavevectors with modulus k.

1.1.3 Craya's equation

In this section we derive the evolution equation of $\hat{R}_{ij}$. We consider an incompressible flow whose velocity field u_i is a solution of the Navier-Stokes equations

$$\frac{\partial}{\partial t}u_i + \frac{\partial}{\partial x_l}(u_i u_l) = -\frac{\partial}{\partial x_i}P + \nu\frac{\partial^2}{\partial x_l \partial x_l}u_i + F_i \tag{1.27}$$

$$\frac{\partial}{\partial x_l}u_l = 0 \tag{1.28}$$

and such that $\langle u_i \rangle = 0$. P is the hydrodynamic pressure divided by density, ν is the kinematic viscosity, and F_i is an external (possibly random) force. If the equations are written in a rotating frame and P includes the centrifugal contribution, the Coriolis force appearing in the momentum equation (1.27) is an example of external force. Other examples of external forces, in the context of numerical simulations, are an artificial forcing aimed at feeding turbulence, or a "penalty" force replacing the boundary conditions in immersed boundary methods (see section 2.1.3). Multiplying the momentum equation (1.27) by u_i, ensemble averaging, and using homogeneity and incompressibility (1.28), one obtains the energy balance equation

$$\frac{d}{dt}\frac{\langle u_i u_i \rangle}{2} = -\epsilon + \phi_{\mathrm{inj}} \tag{1.29}$$

where

$$\epsilon = \nu\left\langle \frac{\partial u_i}{\partial x_l}\frac{\partial u_i}{\partial x_l} \right\rangle \tag{1.30}$$

is the mean kinetic-energy viscous dissipation rate and

$$\phi_{\mathrm{inj}} = \langle F_i u_i \rangle \tag{1.31}$$

is the mean kinetic-energy injection rate.

Following Mathieu and Scott [49], we introduce the finite-range Fourier-transform of the velocity field

$$\hat{u}_{\mathcal{L}i}(\boldsymbol{k}) = \frac{1}{(2\pi)^3}\iiint_{-\mathcal{L}}^{\mathcal{L}} u_i(\boldsymbol{x})\mathrm{e}^{-\mathrm{i}\boldsymbol{k}\cdot\boldsymbol{x}}\,\mathrm{d}^3\boldsymbol{x}, \tag{1.32}$$

where the triple integral is over a box of size $2\mathcal{L}$ centered in $\boldsymbol{x} = \boldsymbol{0}$. Taking the finite-range Fourier-transform of Eq. (1.28) and using property (1.3)

$$k_l \hat{u}_{\mathcal{L}l} = 0, \tag{1.33}$$

while the transform of Eq. (1.27) leads to

$$\frac{\partial \hat{u}_{\mathcal{L}i}}{\partial t} + \hat{N}_{\mathcal{L}i} = -\mathrm{i}k_i \hat{P}_{\mathcal{L}} - \nu k^2 \hat{u}_{\mathcal{L}i} + \hat{F}_{\mathcal{L}i} \tag{1.34}$$

where $\hat{N}_{\mathcal{L}i}$ is the finite-range Fourier transform of the nonlinear term $\partial\left(u_i u_l\right)/\partial x_l$. From the last equation, by scalar product with $\boldsymbol{k}$ and enforcing incompressibility, *i.e.* Eq. (1.33), one obtains the Poisson equation for pressure in Fourier space

$$-\mathrm{i}k^2 \hat{P}_{\mathcal{L}} = k_l \hat{N}_{\mathcal{L}l} - k_l \hat{F}_{\mathcal{L}l}. \tag{1.35}$$

Using this equation to eliminate $\hat{P}_{\mathcal{L}}$ in Eq. (1.34) leads to the momentum equation in Fourier space

$$\frac{\partial \hat{u}_{\mathcal{L}i}}{\partial t} = -P_{il} \hat{N}_{\mathcal{L}l} - \nu k^2 \hat{u}_{\mathcal{L}i} + P_{il} \hat{F}_{\mathcal{L}l} \tag{1.36}$$

where $P_{ij} = \delta_{ij} - \frac{k_i k_j}{k^2}$ is the operator that projects a vector onto the plane orthogonal to $\boldsymbol{k}$. The transform of the nonlinear term can be computed by properties (1.3) and (1.4) as

$$\hat{N}_{\mathcal{L}l}(\boldsymbol{k}) = \mathrm{i}k_m \iiint \hat{u}_{\mathcal{L}l}(\boldsymbol{q}) \hat{u}_{\mathcal{L}m}(\boldsymbol{k} - \boldsymbol{q}) \, \mathrm{d}^3\boldsymbol{q}. \tag{1.37}$$

Using Eq. (1.10) one can show that $\langle \hat{u}^*_{\mathcal{L}i} \hat{u}_{\mathcal{L}j} \rangle$ is linked to $\hat{R}_{ij}$ through

$$\langle \hat{u}^*_{\mathcal{L}i}(\boldsymbol{k}) \hat{u}_{\mathcal{L}j}(\boldsymbol{k}) \rangle = \left(\frac{\mathcal{L}}{\pi}\right)^3 \hat{R}_{\mathcal{L}ij}(\boldsymbol{k}) \tag{1.38}$$

such that

$$\left(\frac{\mathcal{L}}{\pi}\right)^3 \frac{\partial}{\partial t} \hat{R}_{\mathcal{L}ij}(\boldsymbol{k}) = \left\langle \frac{\partial \hat{u}^*_{\mathcal{L}i}}{\partial t} \hat{u}_{\mathcal{L}j} \right\rangle + \left\langle \hat{u}^*_{\mathcal{L}i} \frac{\partial \hat{u}_{\mathcal{L}j}}{\partial t} \right\rangle. \tag{1.39}$$

The momentum equation in spectral space, Eq. (1.36), can then be used to compute the evolution equation of the velocity spectral tensor. Therefore, multiplying the complex conjugate of Eq. (1.36) by $\hat{u}_{\mathcal{L}j}(\boldsymbol{k})$ and averaging

$$\left\langle \frac{\partial \hat{u}^*_{\mathcal{L}i}}{\partial t} \hat{u}_{\mathcal{L}j} \right\rangle = -P_{il} \left\langle \hat{N}^*_{\mathcal{L}l} \hat{u}_{\mathcal{L}j} \right\rangle - \nu k^2 \left\langle \hat{u}^*_{\mathcal{L}i} \hat{u}_{\mathcal{L}j} \right\rangle + P_{il} \left\langle \hat{F}^*_{\mathcal{L}l} \hat{u}_{\mathcal{L}j} \right\rangle. \tag{1.40}$$

Using Eq. (1.38), the viscous term, $-\nu k^2 \langle \hat{u}^*_{\mathcal{L}i} \hat{u}_{\mathcal{L}j} \rangle$, is equal to $-\nu k^2 \left(\mathcal{L}/\pi\right)^3 \hat{R}_{\mathcal{L}ij}$. Similarly, by Eq. (1.10) the forcing term in Eq. (1.40) becomes

$$P_{il} \left\langle \hat{F}^*_{\mathcal{L}l} \hat{u}_{\mathcal{L}j} \right\rangle = \left(\frac{\mathcal{L}}{\pi}\right)^3 P_{il} \hat{\phi}_{\mathcal{L}lj} \tag{1.41}$$

where $\hat{\phi}_{\mathcal{L}lj}(\boldsymbol{k})$ is the transform of the two-point correlation between external force and velocity

$$\phi_{lj}(\boldsymbol{r}) = \langle F_l(\boldsymbol{x}) u_j(\boldsymbol{x}+\boldsymbol{r}) \rangle \tag{1.42}$$

which is supposed to be independent of $\boldsymbol{x}$ and to decrease sufficiently rapidly as $|\boldsymbol{r}|$ increases. For the nonlinear term in Eq. (1.40), one can use property (1.5) and the definition of $\hat{N}_{\mathcal{L}l}$ (1.37) to obtain

$$-P_{il}(\boldsymbol{k}) \left\langle \hat{N}^*_{\mathcal{L}l}(\boldsymbol{k}) \hat{u}_{\mathcal{L}j}(\boldsymbol{k}) \right\rangle = \mathrm{i} P_{il}(\boldsymbol{k}) k_m \iiint \langle \hat{u}^*_{\mathcal{L}l}(\boldsymbol{q}) \hat{u}^*_{\mathcal{L}m}(\boldsymbol{k}-\boldsymbol{q}) \hat{u}_{\mathcal{L}j}(\boldsymbol{k}) \rangle \, \mathrm{d}^3\boldsymbol{q} \tag{1.43}$$

and then by Eq. (1.13)

$$-P_{il}(\boldsymbol{k}) \left\langle \hat{N}^*_{\mathcal{L}l}(\boldsymbol{k}) \hat{u}_{\mathcal{L}j}(\boldsymbol{k}) \right\rangle = \mathrm{i} P_{il}(\boldsymbol{k}) k_m \left(\frac{\mathcal{L}}{\pi}\right)^3 \iiint \hat{\hat{S}}_{\mathcal{L}ljm}(\boldsymbol{k}, \boldsymbol{q}-\boldsymbol{k}) \, \mathrm{d}^3\boldsymbol{q} \tag{1.44}$$

where $\hat{\hat{S}}_{\mathcal{L}ljm}$ is the double Fourier transform of the third-order three-point correlation

$$S_{ljm}(\boldsymbol{r}, \boldsymbol{r}') = \langle u_l(\boldsymbol{x}) u_j(\boldsymbol{x}+\boldsymbol{r}) u_m(\boldsymbol{x}+\boldsymbol{r}') \rangle \, . \tag{1.45}$$

Equation (1.40) can thus be rewritten as

$$\begin{aligned} \left\langle \frac{\partial \hat{u}^*_{\mathcal{L}i}(\boldsymbol{k})}{\partial t} \hat{u}_{\mathcal{L}j}(\boldsymbol{k}) \right\rangle = {} & \mathrm{i} P_{il}(\boldsymbol{k}) k_m \left(\frac{\mathcal{L}}{\pi}\right)^3 \iiint \hat{\hat{S}}_{\mathcal{L}ljm}(\boldsymbol{k}, \boldsymbol{q}-\boldsymbol{k}) \, \mathrm{d}^3\boldsymbol{q} \\ & -\nu k^2 \left(\frac{\mathcal{L}}{\pi}\right)^3 \hat{R}_{\mathcal{L}ij}(\boldsymbol{k}) + \left(\frac{\mathcal{L}}{\pi}\right)^3 P_{il}(\boldsymbol{k}) \hat{\phi}_{\mathcal{L}lj}(\boldsymbol{k}). \end{aligned} \tag{1.46}$$

The expression of $\langle \hat{u}^*_{\mathcal{L}i} \partial \hat{u}_{\mathcal{L}j} / \partial t \rangle$ can be computed in a similar way, leading to

$$\begin{aligned} \left\langle \hat{u}^*_{\mathcal{L}i}(\boldsymbol{k}) \frac{\partial \hat{u}_{\mathcal{L}j}(\boldsymbol{k})}{\partial t} \right\rangle = {} & -\mathrm{i} P_{jl}(\boldsymbol{k}) k_m \left(\frac{\mathcal{L}}{\pi}\right)^3 \iiint \hat{\hat{S}}_{\mathcal{L}ilm}(\boldsymbol{q}, \boldsymbol{k}-\boldsymbol{q}) \, \mathrm{d}^3\boldsymbol{q} \\ & -\nu k^2 \left(\frac{\mathcal{L}}{\pi}\right)^3 \hat{R}_{\mathcal{L}ij}(\boldsymbol{k}) + \left(\frac{\mathcal{L}}{\pi}\right)^3 P_{jl}(\boldsymbol{k}) \hat{\phi}^*_{\mathcal{L}li}(\boldsymbol{k}). \end{aligned} \tag{1.47}$$

Summing Eqs. (1.46) and (1.47), using Eq. (1.39), eliminating $(\mathcal{L}/\pi)^3$, and in the limit of infinitely large $\mathcal{L}$, one finally obtains Craya's equation:

$$\frac{\partial \hat{R}_{ij}}{\partial t} = T_{ij} - 2\nu k^2 \hat{R}_{ij} + \hat{\Phi}_{ij} \tag{1.48}$$

where

$$T_{ij}(\boldsymbol{k}) = \mathrm{i} k_m \left[-P_{jl}(\boldsymbol{k}) \iiint \hat{\hat{S}}_{\mathcal{L}ilm}(\boldsymbol{q}, \boldsymbol{k}-\boldsymbol{q}) \, \mathrm{d}^3\boldsymbol{q} + P_{il}(\boldsymbol{k}) \iiint \hat{\hat{S}}_{ljm}(\boldsymbol{k}, \boldsymbol{q}-\boldsymbol{k}) \, \mathrm{d}^3\boldsymbol{q} \right] \tag{1.49}$$

and

$$\hat{\Phi}_{ij}(\boldsymbol{k}) = P_{il}(\boldsymbol{k}) \hat{\phi}_{\mathcal{L}lj}(\boldsymbol{k}) + P_{jl}(\boldsymbol{k}) \hat{\phi}^*_{\mathcal{L}li}(\boldsymbol{k}). \tag{1.50}$$

The evolution equation of the energy spectral density can be computed by taking half the trace of Craya's equation (1.48),

$$\frac{\partial e(\boldsymbol{k})}{\partial t} = T(\boldsymbol{k}) - 2\nu k^2 e(\boldsymbol{k}) + \hat{\Phi}(\boldsymbol{k}) \tag{1.51}$$

where the nonlinear term, after some manipulations, is equal to

$$T(\boldsymbol{k}) = k_m \Im \iiint \hat{\hat{S}}_{iim}(\boldsymbol{q}, \boldsymbol{k}-\boldsymbol{q}) \, \mathrm{d}^3\boldsymbol{q} \tag{1.52}$$

and

$$\hat{\Phi}(\boldsymbol{k}) = \Re \hat{\phi}_{ii}(\boldsymbol{k}) \tag{1.53}$$

is the transform of the even part of ϕ_{ii}, *i.e.*

$$\Phi(\boldsymbol{r}) = \frac{1}{2}\left(\phi_{ii}(\boldsymbol{r}) + \phi_{ii}(-\boldsymbol{r})\right) \tag{1.54}$$

which is also equal to $\langle F_i(\boldsymbol{x}) \left(u_i(\boldsymbol{x}+\boldsymbol{r}) + u_i(\boldsymbol{x}-\boldsymbol{r})\right)\rangle /2$.

Integrating Eq. (1.51) over a sphere of radius k and using the definition of $E(k)$ (1.26) leads to the well-known Lin's equation

$$\frac{\partial E(k)}{\partial t} = T_E(k) - 2\nu k^2 E(k) + \hat{\Phi}_E(k) \tag{1.55}$$

where

$$T_E(k) = \int T(\boldsymbol{k}) \delta(|\boldsymbol{k}| - k) \, \mathrm{d}\boldsymbol{k} \tag{1.56}$$

and

$$\hat{\Phi}_E(k) = \int \hat{\Phi}(\boldsymbol{k}) \delta(|\boldsymbol{k}| - k) \, \mathrm{d}\boldsymbol{k}. \tag{1.57}$$

Under the hypothesis of statistical isotropy, $e(\boldsymbol{k})$ depends only on the modulus k of the wavevector, and thus Eq. (1.26) leads to $E(k) = 4\pi k^2 e(\boldsymbol{k})$. Then, Eq. (1.55) can be trivially obtained by multiplying Eq. (1.51) by $4\pi k^2$.

Integrate over all wavevectors the evolution equation of the energy spectral density, Eq. (1.51), and use Eq. (1.25) to obtain

$$\frac{d}{dt}\frac{\langle u_i u_i \rangle}{2} = \int T(\boldsymbol{k}) \, \mathrm{d}\boldsymbol{k} - 2\nu \int k^2 e(\boldsymbol{k}) \, \mathrm{d}\boldsymbol{k} + \int \hat{\Phi}(\boldsymbol{k}) \, \mathrm{d}\boldsymbol{k}. \tag{1.58}$$

By comparison with the energy balance equation (1.29) and using the definition of dissipation (1.30), since Eqs. (1.29) and (1.58) must be verified for an arbitrary positive value of ν and for an arbitrary external force, one also obtains

$$\epsilon = 2\nu \int k^2 e(\boldsymbol{k}) \, \mathrm{d}\boldsymbol{k}, \tag{1.59}$$

$$\phi_{\text{inj}} = \int \hat{\Phi}(\boldsymbol{k})\,\mathrm{d}\boldsymbol{k}, \tag{1.60}$$

and

$$\int T(\boldsymbol{k})\,\mathrm{d}\boldsymbol{k} = 0. \tag{1.61}$$

As for the nonlinear term $T(\boldsymbol{k})$ in the energy spectral density equation (1.51), one can prove through a direct computation that energy is also conserved within every nonlinear triadic interaction. In other words, the Fourier transform of the third-order moment S_{ijl} appearing in the definition of $T(\boldsymbol{k})$ (1.52) satisfies

$$k_m \Im\hat{\hat{S}}_{iim}(\boldsymbol{q}, \boldsymbol{k}-\boldsymbol{q}) + k_m \Im\hat{\hat{S}}_{iim}(\boldsymbol{k}-\boldsymbol{q}, \boldsymbol{q}) + \tag{1.62}$$

$$q_m \Im\hat{\hat{S}}_{iim}(\boldsymbol{k}, \boldsymbol{q}-\boldsymbol{k}) + q_m \Im\hat{\hat{S}}_{iim}(\boldsymbol{q}-\boldsymbol{k}, \boldsymbol{k}) + \tag{1.63}$$

$$(k_m - q_m)\Im\hat{\hat{S}}_{iim}(\boldsymbol{k}, -\boldsymbol{q}) + (k_m - q_m)\Im\hat{\hat{S}}_{iim}(-\boldsymbol{q}, \boldsymbol{k}) = 0. \tag{1.64}$$

1.1.4 Helicity

In physical space, helicity density is the scalar product between velocity $\boldsymbol{u}$ and vorticity $\boldsymbol{\omega} = \nabla \times \boldsymbol{u}$, *i.e.* $u_i\omega_i$. Exactly like energy, its integral is an inviscid invariant [54, 55], even in the presence of background rotation. The mean helicity balance equation can be computed from the momentum equation (1.27) and by using statistical homogeneity as

$$\frac{d}{dt}\langle u_i\omega_i\rangle = -\epsilon_h + \phi_h \tag{1.65}$$

where

$$\epsilon_h = -2\nu\left\langle \boldsymbol{\omega}\cdot\nabla^2\boldsymbol{u}\right\rangle \tag{1.66}$$

is the mean helicity viscous dissipation rate and

$$\phi_h = 2\langle \boldsymbol{\omega}\cdot\boldsymbol{F}\rangle \tag{1.67}$$

is the mean helicity injection rate.

We call $h(\boldsymbol{k})$ the Fourier transform of the velocity-vorticity correlation $\langle u_i(\boldsymbol{x})\omega_i(\boldsymbol{x}+\boldsymbol{r})\rangle$ (which by homogeneity is independent of $\boldsymbol{x}$),

$$h(\boldsymbol{k}) = \frac{1}{(2\pi)^3}\iiint \langle u_i(\boldsymbol{x})\omega_i(\boldsymbol{x}+\boldsymbol{r})\rangle\,\mathrm{e}^{-\mathrm{i}\boldsymbol{k}\cdot\boldsymbol{r}}\mathrm{d}^3\boldsymbol{r}. \tag{1.68}$$

Therefore, by the Fourier inversion theorem

$$\langle u_i(\boldsymbol{x})\omega_i(\boldsymbol{x}+\boldsymbol{r})\rangle = \iiint h(\boldsymbol{k})\mathrm{e}^{\mathrm{i}\boldsymbol{k}\cdot\boldsymbol{r}}\mathrm{d}^3\boldsymbol{k} \tag{1.69}$$

and setting $\boldsymbol{r} = \boldsymbol{0}$ one finds that $\int h(\boldsymbol{k})\,\mathrm{d}\boldsymbol{k}$ equals the mean helicity. Thus, $h(\boldsymbol{k})$ represents the helicity contents at wavevector $\boldsymbol{k}$. The helicity spectrum is obtained by integrating $h(\boldsymbol{k})$ over a sphere of radius k,

$$H(k) = \int h(\boldsymbol{k})\delta(|\boldsymbol{k}| - k)\,\mathrm{d}\boldsymbol{k} \tag{1.70}$$

and represents the helicity contents of all wavevectors with modulus k. Since vorticity is a pseudo-vector, helicity is a pseudoscalar quantity, *e.g.* it changes sign under a reflection, or by shifting from a right-handed frame to a left-handed frame, or by inverting all the axes of the coordinate system. Therefore, any turbulent flow with non-vanishing mean helicity lacks mirror-symmetry.

From definition (1.68), shifting to finite-range integrals and using Eq. (1.10)

$$h_{\mathcal{L}}(\boldsymbol{k}) \left(\frac{\mathcal{L}}{\pi}\right)^3 = \langle \hat{u}^*_{\mathcal{L}i}(\boldsymbol{k})\hat{\omega}_{\mathcal{L}i}(\boldsymbol{k})\rangle\,, \tag{1.71}$$

so that $h(\boldsymbol{k})$ can also be computed as the limit of velocity-vorticity transforms correlation as $\mathcal{L} \to \infty$. Similarly, for the energy spectral density

$$e_{\mathcal{L}}(\boldsymbol{k}) \left(\frac{\mathcal{L}}{\pi}\right)^3 = \frac{1}{2}\,\langle \hat{u}^*_{\mathcal{L}i}(\boldsymbol{k})\hat{u}_{\mathcal{L}i}(\boldsymbol{k})\rangle\,. \tag{1.72}$$

Equation (1.71), together with the definition of vorticity and property (1.3), leads to

$$h_{\mathcal{L}}(\boldsymbol{k}) \left(\frac{\mathcal{L}}{\pi}\right)^3 = \mathrm{i}\epsilon_{ilm}k_l\,\langle \hat{u}^*_{\mathcal{L}i}(\boldsymbol{k})\hat{u}_{\mathcal{L}m}(\boldsymbol{k})\rangle \tag{1.73}$$

(ϵ_{ijk} is the alternating Levi-Civita tensor), and using the Schwarz inequality $|h_{\mathcal{L}}(\boldsymbol{k})|\,(\mathcal{L}/\pi)^3 \leq k\,\langle \hat{u}^*_{\mathcal{L}i}(\boldsymbol{k})\hat{u}_{\mathcal{L}i}(\boldsymbol{k})\rangle$. Thus, by comparison with Eq. (1.72) and in the limit of infinitely large $\mathcal{L}$, one obtains the realizability condition

$$|h(\boldsymbol{k})| \leq 2ke(\boldsymbol{k}). \tag{1.74}$$

Therefore, we define the *relative* helicity as $H_{\mathrm{rel}} = \mathcal{H}L_h/K$ where $\mathcal{H} = \int h(\boldsymbol{k})\,\mathrm{d}\boldsymbol{k}$ is the mean helicity, $K = \int e(\boldsymbol{k})\,\mathrm{d}\boldsymbol{k}$ is the turbulent kinetic energy and L_h is a modified lengthscale (different from the integral lengthscale), defined from the spherically integrated kinetic energy spectrum as

$$L_h = \frac{1}{2}\frac{\int E(k)\,\mathrm{d}k}{\int kE(k)\,\mathrm{d}k} \tag{1.75}$$

so that, from the above inequality, $H_{\mathrm{rel}} \leq 1$.

We want to express now $h(\boldsymbol{k})$ in terms of the components of the velocity spectral tensor $\hat{R}_{ij}$. From Eq. (1.73) and recalling Eq. (1.38),

$$h(\boldsymbol{k}) = \mathrm{i}\epsilon_{ilm}k_l\hat{R}_{im}. \tag{1.76}$$

Furthermore, $h(\boldsymbol{k})$ can be expressed as a function of the imaginary part of $\Phi^{12}(\boldsymbol{k})$ only, where Φ^{12} is the off-diagonal component of the spectral velocity tensor $\hat{R}_{ij}$ in Craya frame (see Eq. (1.21)),

$$h(\boldsymbol{k}) = \mathrm{i}k\left(\Phi^{12*}(\boldsymbol{k}) - \Phi^{12}(\boldsymbol{k})\right) = 2k\Im\Phi^{12}(\boldsymbol{k}). \tag{1.77}$$

The evolution equation of the helicity spectral density can be computed from the momentum equation in Fourier space (1.36), after shifting to finite-range integrals through Eq. (1.73):

$$\frac{\partial h(\boldsymbol{k})}{\partial t} = T_h(\boldsymbol{k}) - 2\nu k^2 h(\boldsymbol{k}) + \hat{\Phi}_h(\boldsymbol{k}) \tag{1.78}$$

where

$$T_h(\boldsymbol{k}) = 2\epsilon_{ilm}k_j k_l \Re \iiint \hat{\hat{S}}_{imj}(\boldsymbol{q}, \boldsymbol{k}-\boldsymbol{q})\,\mathrm{d}^3\boldsymbol{q} \tag{1.79}$$

and

$$\hat{\Phi}_h(\boldsymbol{k}) = -2\epsilon_{ilm}k_l \Im\hat{\phi}_{im}. \tag{1.80}$$

Finally, with a procedure similar to the one used in section 1.1.3 for energy, one can prove that helicity is conserved within every nonlinear triadic interaction.

1.1.5 Anisotropy in two-point statistics

The characterisation of anisotropy in homogeneous turbulence addresses a two-fold question. First, what physical quantities are suitable to qualitatively detect isotropy breaking in turbulence subject to external distorsions such as solid body rotation, density gradient, mean shear, *etc.*? Second, how does one quantify and compare the level of anisotropy? One therefore needs a relevant characterisation of this anisotropy, and several choices are possible. For example, one can compute the normalized anisotropic part of the Reynolds stress tensor R_{ij} as $b_{ij} = R_{ij}/R_{kk} - \delta_{ij}/3$. If the off-diagonal components of b_{ij} are not zero the flow is anisotropic, but these quantities only represent anisotropy from a global point of view—mostly related to the large scales. A widely adopted characterisation of anisotropy based on b_{ij} is the method proposed by Lumley & Newman (1977) [48] which consists in identifying the dominant structure of the flow from the position of the second and third invariants (I_2,I_3) of b_{ij} within the so-called Lumley triangle. This tells if the flow structure is mostly 2-component axisymmetric, 1-component, or isotropic, depending on the closeness of the (I_2,I_3) point to one of the vertices of the triangle. However, useful as this simple method may be, it does not tell which scales are most anisotropic. A refined picture is for instance required for rotating turbulence in which one has to identify isotropic and anisotropic subranges at different length scales.

We therefore introduce hereafter a scale-by-scale evaluation of anisotropy in two-point statistics through a modal decomposition of the velocity spectral tensor $\hat{R}_{ij}$. This description is suitable for a wide range of anisotropic flows, such as turbulence subject to solid body rotation, stratified turbulence, flows subject to axisymmetric contractions or expansions or magneto-hydrodynamic turbulence for a conducting fluid subject to an external magnetic field of fixed orientation. Non axisymmetric cases are more complex and only a few studies have been devoted to their statistical description (for instance in [44]).

1.1.6 Modal decomposition of the velocity spectral tensor

From Eq. (1.21), $\hat{R}_{ij}$ can be rewritten as [17, 73]

$$\hat{R}_{ij}(\boldsymbol{k}) = e(\boldsymbol{k})P_{ij}(\boldsymbol{k}) + \Re\left(z(\boldsymbol{k})\mathcal{N}_i(\boldsymbol{k})\mathcal{N}_j(\boldsymbol{k})\right) + \mathrm{i}\epsilon_{ijl}\frac{k_l}{2k^2}h(\boldsymbol{k}) \tag{1.81}$$

where $\boldsymbol{\mathcal{N}}(\boldsymbol{k}) = \boldsymbol{e}^{(2)}(\boldsymbol{k}) - \mathrm{i}\boldsymbol{e}^{(1)}(\boldsymbol{k})$ are helical modes [81]. The decomposition (1.81) displays three important spectral functions which characterize fully the second-order velocity correlations of the flow and carry useful physical meaning about the flow structure at different scales [17, 25, 73]:

1. The energy spectral density $e(\boldsymbol{k})$, already introduced in section 1.1.2. If energy is concentrated in modes corresponding to wavevectors close to the plane $\boldsymbol{k}\cdot\boldsymbol{n} = 0$, the flow is almost bidimensional, while energy concentrated in wavevectors close to $\boldsymbol{n}$ indicates a trend towards a vertically-sheared horizontal flow.

2. The helicity spectral density $h(\boldsymbol{k})$, introduced in section 1.1.4. The helicity contribution in Eq. (1.81) is imaginary and antisymmetric.

3. Finally, the complex-valued function

$$z(\boldsymbol{k}) = \left(\Phi^2(\boldsymbol{k}) - \Phi^1(\boldsymbol{k})\right)/2 + \mathrm{i}\Re\Phi^{12}(\boldsymbol{k}) \tag{1.82}$$

   is the polarization spectral density and contains information on the structure of the flow at different scales. Consider for instance a shell of radius k in spectral space in which the wavevectors closer to the horizontal plane $k_3 = 0$ hold much more energy than the others (which is the case of strongly rotating turbulence if $\boldsymbol{\Omega}$ is parallel to the x_3 axis). In this special case, if the real part of polarization is mostly dominated by the poloidal spectral energy Φ^2, the corresponding flow structure at the scale $1/k$ is characterized by axial velocity, or "jetal" structures, whereas if Φ^1 prevails, axial vorticity is more important

and the flow displays "vortical" structures. Detailed comments about the role of $z(\boldsymbol{k})$ in rotating turbulence or MHD turbulence can be found in [17, 25, 27].

In Chapter 3 we show normalized integrated spectra of the real part of $z(\boldsymbol{k})$, $\Re Z(k)/E(k) = (E^{\rm pol}(k) - E^{\rm tor}(k))/E(k)$, where $E^{\rm pol}(k) = \int \Phi^2(\boldsymbol{k})\delta(|\boldsymbol{k}| - k)\,\mathrm{d}\boldsymbol{k}$ and $E^{\rm tor}(k) = \int \Phi^1(\boldsymbol{k})\delta(|\boldsymbol{k}| - k)\,\mathrm{d}\boldsymbol{k}$ are the poloidal and the toroidal energy spectra, respectively.

In the above decomposition (1.81) we have retained the general $\boldsymbol{k}$ dependence. Furthermore, one can use axisymmetry to consider only the dependence of the spectra upon the axial and horizontal components of the wavevector $\boldsymbol{k}$ (see for instance [32]), or upon the wavenumber k and the polar orientation θ of $\boldsymbol{k}$ with respect to the axis of symmetry [16, 34].

We also recall here the fact that the anisotropy tensor b_{ij}, which carries a rough anisotropic information, can be split as $b_{ij} = b_{ij}^{(e)} + b_{ij}^{(z)} + b_{ij}^{(h)}$ into more informative contributions brought up by integrating the spectra:

$$
\begin{aligned}
b_{ij}^{(e)} &= \frac{1}{\langle u_k u_k \rangle} \iiint \left[e(\boldsymbol{k}) - E(k)/(4\pi k^2) \right] P_{ij} d^3\boldsymbol{k} \\
b_{ij}^{(z)} &= \frac{1}{\langle u_k u_k \rangle} \iiint \Re \left[z(\boldsymbol{k}) N_i(\boldsymbol{k}) N_j(\boldsymbol{k}) \right] d^3\boldsymbol{k} \\
b_{ij}^{(h)} &= \frac{1}{\langle u_k u_k \rangle} \iiint \mathrm{i} h(\boldsymbol{k}) \epsilon_{ijl} \frac{k_l}{2k^2} d^3\boldsymbol{k} \\
&= \frac{1}{\langle u_k u_k \rangle} \iiint \mathrm{i} \frac{H(k)}{4\pi k^2} \epsilon_{ijl} \frac{k_l}{2k^2} d^3\boldsymbol{k} + \frac{1}{\langle u_k u_k \rangle} \iiint \mathrm{i} \left[h(\boldsymbol{k}) - \frac{H(k)}{4\pi k^2} \right] \epsilon_{ijl} \frac{k_l}{2k^2} d^3\boldsymbol{k}.
\end{aligned}
$$

For instance, in exactly isotropic mirror-symmetric three-dimensional turbulence, $b_{ij} = b_{ij}^{(e)} = b_{ij}^{(z)} = b_{ij}^{(h)} = 0$, whereas two-dimensional turbulence (for which helicity is identically zero) with only two components of velocity in the plane (1,2) is characterized as the departure from 3D isotropy by $b_{33} = -1/3$, $b_{33}^{(e)} = 1/6$ and $b_{33}^{(z)} = -1/2$ [17]. Thus the e, z, h-related contributions to the deviatoric tensor b_{ij} provide useful quantitative indicators about anisotropic trends in the flow, but retaining the spectral information permits to qualify the flow structure in a scale-dependent way.

Finally note that in the following chapters we will focus on directional and polarization anisotropy, and the word "anisotropic" will refer to any isotropy breaking but mirror-symmetry breaking.

1.2 Separation-space view

The quantities presented in the previous section, and the related results obtained with spectral analysis for homogeneous turbulence, have their counterparts in the space of separation vectors in physical space. In this section we only derive the equivalent of the energy spectral density equation, *i.e.* the Kármán-Howarth-Monin equation, highlight the relationship between the two, and finally recall the exact four-thirds Kolmogorov law.

1.2.1 Kármán-Howarth-Monin equation

The Kármán-Howarth-Monin equation [28] is the evolution equation of half the two-point velocity correlation

$$R(\boldsymbol{r}) = \langle u_i(\boldsymbol{x}) u_i(\boldsymbol{x}+\boldsymbol{r}) \rangle \,, \tag{1.83}$$

i.e. half the trace of the velocity correlation tensor $R_{ij}(\boldsymbol{r})$ introduced in section 1.1.2. Again, the general external force F_i possibly includes the Coriolis force (if a rotating frame is considered and P includes the centrifugal contribution) or of an artificial numerical forcing. Here we denote $\boldsymbol{x}'$ the variable $\boldsymbol{x}+\boldsymbol{r}$, such that $\partial/\partial x_i' = \partial/\partial x_i$ at constant $\boldsymbol{r}$, $\partial/\partial x_i' = \partial/\partial r_i$ at constant $\boldsymbol{x}$ and $\partial/\partial r_i = -\partial/\partial x_i$ at constant $\boldsymbol{x}'$. Multiplying the momentum equation (1.27) by $u_i(\boldsymbol{x}')$ and ensemble averaging, one obtains

$$\begin{aligned} \left\langle u_i(\boldsymbol{x}') \frac{\partial u_i(\boldsymbol{x})}{\partial t} \right\rangle = &- \left\langle u_i(\boldsymbol{x}') \frac{\partial}{\partial x_l} \left(u_i(\boldsymbol{x}) u_l(\boldsymbol{x}) \right) \right\rangle - \left\langle u_i(\boldsymbol{x}') \frac{\partial P(\boldsymbol{x})}{\partial x_i} \right\rangle \\ &+ \nu \left\langle u_i(\boldsymbol{x}') \frac{\partial^2 u_i(\boldsymbol{x})}{\partial x_l \partial x_l} \right\rangle + \langle u_i(\boldsymbol{x}') F_i(\boldsymbol{x}) \rangle \,. \end{aligned} \tag{1.84}$$

Using incompressibility and homogeneity the pressure term vanishes, and therefore, after some manipulations,

$$\left\langle u_i(\boldsymbol{x}') \frac{\partial u_i(\boldsymbol{x})}{\partial t} \right\rangle = \frac{\partial}{\partial r_l} \langle u_i(\boldsymbol{x}') u_i(\boldsymbol{x}) u_l(\boldsymbol{x}) \rangle + \nu \frac{\partial^2 \langle u_i(\boldsymbol{x}') u_i(\boldsymbol{x}) \rangle}{\partial x_l \partial x_l} + \langle u_i(\boldsymbol{x}') F_i(\boldsymbol{x}) \rangle \,. \tag{1.85}$$

Computing in a similar way the contribution of $\langle u_i(\boldsymbol{x}) \partial u_i(\boldsymbol{x}')/\partial t \rangle$, summing the result to the last equation and dividing by 2

$$\begin{aligned} \frac{1}{2} \frac{\partial}{\partial t} R(\boldsymbol{r}) = \frac{1}{2} \Bigg(&\frac{\partial}{\partial r_l} \langle u_i(\boldsymbol{x}') u_i(\boldsymbol{x}) u_l(\boldsymbol{x}) \rangle - \frac{\partial}{\partial r_m} \langle u_i(\boldsymbol{x}) u_i(\boldsymbol{x}') u_m(\boldsymbol{x}') \rangle \Bigg) \\ &+ \nu \frac{\partial^2}{\partial r_l \partial r_l} R(\boldsymbol{r}) + \frac{1}{2} \left(\phi_{ii}(\boldsymbol{r}) + \phi_{ii}(-\boldsymbol{r}) \right) . \end{aligned} \tag{1.86}$$

We recall that $\phi_{ij} = \langle F_i(\boldsymbol{x}) u_j(\boldsymbol{x}+\boldsymbol{r}) \rangle$ has already been introduced in section 1.1.3 (Eq. (1.42)). Using homogeneity and incompressibility, the nonlinear term can be shown to be equal to the

divergence (in separation space) of the third-order vector moment

$$\mathcal{F}_i(\boldsymbol{r}) = \langle \delta u_i \delta u_j \delta u_j \rangle \tag{1.87}$$

where $\delta u_i = u_i(\boldsymbol{x}') - u_i(\boldsymbol{x})$. Therefore Eq. (1.86) becomes

$$\frac{1}{2}\frac{\partial}{\partial t} R = \frac{1}{4} \nabla \cdot \boldsymbol{\mathcal{F}} + \nu \nabla^2 R + \Phi \tag{1.88}$$

which is referred to as Kármán-Howarth-Monin equation [28, 58]. $\Phi(\boldsymbol{r})$ is the even part of $\phi_{ii}(\boldsymbol{r})$ and has already been defined in section 1.1.3, see Eq. (1.54). Note that only forces that produce work, *i.e.* when the force-velocity correlation is non-vanishing, can have a non-vanishing contribution Φ in Eq. (1.88). This is not the case of the Coriolis force, as explained in section 1.3.

If $\boldsymbol{r} = \boldsymbol{0}$ the velocity correlation R becomes the mean kinetic energy and the Kármán-Howarth-Monin equation becomes the energy balance equation, similarly to the energy spectral density equation after integration over all wavevectors (see section 1.1.3). Furthermore, since Eq. (1.29) and Eq. (1.88) for $\boldsymbol{r} = \boldsymbol{0}$ must be verified for an arbitrary positive value of ν and for an arbitrary external force F_i, using a procedure similar to the one used to obtain Eqs. (1.59)-(1.61),

$$\left[\nu \nabla^2 R\right]_{\boldsymbol{r}=\boldsymbol{0}} = -\epsilon \tag{1.89}$$

$$\Phi(\boldsymbol{r} = \boldsymbol{0}) = \phi_{\text{inj}} \tag{1.90}$$

$$\left[\nabla \cdot \boldsymbol{\mathcal{F}}\right]_{\boldsymbol{r}=\boldsymbol{0}} = 0. \tag{1.91}$$

Moreover, since the Fourier transform of $\frac{1}{2}\frac{\partial}{\partial t} R(\boldsymbol{r})$ is equal to $e(\boldsymbol{k})$, the transform of any term in Eq. (1.88) is equal to the corresponding term in Eq. (1.51), *i.e.* $2k^2 e$, $\hat{\Phi}$ and T are the Fourier transforms of $\nabla^2 R$, Φ and $\frac{1}{4}\nabla \cdot \boldsymbol{\mathcal{F}}$, respectively.

1.2.2 Four-thirds Kolmogorov law

Consider statistically stationary turbulence forced through an external force F_i that does work, so that at large times the time derivative in the Kármán-Howarth-Monin equation (1.88) vanishes. Furthermore, let the kinematic viscosity ν tend to zero, which makes the dissipative term vanish at any finite scale $r = |\boldsymbol{r}|$, and then consider infinitely-small scales $r = |\boldsymbol{r}| \to 0$. Under these assumptions, if the forcing term Φ is continuous in $\boldsymbol{r} = \boldsymbol{0}$, it tends to the mean energy injection rate ϕ_{inj}, which by statistical stationarity and the energy balance equation (1.29) is equal to the mean energy dissipation rate ϵ. Therefore Eq. (1.88) leads to

$$\nabla \cdot \boldsymbol{\mathcal{F}}(\boldsymbol{r}, t) = -4\epsilon \tag{1.92}$$

[28, 58]. Consider now unforced decaying turbulence, so that the forcing contribution in the Kármán-Howarth-Monin equation (1.88) vanishes, and let again ν and then r tend to zero. Under these assumptions

$$\left[\frac{\partial R(\boldsymbol{r})}{\partial t}\right]_{r\to 0} = \left[\frac{\partial}{\partial t}\left\langle u_i(\boldsymbol{x})u_i(\boldsymbol{x}+\boldsymbol{r})\right\rangle\right]_{r\to 0} = 2\frac{\partial}{\partial t}\frac{\langle u_i u_i\rangle}{2} \tag{1.93}$$

which by the energy balance equation (1.29), in the absence of an external force that produces work, is equal to -2ϵ. Therefore, from the Kármán-Howarth-Monin equation (1.88) one obtains the inertial relation (1.92) again.

In homogeneous turbulence experiments or numerical simulations, if the viscosity is small enough and if the possible external force is smooth enough, there exists a range of scales much greater than the dissipative scale η and much smaller than the integral lengthscale. In this range, which is referred to as *inertial* range, $\nu\nabla^2 R \approx 0$ and Φ (in the case of statistically stationary forced turbulence) or $-1/2\partial R/\partial t$ (in the case of decaying unforced turbulence) is approximately equal to ϵ, so that the inertial relation (1.92) is expected to be approximately verified. For example, in the following chapters we will analyze spectral simulations forced through large-scale spectral forcing, in which $\hat{\phi}_{ij}$ vanishes for wavevectors with modulus greater than a relatively small wavenumber k_F, *i.e.* the working external force acts only at "large scales". Then, since the viscosity is small, we are able to consider a range of scales in which $-1/4\nabla\cdot\boldsymbol{\mathcal{F}}$ is almost constant and close to ϵ.

Note that in the derivation of the inertial relation (1.92) we did not assume isotropy. Under the isotropy assumption the third-order vector moment depends only on the modulus of the separation vector $\boldsymbol{r}$ (in addition to time), and only its radial (parallel to $\boldsymbol{r}$) component $\mathcal{F}_r = \langle \delta u_r \delta u_i \delta u_i \rangle$, where $\delta u_r = \delta u_i r_i/\sqrt{r_j r_j}$, is non-zero. Then, if the flow is statistically isotropic, one can integrate the inertial relation (1.92) over a full sphere of radius r and use the divergence theorem to find the well-known four-thirds Kolmogorov law,

$$\mathcal{F}_r = < \delta u_r \delta u_i \delta u_i > = -\frac{4}{3}\epsilon r \tag{1.94}$$

[4]. An equivalent form for the above relation is

$$< \delta u_r^3 > = -\frac{4}{5}\epsilon r \tag{1.95}$$

[39], which is referred to as four-fifths Kolmogorov law.

1.3 Rotating turbulence

Rotating turbulence is relevant in many contexts, for instance astrophysical, geophysical and industrial flows, or academic configurations such as the von Kármán-forced turbulence (see Chapter 5). We will focus here on homogeneous rotating turbulence. The rotation rate vector $\mathbf{\Omega}$ introduces a preferential direction, which is assumed here to be parallel to the x_3 ("vertical") axis without loss of generality. The flow is statistically axisymmetric about this axis. It is nowadays commonly admitted that background rotation introduces significant anisotropy in the turbulent dynamics through both linear and nonlinear mechanisms [17, 24, 33, 81]. For example, even if the Coriolis force gives rise to no production term in the energy spectral density equation (as shown below), when rotation is strong enough the spectral energy transfer is anisotropic [17]. Because of this, energy is concentrated in modes corresponding to wavevectors close to the (x_1, x_2) plane, which is the plane normal to the rotation rate vector $\mathbf{\Omega}$, and the flow is almost bidimensional (but 3-component). In physical space, this trend towards bidimensionalization manifests through the presence of structures elongated along the direction of rotation ("columnar" structures), see *e.g.* [23, 56, 75, 83, 86]. Also, the pdf of the axial component of the vorticity is asymmetric, and in particular its skewness is positive, which is referred to as cyclone-anticyclone asymmetry, see *e.g.* [7, 29, 36, 59, 60, 78].

In this section, we present the main features of homogeneous rotating turbulence. Therefore, writing the momentum equation (1.27) in a rotating frame, and including the centrifugal contribution in the pressure gradient, the Coriolis force

$$F_{\mathrm{C}i} = -2\epsilon_{ijl}\Omega_j u_l \tag{1.96}$$

(or $\boldsymbol{F}_{\mathrm{C}} = -2\mathbf{\Omega} \times \boldsymbol{u}$) appears explicitly:

$$\frac{\partial}{\partial t}u_i + \frac{\partial}{\partial x_l}\left(u_i u_l\right) = -\frac{\partial}{\partial x_i}P + \nu\frac{\partial^2}{\partial x_l \partial x_l}u_i - 2\epsilon_{ijl}\Omega_j u_l + F_i \tag{1.97}$$

or in spectral space

$$\frac{\partial}{\partial t}\hat{u}_{\mathcal{L}i} = -P_{il}\hat{N}_{\mathcal{L}l} - \nu k^2 \hat{u}_{\mathcal{L}i} - 2P_{il}\epsilon_{ljm}\Omega_j \hat{u}_{\mathcal{L}m} + P_{il}\hat{F}_{\mathcal{L}l}. \tag{1.98}$$

Since the scalar triple product $u_i\epsilon_{ijl}\Omega_j u_l$ is identically zero, the contribution of the Coriolis force in the energy balance equation vanishes, *i.e.* the Coriolis force does no work, see Eqs. (1.29) and (1.31). Using Eqs. (1.41), (1.50) and (1.96), the contribution of the Coriolis force in the Craya equation, Eq. (1.48), is equal to

$$\hat{\Phi}_{\mathrm{C}ij} = -2\epsilon_{lmn}\Omega_m\left(P_{il}\hat{R}_{nj} + P_{jl}\hat{R}_{in}\right). \tag{1.99}$$

However, as expected, its contribution in the evolution equation of the energy spectral density (Eq. (1.51)) vanishes. This can easily be proved by contracting Eq. (1.99) and again noticing that $u_i \epsilon_{ijl} \Omega_j u_l = 0$.

Similar considerations apply to the contribution of the Coriolis force in the evolution equations of global helicity and helicity spectral density, since using Eqs. (1.41) and (1.96) and after some manipulations, $\hat{\Phi}_h$ (defined in Eq. (1.80)) vanishes too.

Since the Kármán-Howarth-Monin equation (1.88) is the Fourier transform of the energy spectral density equation, the contribution of the Coriolis force to the time derivative of $R(\boldsymbol{r})$ must vanish. As a consequence the inertial relation (1.92) does not change in rotating turbulence. Of course the four-thirds and four-fifths laws, Eqs. (1.94) and (1.95), which require isotropy, are no longer valid in the presence of a background rotation.

Note that, even if the possible rotation rate $\boldsymbol{\Omega}$ does not appear in the evolution equations of energy, helicity and velocity correlation, Eqs. (1.51), (1.78) and (1.88), the third-order moments $T(\boldsymbol{k})$, $T_h(\boldsymbol{k})$ and $\boldsymbol{\mathcal{F}}(\boldsymbol{r})$ (and its divergence $\nabla \cdot \boldsymbol{\mathcal{F}}$) depend on the rotation rate too, and therefore $e(\boldsymbol{k})$, $h(\boldsymbol{k})$ and $R(\boldsymbol{r})$ are expected to be anisotropic in general.

Nevertheless, under the usual assumptions of vanishing viscosity and infinitely small scales the inertial relation Eq. (1.92) is recovered again starting from the Kármán-Howarth-Monin equation, which means that $\nabla \cdot \boldsymbol{\mathcal{F}}$ is asymptotically constant and thus isotropic, but $\boldsymbol{\mathcal{F}}$ does not need to be.

1.3.1 Dimensional analysis

Homogeneous rotating turbulence is characterized by four independent dimensional parameters: viscosity ν, a large-scale characteristic velocity U [*e.g.* the root-mean-square (r.m.s.) velocity], a large-scale characteristic lengthscale L (*e.g.* the integral scale), and the rotation rate Ω. In general, the dissipation ϵ represents a further degree of freedom, but we assume that it scales as U^3/L at high Reynolds numbers. This assumption has been extensively investigated in isotropic turbulence. A precise scaling law for $C_\epsilon = \epsilon/(U^3 L)$ has been obtained for non-equilibrium (*e.g.* decaying) turbulence (see [79] for a review). For forced turbulence C_ϵ has been found to be constant and independent of the forcing scheme and the forcing wavenumber, even if turbulence is quasi-periodic and time averages are considered [12, 35].

In addition to the above mentioned dimensional parameters, the flow regime also depends on the initial velocity field (in the case of unforced decaying turbulence) or the energy production mechanism (in the case of statistically stationary forced turbulence). If the initial velocity field

and the working external force are not taken into account, the flow regime can be characterized by two independent non-dimensional parameters. One possible choice is the Reynolds number $Re^L = UL/\nu$ and the macro-Rossby number $Ro^L = U/(2\Omega L)$. The micro-Rossby number is defined as $Ro^\omega = \omega'/(2\Omega)$ [17, 56], where ω' is the r.m.s. vorticity. The macro- and the micro-Rossby numbers quantify the relative importance of advection with respect to the rotation rate. In particular, they can be obtained by comparing the nonlinear term in the momentum equation (1.97) with the Coriolis force $2\epsilon_{ijl}\Omega_j u_l$, the difference between Ro^L and Ro^ω being the choice of the relevant scales.

In addition to L, three relevant lengthscales can be defined: (i) the Kolmogorov scale $\eta = (\nu^3/\epsilon)^{1/4}$; (ii) the Zeman scale [82, 88] at which the inertial timescale $(r^2/\epsilon)^{1/3}$ equals the rotation timescale $1/\Omega$, $r_\Omega = \sqrt{\epsilon/(2\Omega)^3}$; (iii) the scale at which the dissipative timescale r^2/ν equals the rotation timescale, $r_{\Omega d} = \sqrt{\nu/(2\Omega)}$. From the above definitions of η and r_Ω, one can obtain $r_{\Omega d} = r_\Omega^{1/3}\eta^{2/3}$. Therefore, an alternative choice for the independent parameters may be two characteristic lengthscale ratios, *e.g.* L/η and r_Ω/L. Furthermore, if one assumes that $\epsilon \sim U^3/L$, the ratio of the integral scale to the Kolmogorov scale and the ratio of the Zeman scale to the integral scale are linked to Re^L and Ro^L: $L/\eta \sim {Re^L}^{3/4}$ and $r_\Omega/L \sim {Ro^L}^{3/2}$. Similarly, assuming $\omega' \sim \nu/\eta^2$ one finds $Ro^\omega \sim (r_\Omega/\eta)^{2/3}$, and $\epsilon \sim U^3/L$ also leads to $Ro^\omega \sim (Re^L)^{1/2}Ro^L$.

Note that Ro^ω (or the equivalent parameters r_Ω/η and $Re^L {Ro^L}^2$) does not depend on large-scale characteristic quantities such as the integral lengthscale or the r.m.s. velocity. It is indeed the only nondimensional parameter that arises from dimensional analysis if only ϵ, ν and Ω are considered.

If ν tends to zero (and the Reynolds number tends to infinity), both η and $r_{\Omega d}$ tend to zero. Then, if the integral lengthscale L tends to infinity, the only relevant characteristic lengthscale is r_Ω. Therefore, in the asymptotically inviscid limit, classical dimensional arguments [25, 53, 88] support the following phenomenology: scales much larger than r_Ω are mainly affected by rotation while scales much smaller than r_Ω are dominated by the nonlinear dynamics and are expected to return to isotropy. In the following chapters we will refer to characteristic wavenumbers instead of lengthscales: $k_\eta = 1/\eta$, $k_\Omega = 1/r_\Omega$ and $k_{\Omega d} = 1/r_{\Omega d}$. If the rotation rate is not too large $k_\eta > k_{\Omega d} > k_\Omega$. Figure 1.2 displays the relative importance of rotation, inertia and dissipation in every range. On the contrary, if Ω is too strong both k_Ω and $k_{\Omega d}$ become larger than k_η, and rotation dominates at any scale larger than η.

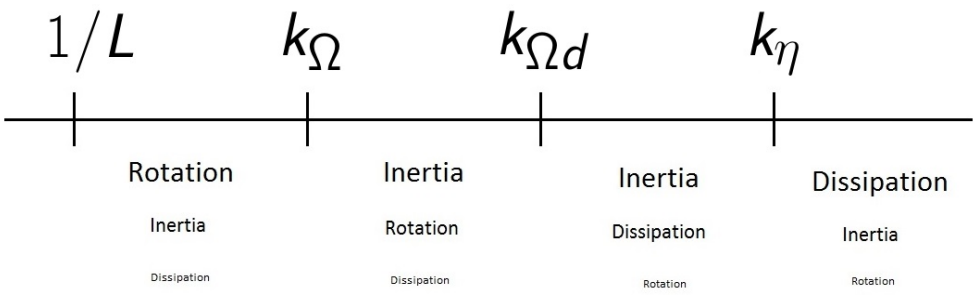

Figure 1.2: Characteristic wavenumbers in rotating turbulence.

1.3.2 Inertial theory in rotating turbulence

Since in homogeneous rotating turbulence the flow is statistically axisymmetric about the rotation axis, the third-order vector moment $\boldsymbol{\mathcal{F}}$ depends on both the modulus of $\boldsymbol{r}$ and the polar angle between $\boldsymbol{r}$ and $\boldsymbol{\Omega}$, but not on the azimuthal angle φ, and is not radial in general. Under some additional assumptions with respect to the isotropic case, Galtier [30, 31] derived an inertial law for $\boldsymbol{\mathcal{F}}$ valid in rotating turbulence with large rotation rate. We briefly illustrate here this theory.

We denote θ the angle between the separation vector $\boldsymbol{r}$ and $\boldsymbol{\Omega}$. $\rho = r\sin\theta$, φ and $\zeta = r\cos\theta$ are the components of the separation vector in the cylindrical frame (ρ, φ, ζ) with the axis ζ parallel to $\boldsymbol{\Omega}$. The key assumption of Galtier's theory is $\boldsymbol{\mathcal{F}}$ to be tangent to the revolution surface S_r obtained by rotating the curve

$$\zeta = \rho_0 \left(\frac{\rho}{\rho_0}\right)^n \tag{1.100}$$

in the $\rho - \zeta$ plane about the ζ axis. This relation represents a general power-law dependence between ζ and ρ, where the exponent n is to be determined. Note that, given n, for any point in the separation space there exists a value of ρ_0 such that this point belongs to a revolution surface corresponding to Eq. (1.100). The unit vector tangent to the curve (1.100) is

$$\boldsymbol{e}_T = \frac{\left(1, n\left(\rho/\rho_0\right)^{n-1}\right)}{\sqrt{1 + n^2\left(\rho/\rho_0\right)^{2(n-1)}}} \tag{1.101}$$

which can be recast as

$$\boldsymbol{e}_T = \frac{(1, n\zeta/\rho)}{\sqrt{1 + n^2\zeta^2/\rho^2}}. \tag{1.102}$$

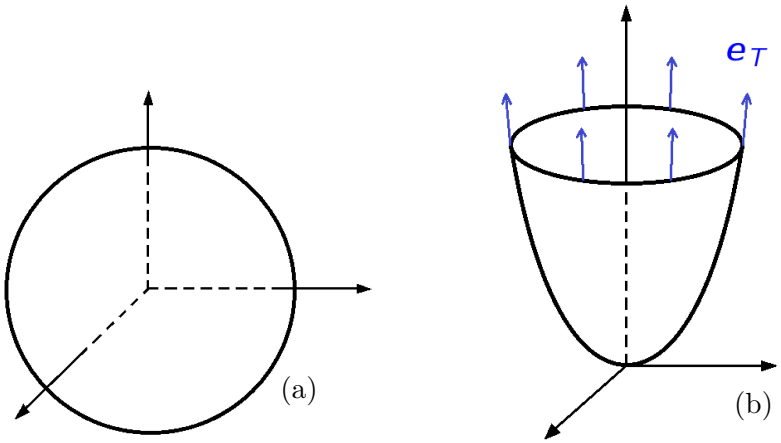

Figure 1.3: Sphere (a) and truncated revolution surface (b) in separation space.

The above assumption corresponds to $\boldsymbol{\mathcal{F}}_p \parallel \boldsymbol{e}_T$, where $\boldsymbol{\mathcal{F}}_p$ is the vector projection of $\boldsymbol{\mathcal{F}}$ onto the plane (ρ, ζ). In the isotropic case $\boldsymbol{\mathcal{F}}$ is radial and the four-thirds law (1.94) can be obtained by integrating the inertial relation (1.92) over a full sphere before using the divergence theorem (see section 1.2.2). We want now to integrate Eq. (1.92) over the surface S_r truncated at a generic height ζ_t. Figure 1.3 displays the integration regions for both the isotropic and axisymmetric cases. The reason of doing so is that, because of axisymmetry, the integral of $|\boldsymbol{\mathcal{F}}_p|$ over the truncation circle can easily be computed, and a simple expression of $\boldsymbol{\mathcal{F}}_p$ can be found again.

Consider then two revolution surfaces truncated at the same ordinate ζ_t, but corresponding to different values of ρ_0, meaning that their abscissas ρ_1 and ρ_2 at $\zeta = \zeta_\mathrm{t}$ are different, say $\rho_2 > \rho_1$. The volume in between can be computed as

$$\Delta\mathcal{V} = \frac{n\pi}{n+2}\zeta_\mathrm{t}\left(\rho_2^2 - \rho_1^2\right). \tag{1.103}$$

Therefore, integration of the inertial relation (1.92) over $\Delta\mathcal{V}$ leads to

$$\int_{S_\mathrm{t}} \boldsymbol{\mathcal{F}} \cdot \boldsymbol{n}\,\mathrm{d}S_\mathrm{t} = -4\epsilon\frac{n\pi}{n+2}\zeta_\mathrm{t}\left(\rho_2^2 - \rho_1^2\right) \tag{1.104}$$

where $\boldsymbol{n}$ is the vertical unit vector bearing the axis of symmetry and S_t is the horizontal truncation surface between the two truncation circles. Note that the azimuthal component of $\boldsymbol{\mathcal{F}}$ is irrelevant here, since because of axisymmetry it is constant with respect to φ and thus it has no contribution in the divergence term of the inertial relation (1.92). Now, letting $\rho_2 \to \rho_1 = \rho$, Eq. (1.104) becomes

$$\boldsymbol{\mathcal{F}} \cdot \boldsymbol{n} 2\pi\rho\mathrm{d}\rho = -4\epsilon\frac{n\pi}{n+2}\zeta_\mathrm{t} 2\rho\mathrm{d}\rho, \tag{1.105}$$

and using the fact that $\boldsymbol{\mathcal{F}}_p$ is parallel to $\boldsymbol{e}_T$, Eq. (1.102), one finally obtains

$$\boldsymbol{\mathcal{F}}_p = -f(\theta)\epsilon\rho\boldsymbol{e}_T \tag{1.106}$$

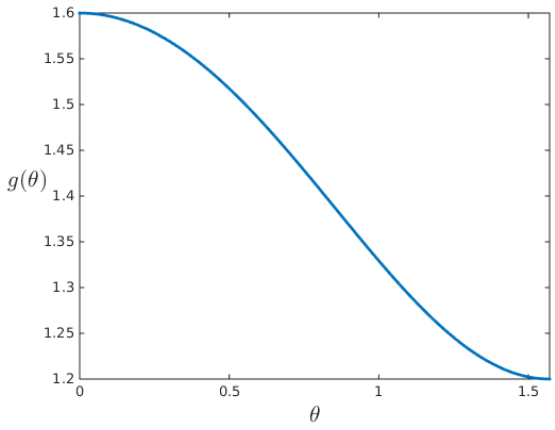

Figure 1.4: Plot of $g(\theta)$ as defined by Eq. (1.109).

where

$$f(\theta) = \frac{4\left(1 + n^2 \cot^2\theta\right)^{1/2}}{n+2} \tag{1.107}$$

or, equivalently,

$$\boldsymbol{\mathcal{F}}_p = -g(\theta)\epsilon r \boldsymbol{e}_T \tag{1.108}$$

where

$$g(\theta) = \frac{4\left(\sin^2\theta + n^2\cos^2\theta\right)^{1/2}}{n+2}. \tag{1.109}$$

The value of n can be estimated—under some assumptions—through dimensional analysis, leading to $n = 4/3$. For details about this result we refer to [30]. $g(\theta)$ is plotted for $n = 4/3$ in Fig. 1.4, which shows that the modulus of $\boldsymbol{\mathcal{F}}$ is greater for small θ (*i.e.* separation vectors closer to $\boldsymbol{\Omega}$) with respect to large θ (*i.e.* separation vectors closer to the horizontal plane).

Chapter 2

Numerical tools

In this chapter the adopted numerical approach is described. First, we introduce the pseudo-spectral method, and present the numerical algorithm used in our simulations and the penalization scheme used for the treatment of boundary conditions in the confined simulations. Then we describe in detail the computation of the statistics used in the following chapters to detect anisotropy in both spectral and separation spaces, and the implementation of two large-scale spectral forcing schemes, the ABC and the non-helical and helical Euler forcings.

2.1 Numerical approach

2.1.1 Turbulence in a periodic domain

Classical Fourier-spectral algorithms (see *e.g.* [66]) solve the Navier-Stokes equations in a three-dimensional cube C in physical space with periodic boundary conditions. If the cube is large enough with respect to the integral lengthscale and the flow is homogeneous in the cube, its features are similar to ideal homogeneous turbulence ones. For the sake of simplicity let the size of C be 2π. The periodic velocity field $\boldsymbol{u}(\boldsymbol{x})$ can be expanded as an infinite Fourier series,

$$\boldsymbol{u}(\boldsymbol{x}) = \sum_{\boldsymbol{k}} \hat{\boldsymbol{u}}(\boldsymbol{k}) \mathrm{e}^{\mathrm{i}\boldsymbol{k}\cdot\boldsymbol{x}}, \tag{2.1}$$

where now $\boldsymbol{k}$ represents discrete wavevectors with integer components and

$$\hat{\boldsymbol{u}}(\boldsymbol{k}) = \frac{1}{(2\pi)^3} \int_C \boldsymbol{u}(\boldsymbol{x}) \mathrm{e}^{-\mathrm{i}\boldsymbol{k}\cdot\boldsymbol{x}} \mathrm{d}\boldsymbol{x} \tag{2.2}$$

is the Fourier coefficient of $\boldsymbol{u}(\boldsymbol{x})$ corresponding to wavevector $\boldsymbol{k}$. It is easy to prove that, since the velocity field is periodic, its Fourier coefficient $\hat{\boldsymbol{u}}(\boldsymbol{k})$ is equal to its finite-range integral transform

multiplied by $(\pi/\mathcal{L})^3$ in the limit of infinitely large $\mathcal{L}$ or if $\mathcal{L}$ is equal to an integer multiple of π, compare the definition of the finite-range Fourier transform (1.32) and the definition of the Fourier coefficient (2.2).

Note that all the results presented in section 1.1 are still valid if Fourier integral transforms are replaced by Fourier discrete transforms and integrals in spectral space are replaced by summations over discrete wavevectors. Furthermore, $\hat{\boldsymbol{u}}(\boldsymbol{k})$ can be projected onto Craya-Herring frame (see section 1.1.2),

$$\hat{\boldsymbol{u}}(\boldsymbol{k}) = u^{(1)}(\boldsymbol{k})\boldsymbol{e}^{(1)}(\boldsymbol{k}) + u^{(2)}(\boldsymbol{k})\boldsymbol{e}^{(2)}(\boldsymbol{k}) \tag{2.3}$$

with no component of $\hat{\boldsymbol{u}}$ along $\boldsymbol{e}^{(3)}$ because of the incompressibility condition $\boldsymbol{k}\cdot\hat{\boldsymbol{u}}(\boldsymbol{k}) = 0$. $R_{ij}(\boldsymbol{r})$ is periodic too, and the tensor $\hat{R}_{ij}(\boldsymbol{k}) = \langle \hat{u}_i^*(\boldsymbol{k})\hat{u}_j(\boldsymbol{k})\rangle$ represents its Fourier coefficients. The decomposition developed in section 1.1.6 for $\hat{R}_{ij}$ may be repeated here with no formal difference. In addition, the spectral densities appearing in Eq. (1.81) are now directly linked to $\hat{\boldsymbol{u}}(\boldsymbol{k})$, *i.e.*

$$e(\boldsymbol{k}) = \frac{1}{2}\langle \hat{\boldsymbol{u}}^*(\boldsymbol{k})\cdot\hat{\boldsymbol{u}}(\boldsymbol{k})\rangle, \tag{2.4}$$

$$h(\boldsymbol{k}) = \langle \hat{\boldsymbol{u}}^*(\boldsymbol{k})\cdot\hat{\boldsymbol{\omega}}(\boldsymbol{k})\rangle, \tag{2.5}$$

$$z(\boldsymbol{k}) = \frac{1}{2}\langle u^{(2)*}(\boldsymbol{k})u^{(2)}(\boldsymbol{k}) - u^{(1)*}(\boldsymbol{k})u^{(1)}(\boldsymbol{k})\rangle + \mathrm{i}\langle \Re u^{(1)}(\boldsymbol{k})\Re u^{(2)}(\boldsymbol{k}) + \Im u^{(1)}(\boldsymbol{k})\Im u^{(2)}(\boldsymbol{k})\rangle. \tag{2.6}$$

2.1.2 Numerical algorithm

The pseudo-spectral method [63, 66, 80] is the numerical spectral method we use to solve the Navier-Stokes equations through direct numerical simulations (DNS). Fourier-spectral methods consist in approximating $\boldsymbol{u}(\boldsymbol{x})$ with a truncated series in place of the infinite series (2.1), which leads to a finite number of degrees of freedom, and solving the momentum equation in Fourier space

$$\frac{\partial \hat{u}_i}{\partial t} = -P_{ij}\hat{N}_j - \nu k^2 \hat{u}_i + P_{ij}\hat{F}_j \tag{2.7}$$

(where incompressibility has already been taken into account) for the Fourier coefficients. However, the transform of the nonlinear term is a convolution product, and therefore, since it is both nonlinear and nonlocal in spectral space, it requires much computational effort. The pseudo-spectral method consists in computing the nonlinear term in the physical space, which implies going back and forth between spectral and physical spaces. In particular the Fourier coefficients of velocity and its spatial derivatives are inverse Fourier transformed, then the nonlinear term in physical space is computed over a regular grid through pointwise products, and finally its

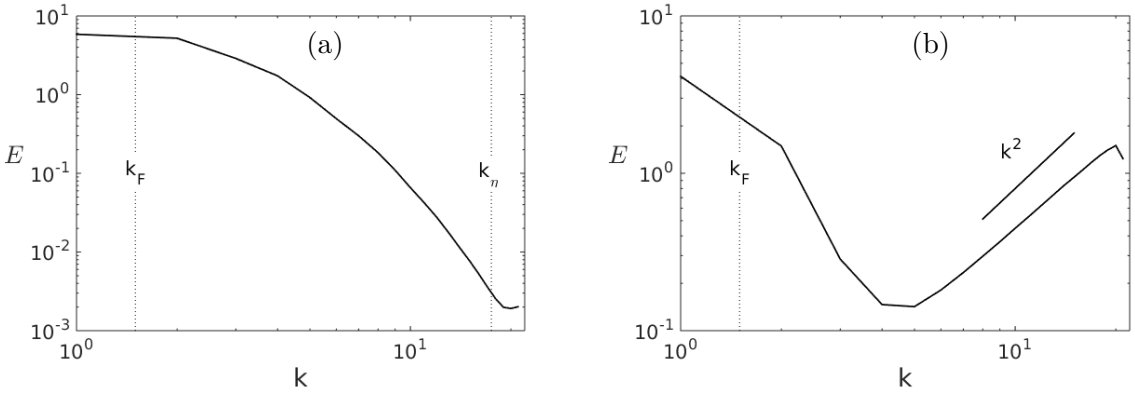

Figure 2.1: Energy spectra of statistically stationary forced turbulence computed through 64^3 resolution runs, with (a) $k_{\max}\eta = 1.2$ and (b) $k_{\max}\eta = 0.1$. k_F is the forcing wavenumber.

discrete transform is performed and is projected onto planes normal to wavevectors in order to take into account incompressibility. Since for the transforms the fast Fourier transform (FFT) algorithm is used, which strongly reduces the required computational effort, the pseudo-spectral method results to be suitable for unconfined turbulence simulations.

In our simulations the rotational form for the nonlinear term, $\boldsymbol{N} = \boldsymbol{\omega} \times \boldsymbol{u}$, is used. We also adopt the 2/3-rule for dealiasing and the third-order Adams-Bashforth (explicit multistep) scheme for time marching.

The viscous term is treated exactly and implicitly by a change of variables before time advancing. This is possible because multiplying the momentum equation (2.7) by $\mathrm{e}^{-\nu k^2 t}$ leads to

$$\mathrm{e}^{-\nu k^2 t}\frac{\partial \hat{u}_i}{\partial t} = -\mathrm{e}^{-\nu k^2 t} P_{ij}\hat{N}_j - \mathrm{e}^{-\nu k^2 t}\nu k^2 \hat{u}_i + \mathrm{e}^{-\nu k^2 t} P_{ij}\hat{F}_j, \tag{2.8}$$

so that

$$\frac{\partial \hat{v}_i}{\partial t} = -\mathrm{e}^{-\nu k^2 t} P_{ij}\hat{N}_j + \mathrm{e}^{-\nu k^2 t} P_{ij}\hat{F}_j \tag{2.9}$$

where $\hat{v}_i = \mathrm{e}^{-\nu k^2 t}\hat{u}_i$.

The criterion we use to check that we achieve good resolution is setting the simulation parameters such that $k_{\max}\eta \geq 1.2$ (see [26] for details about the effect of the grid resolution on numerical computations). $k_{\max}$ is the maximum wavenumber after dealiasing, *i.e.* $k_{\max} = n/3$, where n is the number of points used to discretize the periodic domain in each direction. When $k_{\max}\eta$ is too low, the effect of spectral truncation is also evident in energy spectra. Figure 2.1 displays the energy spectra of two 64^3 resolution statistically stationary forced simulations, corresponding to $k_{\max}\eta = 1.2$ and $k_{\max}\eta = 0.1$ respectively. In the poor resolution run, Fig. 2.1(b),

a thermalised range appears at large wavenumbers. In this range wavevectors statistically hold the same amount of energy and thus $E(k) \sim k^2$. For thermalization in spectrally truncated Euler flows see [11, 20, 42].

2.1.3 Treatment of boundary conditions

In addition to unconfined (periodic domain) simulations, we also perform confined simulations of the von Kármán flow (see Chapter 5) by coupling the pseudo-spectral algorithm to an immersed boundary method, in particular a volume penalization method. This penalization method was developed by Kolomenskiy et al. [41] and implemented by Jause-Labert et al. [15], and is briefly described in this section.

Immersed boundary methods [64, 65] consist in treating the boundary conditions, *e.g.* the presence of solid bodies, by means of an additional "penalty" term in the equations. The main advantage of this approach is that the mesh does not need to fit the solid walls, so that the flow can be computed in rather complex domains with relative ease. However, when an immersed boundary method is used in a spectral code, spectral accuracy is lost.

In the case of a penalization method [5], a penalty force of the form

$$\boldsymbol{F} = -\frac{1}{\mu}\chi\left(\boldsymbol{u} - \boldsymbol{u}_S\right) \tag{2.10}$$

is added in the momentum equation. μ is the penalization parameter, $\boldsymbol{u}_S(\boldsymbol{x}, t)$ is a prescribed velocity field which equals the boundary condition for $\boldsymbol{u}$ in the solid part $\mathcal{S}$ of the domain, and $\chi(\boldsymbol{x}, t)$ is a mask function defined as

$$\chi(\boldsymbol{x}, t) = \begin{cases} 1, & \text{if } \boldsymbol{x} \in \mathcal{S} \\ 0, & \text{otherwise.} \end{cases} \tag{2.11}$$

On one hand, $\boldsymbol{F}$ vanishes in the flow region, and therefore the original momentum equation is recovered. On the other hand, in the solid region, it depends on the penalization parameter, the boundary condition and the velocity field. The solution of the penalized problem has been proven to converge to the corresponding Navier-Stokes solution with no-slip boundary conditions and fixed bodies as $\mu \to 0$ [2].

After spectral discretization of the penalized equations, from the momentum equation (2.7) and the expression of the penalty force (2.10), one obtains

$$\frac{\partial \hat{u}_i}{\partial t} = -P_{ij}\hat{N}_j - \nu k^2 \hat{u}_i - P_{ij}\frac{1}{\mu}\widehat{\chi(u_j - u_{Sj})}. \tag{2.12}$$

In order to overcome the stability constraint for the time step [41], $\Delta t < \frac{6}{11}\mu$ for the third-order Adams-Bashforth scheme, the penalization term can be treated by the method described in [41] and tested for the Burgers' equation, *i.e.* $\widehat{\chi(u_j - u_{Sj})}$ can be estimated at the time step where the system state is unknown. Of course this makes the scheme implicit, because the product in physical space between the mask and the velocity becomes a convolution in Fourier space by property (1.4). However, while in the case of Burgers' equation one can come back to an explicit formulation by estimating the penalization term in physical space [41], in the case of Navier-Stokes equations the presence of the projector operator P_{ij} in Eq. (2.12) does not allow this.

Our code uses a splitting method to compute the nonlinear and the penalization contributions to the velocity time-derivative separately, at the cost of an additional round trip between physical and spectral spaces, see [15] for details about the implementation. As a simple illustration, in the case of a first-order scheme, this method leads to

$$\hat{u}_i(t+\Delta t) = P_{ij}\mathrm{FT}\left\{\frac{\mathrm{FT}^{-1}\left\{\hat{u}_j(t) - \Delta t P_{jl}\hat{N}_l(t)\right\} + \frac{\Delta t}{\mu}\chi(t+\Delta t)u_{Sj}(t+\Delta t)}{1+\frac{\Delta t}{\mu}\chi(t+\Delta t)}\right\} \tag{2.13}$$

where FT and FT^{-1} denote Fourier and inverse Fourier transform, and Δt is the time step.

2.2 Anisotropy detection

2.2.1 Directional spectra

In the modal decomposition of the velocity spectral tensor, see Eq. (1.81), we have retained the general $\boldsymbol{k}$ dependence. Under the assumption of axisymmetry one can consider only the dependence of the energy, helicity and polarization spectral densities upon the axial and horizontal components of the wavevector $\boldsymbol{k}$ (see for instance [32]), or upon the wavenumber k and the polar orientation θ of $\boldsymbol{k}$ with respect to the axis of symmetry [16, 34]. Therefore, in our analysis of spectral anisotropy (see Chapter 3), we shall present direction-dependent spectra, discretizing k between minimal and maximal values set by the computational box size and the resolution, and considering angular averages of spectra in five angular sectors in the interval $\theta \in [0, \pi/2]$, *i.e.* $[(i-1)\pi/10, i\pi/10]$ with $i = 1, \cdots, 5$. We call $E_i(k)$, $H_i(k)$ and $\Re Z_i(k)$ the spectra of energy, helicity and real part of polarization. They are obtained by summing the corresponding spectral densities over these sectors, *e.g.*

$$E_i(k) = C_i^k \sum_{\substack{\text{sector } i \\ \text{shell } k}} e(\boldsymbol{k}). \tag{2.14}$$

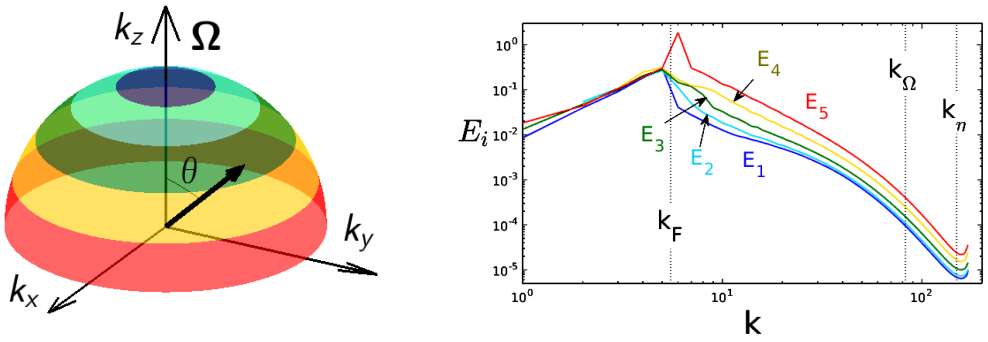

Figure 2.2: Angular sectors (left) and corresponding angle-dependent energy spectra for rotating turbulence (right). k_F is the forcing wavenumber.

The factor C_i^k is the ratio of the shell sector volume to the number of discrete wavevectors in it (if the size of C is not 2π, one also has to multiply by the wavevectors density in spectral space), and normalizes the spectra for all angular sectors such that for directionally isotropic turbulence they collapse onto the corresponding spherically-integrated spectrum, *e.g.* the $E_i(k)$ spectra collapse on $E(k)$. Figure 2.2 shows direction-dependent energy spectra for strongly rotating turbulence together with a representation of the related angular sectors. The limited number of sectors is imposed by the need of a minimal number of discrete wavevectors in every sector for achieving decent sample size from DNS data. Even so, in the small wavenumbers, very few wavevectors lie within the averaging regions.

The energy spectrum is also used to compute the integral lengthscale, defined as the integral of the longitudinal velocity correlation divided by the mean squared velocity, which under the isotropy assumption can be shown [49] to be equal to

$$L = \frac{3}{4}\pi \frac{\int E(k)/k \, \mathrm{d}k}{\int E(k) \, \mathrm{d}k}. \tag{2.15}$$

One could estimate L by summations over k-centered shells:

$$L = \frac{3}{4}\pi \frac{\sum E(k)/k}{\sum E(k)} \tag{2.16}$$

where k are integer values identifying the shells. However, since in general small wavevectors hold much more energy than large ones, this estimation of L essentially depends on the small wavenumbers part of the energy spectrum. Therefore, since the integer values k used in Eq. (2.16) significantly differ from the right wavenumbers at large scales, an error arises. In order to improve the estimation of L, we compute the average wavenumbers in every shell and use them instead

of the integer values k. For example, for the spectrum shown in Fig. 2.1(a) Eq. (2.16) leads to a 20% error with respect to the improved estimation using average wavenumbers.

Using the average values of the wavenumbers for plotting the spectra also improves their appearance, but the difference is slight.

If a statistically stationary state is reached and velocity decorrelates rapidly in time [49], ensemble averages can be estimated through time averages. Spectra presented in Chapter 3 are obtained by time averaging the instantaneous spectra.

2.2.2 Statistics in separation space

We also compute the quantities apearing in the Kármán-Howarth-Monin equation, *i.e.* $R(\boldsymbol{r})$, $\boldsymbol{\mathcal{F}}(\boldsymbol{r})$, $\nu\nabla^2 R(\boldsymbol{r})$ and $\Phi(\boldsymbol{r})$, see Eq. (1.88), and plot their distributions in the (ρ-ζ) plane, where ρ and ζ are the horizontal (normal to x_3 axis) and vertical (parallel to x_3 axis) components of $\boldsymbol{r}$. The considered separation vectors $\boldsymbol{r} = \boldsymbol{x} - \boldsymbol{x}'$ lie along the four azimuthal directions $\varphi = 0, \pi/2, \pi, 3\pi/4$ and are such that $|\boldsymbol{r}| \leq r_{\max} \leq \pi$ ($r_{\max}$ is a suitably defined value) and such that $\boldsymbol{x}$ and $\boldsymbol{x}'$ correspond to numerical grid points. For example, in the plane ($r_2 = 0$, r_1, $r_3 \geq 0$), $\boldsymbol{r} = \frac{2\pi}{n}[i, 0, k]$ with $i, k = 0, ..., n/2 - 1$ where n is the numerical resolution.

First, for every separation vector $R(\boldsymbol{r}, t)$ and $\boldsymbol{\mathcal{F}}(\boldsymbol{r}, t)$ are directly obtained through averaging in physical space and possibly by averaging in time. Values corresponding to 512^3 equally spaced nodes in physical space are used to average, independently of the resolution.

Then, $\nu\nabla^2 R(\boldsymbol{r})$ is computed through a second-order finite differences Laplace operator over a five-point stencil in the same nodes where $R(\boldsymbol{r})$ and $\boldsymbol{\mathcal{F}}(\boldsymbol{r})$ values are available, and $\nabla \cdot \boldsymbol{\mathcal{F}}(\boldsymbol{r})$ is computed through first-order finite differences over a staggered grid. Of course, axisymmetry is taken into account in the estimation of these quantities. The simplest way to do so is expressing the Laplacian and divergence operators in the cylindrical frame (ρ,φ,ζ):

$$\nabla^2 R = \frac{1}{\rho}\frac{\partial}{\partial \rho}\left(\rho \frac{\partial R}{\partial \rho}\right) + \frac{\partial^2 R}{\partial \zeta^2} \tag{2.17}$$

$$\nabla \cdot \boldsymbol{\mathcal{F}} = \frac{1}{\rho}\frac{\partial}{\partial \rho}\left(\rho F_\rho\right) + \frac{\partial F_\zeta}{\partial \zeta}. \tag{2.18}$$

Because of axisymmetry the analysis of these quantities can be restricted to the (ρ,ζ) plane and to positive values of both ρ and ζ. Axial symmetry and the definitions of R and $\boldsymbol{\mathcal{F}}$,

Eqs. (1.83) and (1.87), can further be used to obtain the following symmetries:

$$\left[\frac{\partial^{2m+1}}{\partial\theta^{2m+1}}R\right]_{\theta=0} = \left[\frac{\partial^{2m+1}}{\partial\theta^{2m+1}}\mathcal{F}_r\right]_{\theta=0} = \left[\frac{\partial^{2m+1}}{\partial\theta^{2m+1}}\left(\nabla\cdot\boldsymbol{\mathcal{F}}\right)\right]_{\theta=0} = 0 \tag{2.19}$$

$$\left[\frac{\partial^{2m}}{\partial\theta^{2m}}\mathcal{F}_\theta\right]_{\theta=0} = \left[\frac{\partial^{2m}}{\partial\theta^{2m}}\mathcal{F}_\varphi\right]_{\theta=0} = 0 \tag{2.20}$$

$$\left[\frac{\partial^{2m+1}}{\partial\theta^{2m+1}}R\right]_{\theta=\pi/2} = \left[\frac{\partial^{2m+1}}{\partial\theta^{2m+1}}\mathcal{F}_r\right]_{\theta=\pi/2} = \left[\frac{\partial^{2m+1}}{\partial\theta^{2m+1}}\mathcal{F}_\varphi\right]_{\theta=\pi/2} = \left[\frac{\partial^{2m+1}}{\partial\theta^{2m+1}}\left(\nabla\cdot\boldsymbol{\mathcal{F}}\right)\right]_{\theta=\pi/2} = 0 \tag{2.21}$$

$$\left[\frac{\partial^{2m}}{\partial\theta^{2m}}\mathcal{F}_\theta\right]_{\theta=\pi/2} = 0 \tag{2.22}$$

for $m \geq 0$ (the zero-th order derivatives are included, *e.g.* $\mathcal{F}_\theta = 0$ in $\theta = 0$).

The computations of statistics in separation space have been validated through the isotropic turbulence relationships [49]

$$\langle \delta u_i \delta u_i \rangle = 4\int \left(1 - \frac{\sin kr}{kr}\right) E(k)\,\mathrm{d}k \tag{2.23}$$

$$R = 2\int \frac{\sin kr}{kr} E(k)\,\mathrm{d}k \tag{2.24}$$

$$\langle u_r(\boldsymbol{x}) u_r(\boldsymbol{x}') \rangle = 2\int \frac{\sin kr - kr\cos kr}{k^3 r^3} E(k)\,\mathrm{d}k \tag{2.25}$$

and through the Kármán-Howarth-Monin equation (1.88).

2.3 Forcing schemes

When performing direct numerical simulations of homogeneous turbulence, one would like to force turbulence for two reasons. First, it permits to reach higher Reynolds numbers than in freely decaying turbulence. Second, under some assumptions [49], statistics can be obtained with time-averaging rather than ensemble averaging, which would be very costly considering the fact that refined statistics require a large number of samples. Also, forcing turbulence can be useful to represent—through a model force—the effect of forcing mechanisms in more complex turbulent flows, and to reproduce, without simulating complete complex systems, situations of actual flows, such as *e.g.* injection of energy by large-scale instabilities in atmospheric flows, or

stirring devices in industrial flows. For instance, the well-known von Kármán experiment (see Chapter 5) consists of two counter rotating rotors that not only inject energy at large scales in the flow, but also helicity.

In order to study statistically stationary turbulence, many velocity forcing schemes have been used so far in numerical simulations. In homogeneous spectral simulations, large-scale forcing methods consist in providing energy to the low wavenumber modes, which is consistent with the concept of Richardson cascade, see *e.g.* [1, 26, 76]. For example, considering a working external force $\boldsymbol{F}$ which is a linear combination of sines and cosines with wavevectors of modulus lesser than or equal to k_F, by Eqs. (1.41), (1.50) and (1.53) the forcing contribution in both Craya's equation and energy spectral density equation vanishes at wavenumbers greater than k_F. Therefore, in statistically stationary turbulence, this external force feeds low wavenumbers and then part of this energy is transferred to larger wavenumbers through the nonlinear term $T(\boldsymbol{k})$ in the energy spectral density equation (1.51). In other words, considering that $\nu k^2 e(\boldsymbol{k}) \geq 0$ in Eq. (1.51), $T(\boldsymbol{k})$ is negative at wavenumbers lesser or equal to k_F and positive at wavenumbers greater than k_F.

However, since only a finite number of wavenumbers is excited by large-scale spectral forcing schemes, anisotropy may develop at low wavevenumbers and eventually branch out to smaller scales. Detecting this kind of anisotropy requires direction-dependent statistics, and is the main purpose of Chapter 3. In this section we describe in detail the two forcing schemes that we use for such investigation, the non-helical and the helical Euler forcing method and the ABC forcing method [37, 52, 68], as well as their implementation.

2.3.1 ABC forcing

The ABC forcing consists in adding in the momentum equation (1.27) an external force $\boldsymbol{F}_{\mathrm{ABC}}$ corresponding to an Arnold-Beltrami-Childress flow (see *e.g.* [19]):

$$\boldsymbol{F}_{\mathrm{ABC}} = [B\cos(k_F\, y) + C\sin(k_F\, z)]\,\hat{\boldsymbol{\imath}} + [C\cos(k_F\, z) + A\sin(k_F\, x)]\,\hat{\boldsymbol{\jmath}} + [A\cos(k_F\, x) + B\sin(k_F\, y)]\,\hat{\boldsymbol{k}}, \quad (2.26)$$

for a given large scale wavenumber k_F. Since $\boldsymbol{F}_{\mathrm{ABC}}$ is an eigenfunction of the curl operator with eigenvalue k_F, the corresponding contribution (1.80) in the helicity equation (1.78) is nonzero and thus the ABC forcing injects helicity, in addition to energy, in the flow. For the sake of simplicity let the constants A, B and C be equal to 2. Then in Fourier space the expression

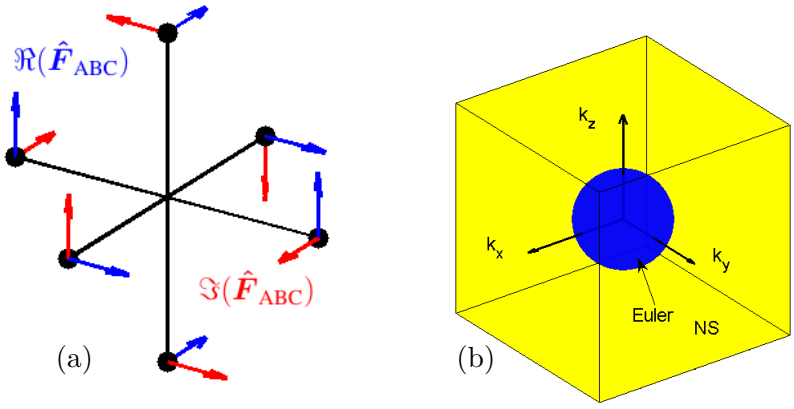

Figure 2.3: (a) ABC, and (b) Euler forcing schemes in spectral space.

(2.26) becomes

$$\begin{aligned}
\hat{\boldsymbol{F}}_{\rm ABC} &= [0 \quad \pm i \quad 1] \text{ if } \boldsymbol{k} = [\mp k_F \quad 0 \quad 0] \\
\hat{\boldsymbol{F}}_{\rm ABC} &= [1 \quad 0 \quad \pm i] \text{ if } \boldsymbol{k} = [0 \quad \mp k_F \quad 0] \\
\hat{\boldsymbol{F}}_{\rm ABC} &= [\pm i \quad 1 \quad 0] \text{ if } \boldsymbol{k} = [0 \quad 0 \quad \mp k_F] \\
\hat{\boldsymbol{F}}_{\rm ABC} &= [0 \quad 0 \quad 0] \quad \text{otherwise.}
\end{aligned} \tag{2.27}$$

In Fig. 2.3(a) $\boldsymbol{F}_{\rm ABC}$ is represented in spectral space.

In terms of flow structure, the large-scale flow induced by the ABC forcing is very much like Taylor-Green vortices, but extended to three dimensions. More precisely, $\boldsymbol{F}_{\rm ABC}$ induces permanent large-scale curved helical rotors associated with a single wavelength.

Thus, $\hat{\boldsymbol{F}}_{\rm ABC}$ is a steady force that excites only six modes and injects a given amount of helicity. In rapidly rotating turbulence, an inverse energy cascade can arise so that it can be difficult to reach a statistically stationary state [72]. Indeed, similarly to ABC-forced rotating simulations present in the literature, for the ABC-forced rotating run analyzed in Chapter 4, spectra are computed by time-averaging, although a statistically stationary state is not reached.

2.3.2 Non-helical and helical Euler forcing

In order to overcome some of the limitations of ABC forcing, we use the Euler forcing [68], which can be thought of as introducing three-dimensional large-scale vortices that evolve in time by interacting with each other—but not with the other scales of the flow—in a manner closer to actual inviscid turbulent nonlinear dynamics. Unlike the ABC forcing, the external force induced by the Euler scheme is unsteady and chaotic, the number of excited modes depends on k_F, and the amount of injected helicity can be controlled.

We now describe in detail how the Euler forcing is implemented. The Euler-forced simulations are inspired by the truncated Euler dynamics [11, 20, 42]: the lowest-wavenumbers modes, corresponding to wavevectors $\boldsymbol{k}$ such that $0 \leq |\boldsymbol{k}| \leq k_F$ (k_F is the largest forcing wavenumber), obey the three-dimensional incompressible Euler equations (possibly with background rotation) and are independent of the other modes. Of course the modes corresponding to wavenumbers $\boldsymbol{k}$ such that $|\boldsymbol{k}| > k_F$ are solutions of the incompressible Navier-Stokes equations and also depend on the modes in the Euler forcing sphere. Figure 2.3(b) illustrates the forced and unforced regions in spectral space. For the spherically truncated inviscid system, we compute the quadratic nonlinear term through a convolution in Fourier space so that no aliasing error arises.

Since energy and helicity are conserved within every nonlinear triadic interaction (see sections 1.1.3 and 1.1.4), in this truncated system total energy and helicity are conserved as well. Background rotation does not affect this conservation property, since the Coriolis force has vanishing contributions in both energy and helicity evolution equations (for the truncated system as well as for every non-linear triadic interaction), see section 1.3. Of course, while in spectral methods the spatial operators do not introduce a numerical error (and thus do not modify the total energy and helicity in the Euler system), the temporal error affects energy and helicity if a non-conservative scheme is employed. Since we use the classical fourth-order Runge-Kutta scheme, this is our case. However we verified that this temporal error is negligible in our simulations, as shown by Fig. 2.4 which plots the Euler system energy dissipated or produced as a function of time for the simulation corresponding to the spectrum of Fig. 2.1(a). Note that, because of the conservative dynamics of the lowest modes $|\boldsymbol{k}| \leq k_F$, the Euler forcing prevents the development of any inverse cascade.

If energy is concentrated at large scales in the initial spectrum, the transient dynamics of spectrally truncated 3D incompressible Euler equations behaves like dissipative Navier-Stokes equation and displays a K41 scaling [20]. However, we are interested here in the statistically stationary solution (statistical or absolute equilibrium). The exact solutions for the statistical equilibrium energy and helicity spectra are [42]

$$E(k) = \frac{4\pi}{\alpha} \frac{k^2}{1 - \left(\frac{\beta}{\alpha}\right)^2 k^2}, \quad H(k) = \frac{8\pi\beta}{\alpha^2} \frac{k^4}{1 - \left(\frac{\beta}{\alpha}\right)^2 k^2}, \tag{2.28}$$

where α and β depend on the total energy and helicity and are constrained by the realizability condition $|h(\boldsymbol{k})| \leq 2\,|\boldsymbol{k}|\,e(\boldsymbol{k})$ such that $\alpha > 0$ and $|\beta k_F| \leq \alpha$. At a given truncation wavenumber, the solution depends only on the constant total energy and helicity. Therefore, there is only

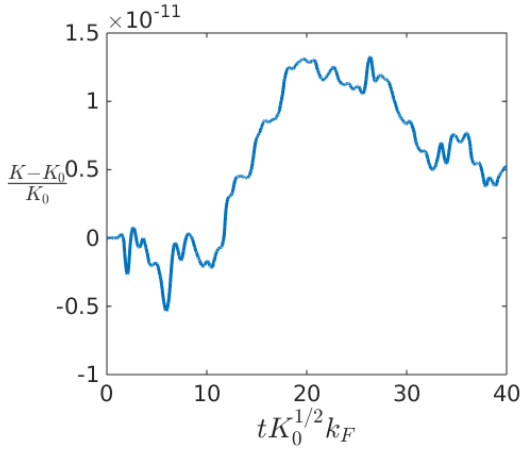

Figure 2.4: Energy dissipated or produced by temporal numerical error in the spherically truncated Euler system as a function of time t. $k_F = 1.5$ is the truncation wavenumber, K and K_0 are the energy and the initial energy.

one independent non-dimensional parameter, *e.g.* the relative helicity (the possible presence of rotation, which represents an additional degree of freedom, is not discussed here). Figure 2.5 shows the exact and numerical spectra for different relative helicities with $k_F = 5.5$. If $H_{\text{rel}} = 0$, every wavevector holds the same amount of energy, and the energy spectrum is therefore proportional to k^2. As the relative helicity increases, large wavenumber energy and helicity densities become larger and larger with respect to their low wavenumber counterparts.

Note that, with respect to previous works using the Euler forcing [61, 68], our implementation allows to control helicity injection and to vary k_F arbitrarily, so that it is not restricted to non-helical turbulence and $k_F = 1.5$. In Euler-forced runs, Fourier coefficients for the forcing wavenumbers are initialized as a random homogeneous solenoidal velocity field with a given energy spectrum. The mean helicity can be computed as $\sum_{\boldsymbol{k}} h(\boldsymbol{k})$, where the helicity density $h(\boldsymbol{k}) = \hat{\boldsymbol{u}}^*(\boldsymbol{k}) \cdot \hat{\boldsymbol{\omega}}(\boldsymbol{k})$ can be recast as $h(\boldsymbol{k}) = 2\,\boldsymbol{k} \cdot (\Re\hat{\boldsymbol{u}} \times \Im\hat{\boldsymbol{u}})$. In helical Euler-forced simulations, the initial values of the forced modes are modified in order to obtain the maximal achievable helicity densities without changing the energy densities, *i.e.*

$$\hat{\boldsymbol{u}}(\boldsymbol{k}) = e(\boldsymbol{k})^{1/2}\, \mathrm{e}^{\mathbf{i}\,\gamma} \left(\boldsymbol{e}^{(1)}(\boldsymbol{k}) + \mathrm{i}\boldsymbol{e}^{(2)}(\boldsymbol{k}) \right) \tag{2.29}$$

where γ is a uniformly distributed random angle so that the initial Euler field is homogeneous.

Since the relative helicity in a helical forced simulation depends on the prescribed energy spectrum, we use different shapes for the initial energy spectrum in order to achieve different relative helicities. The considered spectrum is $E(k) = k^p e^{-p/2(k/k_F)^2}$, with a maximum at $k = k_F$

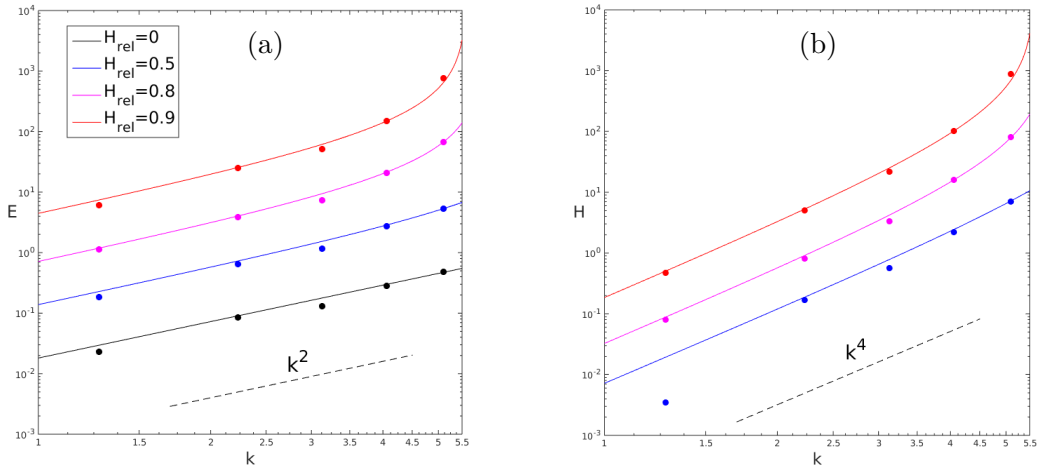

Figure 2.5: Exact energy and helicity spectra of the spherically truncated Euler system for different relative helicities (continuous line) and DNS time-averaged spectra (markers). The truncation wavenumber is $k_F = 5.5$.

and different possible values for p.

In non-helical Euler-forced simulations, we ensure exact vanishing net helicity in the initial field by adjusting angles between the real and imaginary parts of all the forcing modes, so that $\sum_{\boldsymbol{k}} h(\boldsymbol{k}) = 0$.

Our implementation of the truncated Euler equations has been validated against the spectra (2.28) predicted by Kraichnan [42], as shown in Fig. 2.5. The agreement between analytical spectra and DNS points is good at all relative helicities.

In order to verify that the system is ergodic, we compared two simulations initialized with different energy spectra but same values of k_F and $H_{\rm rel}$ and checked that the same spectra were obtained through time averages, for the forced wavenumbers as well as for the unforced ones. It is understood, however, that some special initial values for the Euler modes would not lead to the same statistically stationary solution as the initializations described above. For example, if only one mode in the Euler sphere is nonzero, no triadic interaction happens and thus energy does not spread out to the other modes. Another special case is when some or all the largest wavenumber modes are initialized with maximal helicity, *i.e.* $|h(\boldsymbol{k})| = 2ke(\boldsymbol{k})$ (see the realizability condition, Eq. (1.74)), and all the other modes vanish. In this case, while interactions among maximal wavenumber modes are possible (if the corresponding wavevectors form a triad), no interaction with the other modes is possible. This can be understood by observing that transfering an amount of energy from a maximal wavenumber mode to a lower wavenumber mode would necessarily cause a decrease in the global helicity, which on the contrary

is an inviscid invariant.

2.3.3 Shell-Euler-forcing

In the presence of background rotation, the Euler and ABC forcing schemes give rise to substantially different physical systems. Indeed, as already explained in sections 2.3.1 and 2.3.2, while in Euler-forced runs the modes in the spherically truncated system evolve independently of the other modes, the low wavevectors modes in ABC-forced runs are coupled with all the other modes. As a consequence, if rotation is large enough, energy is allowed to cascade backwards. This inverse cascade (see *e.g.* [72]), manifests as an increase of the energy in the smallest wavenumbers, and as a consequence the flow is not statistically stationary.

In Chapter 4 we compare rotating runs forced through ABC and Euler forcings. Then, because of the presence of rotation, one may wonder if the differences observed in the simulations depend mainly on the intrinsic nature of the schemes or on the presence of an inverse cascade in ABC-forced runs. For this reason, in order to investigate the role of an inverse cascade, we also implemented a helical shell-Euler-forced scheme, in which the truncated system includes only modes corresponding to wavenumbers k such that $4.6 \leq k \leq 5.4$. In order to verify that, within the shell, energy can reach any mode starting from any other mode through triadic interactions, we performed a simulation with large initial energy for only one mode ($\boldsymbol{k} = [2, 3, 4]$) and small initial energy for all the other modes. Of course it makes no sense to initialize with exactly zero energy all the modes but one, because in that case no triadic interaction would exist. Energy densities are plotted as functions of time in Fig. 2.6, and show that all modes finally receive energy so that all modes are interconnected through nonlinear triadic interactions.

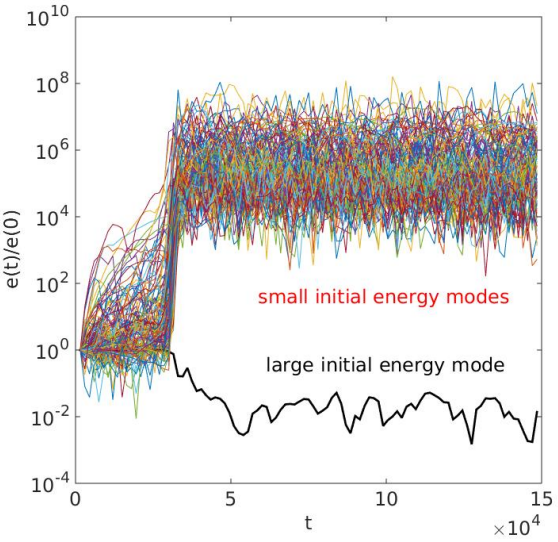

Figure 2.6: Energy densities as functions of time divided by their initial value.

Chapter 3

Anisotropy induced by forcing

In this chapter we study the effect of large-scale spectral forcing on the scale-dependent anisotropy of the velocity field in direct numerical simulations of homogeneous incompressible turbulence expected to be isotropic. This investigation also is a necessary pre-requisite before assessing the global anisotropic structure of forced rotating turbulence, which is the aim of Chapter 4. The considered forcing methods are the steady ABC single wavenumber scheme and the unsteady non-helical or helical Euler scheme, both described in detail in Chapter 2. The results are also compared with high resolution data obtained with the negative viscosity scheme. Our fine-grained characterization of anisotropy is based on the modal decomposition of the spectral velocity tensor introduced in Chapter 1. In particular we measure energy, helicity and polarization angle-dependent spectra. We show that anisotropy can be detected in most cases and that its characteristics depend on the forcing nature, on the value of the forcing wavenumber k_F, and on the relative helicity of the spherically truncated system in the case of helical Euler forcing.

3.1 Distant triadic interactions

According to the classical Kolmogorov K41 theory [40] for turbulent flows at asymptotically large Reynolds number, the large-scale dynamics should affect small scales statistical properties only through the energy production rate, *i.e.* small scales should be statistically independent of large scales, and have a universal behaviour. This assumption is referred to as the local isotropy hypothesis and has been studied by many authors but it is still debated. On the one hand, some authors agree about energy cascading from large to small scales mainly through local triadic interactions in Fourier space. On the other hand, other works showed that the energy-containing scales directly affect the small scales dynamics through distant triadic interactions.

Such nonlinear interactions correspond to wavenumber triangles with very large scale separation.

In particular, [13, 14] analyzed the nonlinear interactions among Fourier modes in a single triad with a wavenumber in the energy-containing scales: since this triad contribution does not vanish at infinite scale separation, the small scales may not be independent of large scales at asymptotically large Reynolds number. Yeung & Brasseur (1991) [84] confirmed this by observing small scale anisotropy in numerical simulations with strongly anisotropic large scale forcing. Since small scale anisotropy was found to increase with the wavenumber and to be consistent with the distant triad equations, local anisotropy should therefore persist at high Reynolds number. The local isotropy hypothesis was also shown to be violated in homogeneous sheared turbulence by the measurement of statistical quantities in the physical space in direct numerical simulations (DNS) [69, 70] and in experiments [74]. The detailed structure of small scales in highly anisotropically forced turbulence was also investigated by [85] in both Fourier and physical space. Anisotropic redistribution of energy and phase in high wavenumber shells was predicted and observed in DNS. In particular, a reduction of energy was detected in the directions of the forcing wavenumbers.

In any case, the study of anisotropic turbulence and of its scale-dependent features through classical Fourier analysis requires to disentangle the effect of physical sources of anisotropy from those of other artificial mechanisms, like energy and helicity production in forced simulations. Identifying and quantifying the anisotropy induced by some widely used forcing schemes in turbulence intended to be isotropic is our first concern. Note that, while in [84, 85] an explicitly and highly anisotropic forcing was used, we investigate here the unwanted intrinsic anisotropy of large scale spectral forcing schemes. Our second concern is to investigate homogeneous non-helical and helical forced turbulence subject to a background rotation, by characterizing its scale- and angle-dependent anisotropy (Chapter 4). The motivation comes for instance from previous studies of freely decaying rotating turbulence [25], in which a refined anisotropic characterization was absolutely required to understand the subtle effect of the Coriolis force on each scale of the flow. However, the drop in Reynolds number was severe due to dissipation, so that forced rotating turbulence should be considered.

3.2 Performed simulations

Except for the run forced through negative viscosity (for which only one velocity field is available), statistics of all the runs in this chapter and in Chapter 4 were obtained by time-averaging

Run	Forcing	k_F	$k_{\max}\eta$	k_η	Re^λ	Re^L	$H_{\rm rel}$	Resolution
A_{nh}	non-hel.	5.5	1.20	142	82.4	239	-2.74E-3	512^3
A_h^1	helical	5.5	1.22	140	81.3	219	0.451	512^3
A_h^2	helical	5.5	1.19	143	81.7	210	0.617	512^3
A_{ABC}	ABC	5	1.38	123	81.9	216	0.643	512^3
B_h	helical	3.5	1.22	139	115	396	0.617	512^3
B_{ABC}	ABC	3	1.45	117	116	397	0.622	512^3
C_{nh}^1	non-hel.	1.5	2.71	62.6	110	432	9.61E-3	512^3
C_{nh}^2	non-hel.	1.5	1.23	138	191	1208	7.38E-3	512^3
C_h^1	helical	1.5	2.19	77.5	136	640	0.201	512^3
C_h^2	helical	1.5	1.29	132	213	1469	0.227	512^3
D_{nv}	neg. visc.	2.5	1.94	498	430	5587	8.22E-4	2048^3

Table 3.1: Parameters used in the non-rotating simulations: k_F is the maximal forcing wavenumber, $k_{\max}$ is the maximal resolved wavenumber (after dealiasing), η is the Kolmogorov lengthscale and $k_\eta = 1/\eta$. Re^λ and Re^L are Reynolds numbers based on the Taylor scale λ and on the longitudinal integral lengthscale L respectively. $H_{\rm rel}$ refers to global relative helicity, *i.e.* in Euler-forced runs it includes both the modes in the truncated system and the modes corresponding to wavenumbers outside the Euler sphere. Letters A, B, C and D indicate different sets of non-rotating runs at decreasing k_F, subscripts $_{\rm nh}$, $_{\rm h}$, $_{\rm ABC}$ and $_{\rm nv}$ stand for non-helical Euler, helical Euler, ABC and negative viscosity forcing, respectively.

over at least one eddy-turnover time after the statistically stationary state was reached. Table 3.1 reports the parameters of the non-rotating forced runs considered in this chapter.

For the runs in set A, $k_F = 5.5$ (Euler forced runs) and 738 modes are in the Euler sphere, or $k_F = 5$ (run A_{ABC}, ABC forcing) involving only 6 modes, as in all ABC-forced runs. To allow a close comparison between all runs of the A series, we have ensured that the flow regimes are the same in terms of Reynolds numbers. While in run A_{nh} (non-helical Euler forced) the largest-wavenumber forcing modes contain the same energy as the lowest-wavenumber ones, in run A_h^1 (helical Euler forcing) the 48 largest-wavenumber modes (among 738 forcing modes) hold 15% of the total energy. In comparison, in run A_h^2 (highly helical Euler forcing) the 48 largest-wavenumber modes hold 92% of the kinetic energy in the Euler sphere and the relative

helicity is nearly equal to that of run A_{ABC}.

As for runs in set B, run B_h is a helical Euler-forced run with $k_F = 3.5$ and large relative helicity, and run B_{ABC} is an ABC-forced run with $k_F = 3$. Similarly to A_h^2, in run B_h the 8 largest-wavenumber modes (among 178 forcing modes) hold 81% of the Euler field energy, and the relative helicity is comparable to that of run B_{ABC}.

The non-helical and helical Euler forced runs in set C at $k_F = 1.5$ allow to investigate the dependence on Reynolds number. $k_F = 1.5$ is the lowest possible forcing wavenumber allowing non-linear interactions in the truncated system, which leads to 18 forcing modes.

Finally, run D_{nv} is forced through the negative viscosity method and reaches the largest Reynolds number in the considered simulations, *i.e.* $Re^\lambda = 430$. Since $k_F = 2.5$, 80 modes are forced. These data are provided by Kaneda's group [38]. Only one instantaneous velocity field is available and—in the absence of time-averaging—the resulting spectra are not as smooth as those from the other runs.

In terms of numerical resolution of the large scales, we note that the choice of k_F affects the integral lengthscale L, so that a possible effect of numerical confinement can appear. For instance, [50] studied this in isotropic turbulence and [77] in the context of the Richtmyer-Meshkov instability. Both noticed that the large scales—or equivalently the energy spectrum close to its maximum—are sensitive to confinement effects if L becomes larger than 10% of the computational domain size. However, [50] and [77] conclude that confinement has no effect on small-scale statistics, which is the object of our study. In any case, all runs in sets A and B satisfy the constraint $L \leq 10\%2\pi$. For runs in set C at $k_F = 1.5$, L is between 16% and 19% of the box size, only slightly larger than the recommanded threshold.

3.3 Energy spectra and energy directional anisotropy

Figure 3.1 shows the spherically integrated kinetic energy spectra for runs in sets A, B and C. The forcing wavenumber appears clearly as a marked peak in Figs. 3.1(a) and (b) ($k_F \simeq 5$ and $k_F \simeq 3$). In Fig. 3.1(c) at $k_F = 1.5$, all the forcing wavevectors are included in the smallest shell, so that no energy peak is visible. However, a weak disturbance in the spectral slope appears close to the forcing wavenumber. The Kolmogorov inertial scaling $k^{-5/3}$ appears in a wider spectral range than in Figs. 3.1(a) and (b) due to higher Reynolds numbers. In all of these three figures, the presence of helicity in the forcing, and thereby of a helicity cascade, modifies the kinetic energy spectral scaling at wavenumbers slightly larger than k_F. In particular, in helical

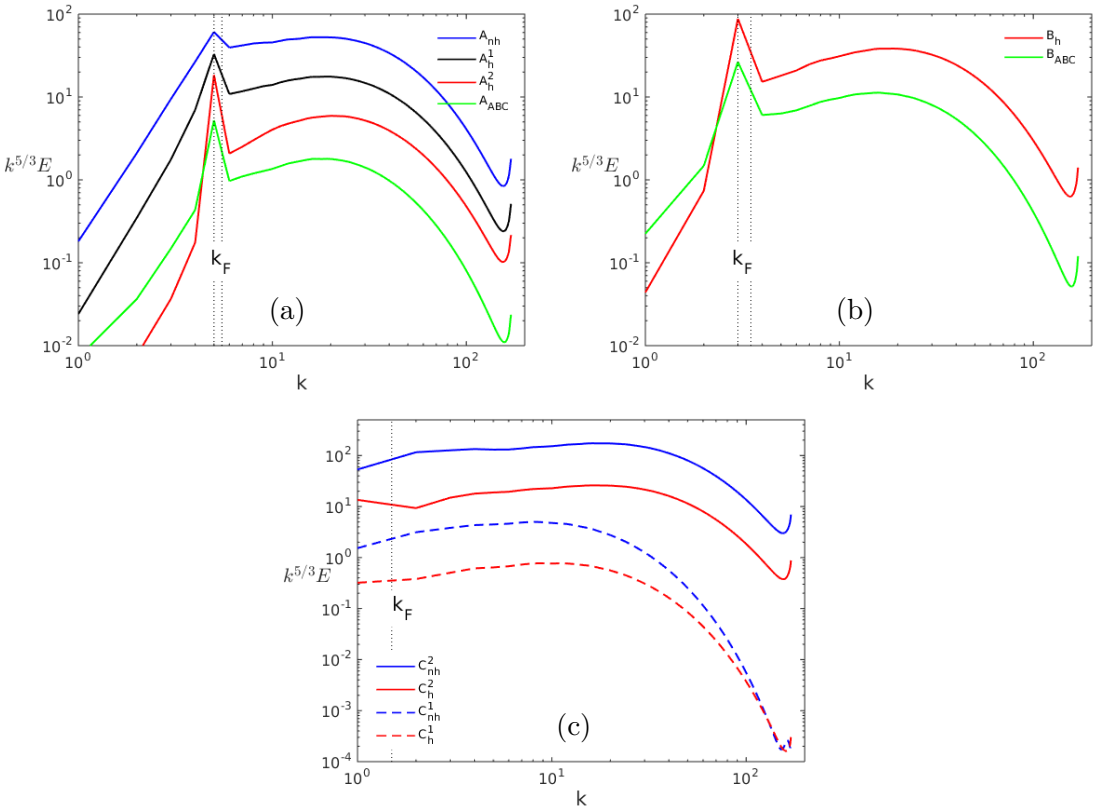

Figure 3.1: Spherically integrated kinetic energy spectra: (a) for runs in set A ($k_F \simeq 5$); (b) for runs in set B ($k_F \simeq 3$); (c) for runs in set C ($k_F = 1.5$). Spectra are shifted vertically for better view, and are compensated by the Kolmogorov inertial scaling $k^{5/3}$. k_F indicates the forcing wavenumber, as in the following plots.

runs the energy spectra are flatter (and the compensated spectra have a larger slope) in a small range neighbouring k_F.

Figure 3.2 shows the direction-dependent kinetic energy spectra $E_i(k)$ for runs of sets A, B and D. At first glance, over these logarithmic plots, the inertial and small scales are isotropic since all the curves at different orientations collapse on the spherically integrated spectrum $E(k)$, independently of the forcing method. Only in a vicinity of the forcing wavenumber, at large scales, does one observe a separation between the curves. This can be both attributed to less accurate sampling at low wavenumbers—although time-averages are used—and to the forcing. Spectra of runs $\mathrm{A_{ABC}}$ and $\mathrm{B_{ABC}}$ (Figs. 3.2a-b) seem to be more prone to this departure from isotropy over almost a decade of wavenumbers about the forcing one.

We however wish to focus more closely on the departure of the spectra from isotropy by investigating the relative difference between any directional spectrum and the spherically-integrated spectrum, computed as $\Delta E_i(k) = \left(E_i(k) - E(k)\right)/E(k)$ for $i = 1, \cdots, 5$. This quantity is plotted in Figs. 3.3 (set A), 3.4 (set B), 3.5 (set C) and 3.6 (set D).

A quick observation of these figures shows that large-scale directional anisotropy develops in several runs. More specifically, one observes that:

1. for the same values of k_F and Re^λ, the Euler-forced runs display an increasing anisotropy as their relative helicity increases (compare runs $\mathrm{A_{nh}}$, $\mathrm{A_h^1}$ and $\mathrm{A_h^2}$ [Fig. 3.3(a)-(c)]);

2. for similar values of k_F, H_{rel} and Re^λ, the anisotropy is stronger in ABC-forced than in Euler-forced runs (compare runs $\mathrm{A_h^2}$ and $\mathrm{A_{ABC}}$ [Fig. 3.3(c) and 3.3(d)], or runs $\mathrm{B_h}$ and $\mathrm{B_{ABC}}$ [Fig. 3.4(a) and 3.4(b)]).

These results can be interpreted by considering the number of sufficiently excited modes in each run: the lower this number, the more anisotropy develops. This explains straightforwardly the aforementioned item 2. In fact, the anisotropy level is the strongest in the ABC-forced runs since the ABC force excites directly only six modes, four in the horizontal sector and one in each vertical sector (see equation (2.27)). For runs $\mathrm{A_{ABC}}$ (Fig. 3.3d) and $\mathrm{B_{ABC}}$ (Fig. 3.4b), the k_F-centered horizontal and vertical sectors hold more energy than the others. Nevertheless the opposite happens at small scales, which is consistent with the numerical and theoretical results given by [13, 14, 84, 85] for highly anisotropic forcing as recalled in section 3.1.

Similarly, item 1 above can be explained by the fact that, when net helicity is large in the truncated Euler dynamics, most of the energy remains concentrated in the largest wavenumbers so that only the corresponding modes are significantly excited by the forcing scheme. Therefore,

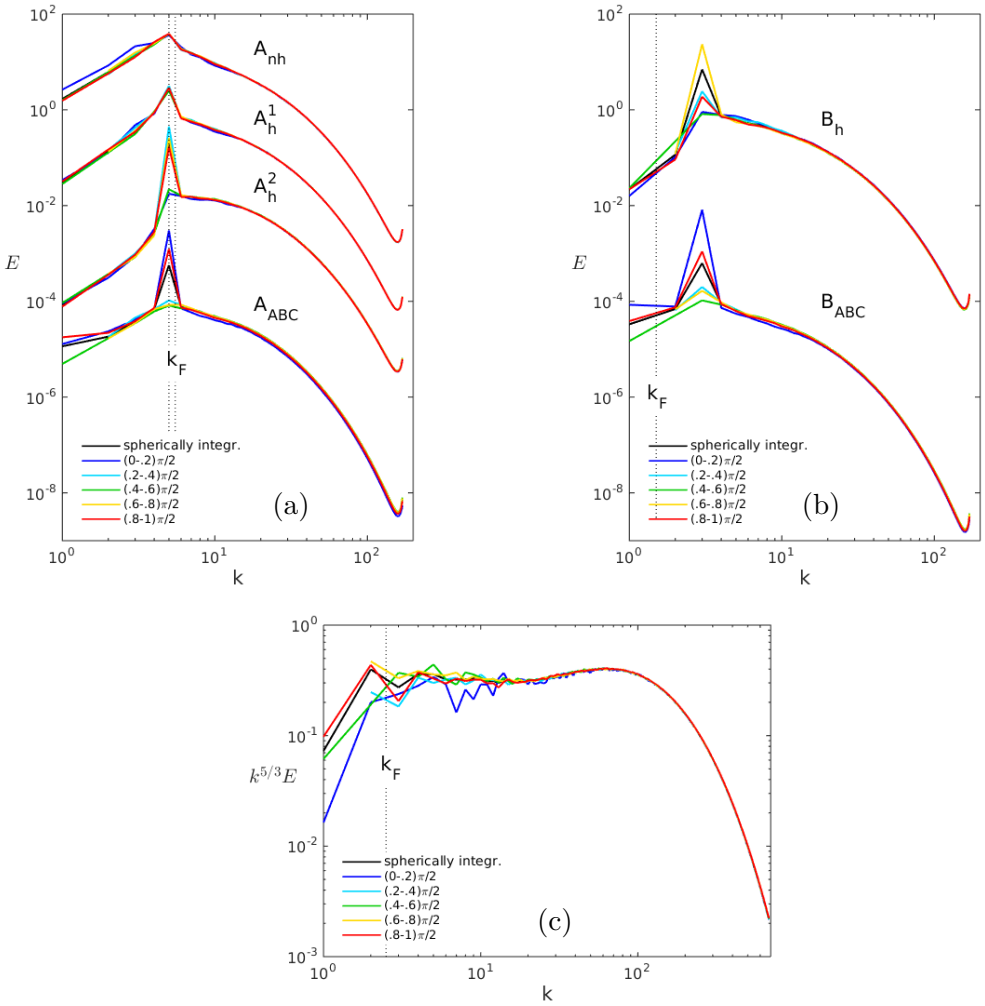

Figure 3.2: (a) Directional energy spectra $E_i(k)$ as functions of wavenumber k for the five angular sectors for set A ($k_F \simeq 5$); (b) Directional energy spectra $E_i(k)$ as functions of wavenumber k for the five angular sectors for set B ($k_F \simeq 3$); (c) Directional energy spectra $E_i(k)$ compensated by $k^{5/3}$ as functions of wavenumber k for the five angular sectors for run $\mathrm{D_{nv}}$. The five sectors are indicated in legend, and the same colorcode applies throughout the present chapter and Chapter 4.

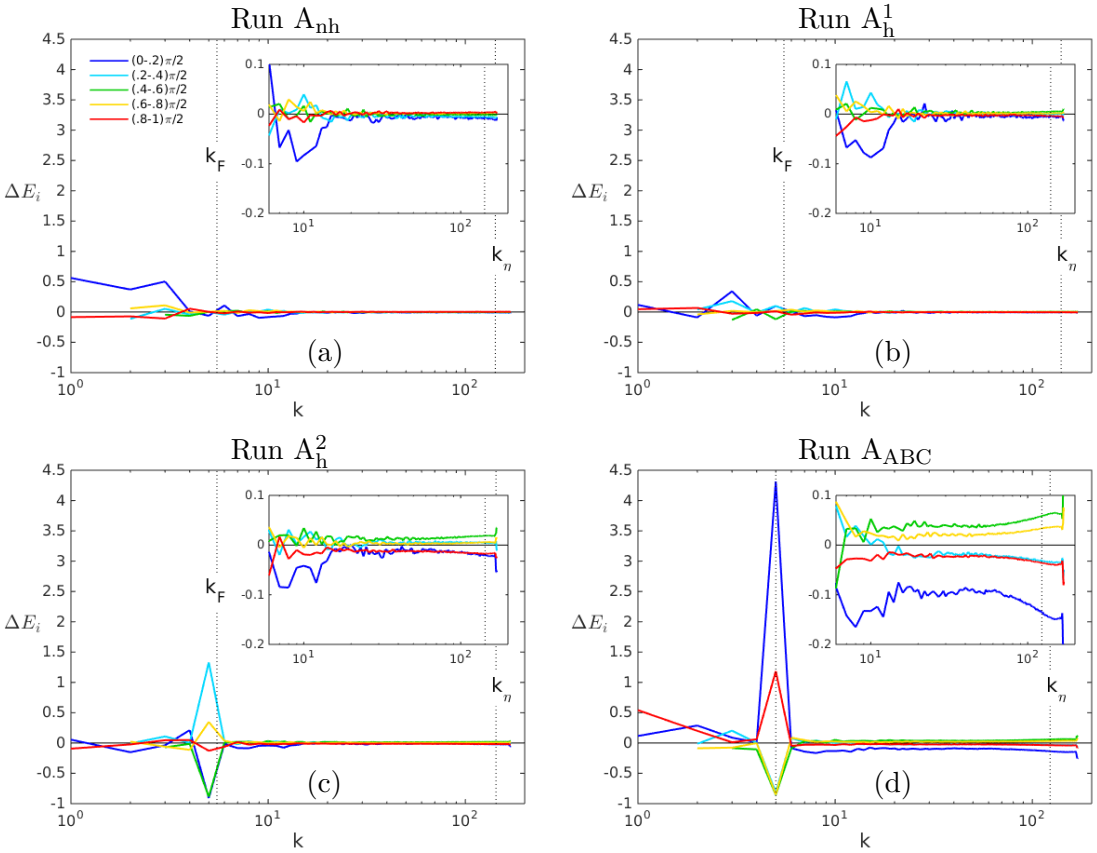

Figure 3.3: Directional anisotropy of the kinetic energy $\Delta E_i(k)$ for runs: (a) A_{nh}; (b) A_h^1; (c) A_h^2; (d) A_{ABC}. The insets focus on the large wavenumber inertial and dissipative ranges.

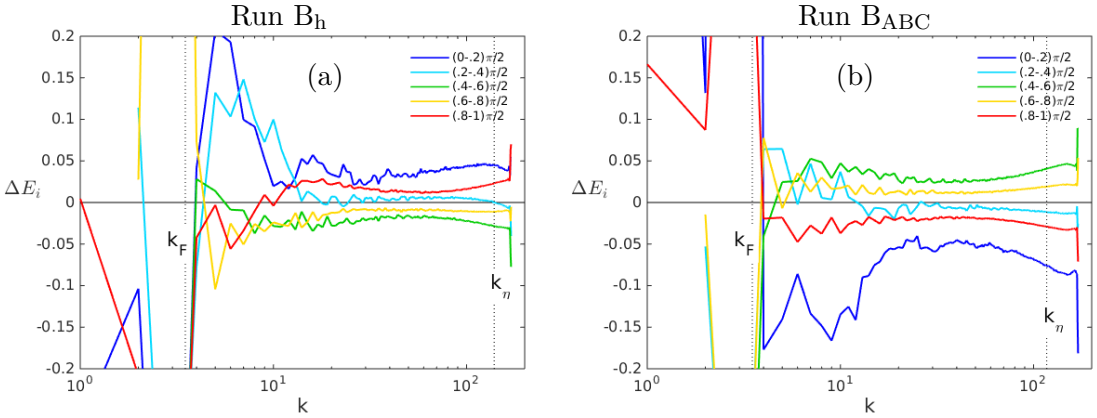

Figure 3.4: Directional anisotropy of the kinetic energy $\Delta E_i(k)$ for: (a) run B_h; (b) run B_{ABC}.

if the number of the largest wavenumbers is sufficiently small, a small number of modes hold most of the energy associated to the truncated Euler system and anisotropy develops. However, the number of largest wavenumbers does not increase monotonically with k_F, and a larger value of k_F may yield larger small-scale anisotropy than a smaller value of k_F. Figure 3.7 shows the number of largest forced wavenumbers in Euler-forced runs as a function of k_F. This also explains why the anisotropy level of run $\mathrm{B_h}$ (highly helical Euler forced, $k_F = 3.5$, 8 largest wavenumbers) is almost as large as that of run $\mathrm{B_{ABC}}$ (ABC forced, $k_F = 3$), as seen in Fig. 3.4. In addition, their anisotropies are opposite because they depend on the different orientations of wavenumbers corresponding to the most excited modes.

We also observe in *e.g.* Figs. 3.3(a) and 3.5(a)-(b), that non-helical Euler-forced simulations never develop strong directional anisotropy. In fact, even the lowest possible forcing wavenumber allowing non-linear interactions in the truncated system, $k_F = 1.5$, leads to 18 forcing modes, which have the same energy densities if the net helicity of the truncated Euler system is zero. Furthermore, the anisotropy level of a $k_F = 1.5$ helical Euler forced run cannot be as strong as that in run $\mathrm{B_h}$ ($k_F = 3.5$, 8 largest wavenumbers) or in runs $\mathrm{A_{ABC}}$ and $\mathrm{B_{ABC}}$ (ABC-forced, 6 forcing modes), because in the sphere of radius $k_F = 1.5$ there are 12 largest wavenumbers (the ones with two unitary components and one null component). This is confirmed by Figs. 3.5(c)-(d), that show the energy directional anisotropy in helical runs of set C.

We finally investigate the influence of the Reynolds number. Figure 3.5 shows the energy directional anisotropy for both the non-helical and helical runs in set C (Euler forced, $k_F = 1.5$, at moderate and high Reynolds numbers). The helical runs $\mathrm{C_h^1}$ and $\mathrm{C_h^2}$ (with relative helicity equal to about 0.2) are qualitatively similar to the non-helical runs $\mathrm{C_{nh}^1}$ and $\mathrm{C_{nh}^2}$. By comparing the moderate Reynolds number case in runs $\mathrm{C_{nh}^1}$ and $\mathrm{C_h^1}$ (Figs. 3.5a and 3.5c) with the higher Reynolds number case in runs $\mathrm{C_{nh}^2}$ and $\mathrm{C_h^2}$ (Figs. 3.5b and 3.5d), no obvious trend towards isotropy is observed at increasing wavenumber and Reynolds number. Instead, for the largest Reynolds number, anisotropy clearly increases with the wavenumber, in agreement with [13, 14, 84, 85]. The same behavior is observed in run $\mathrm{D_{nv}}$ at an even higher Reynolds number, as shown in Fig. 3.6 (note that the spectra plotted in this figure have been obtained by using larger bins than in the other cases, since no time-averaging is possible over this single velocity field snapshot).

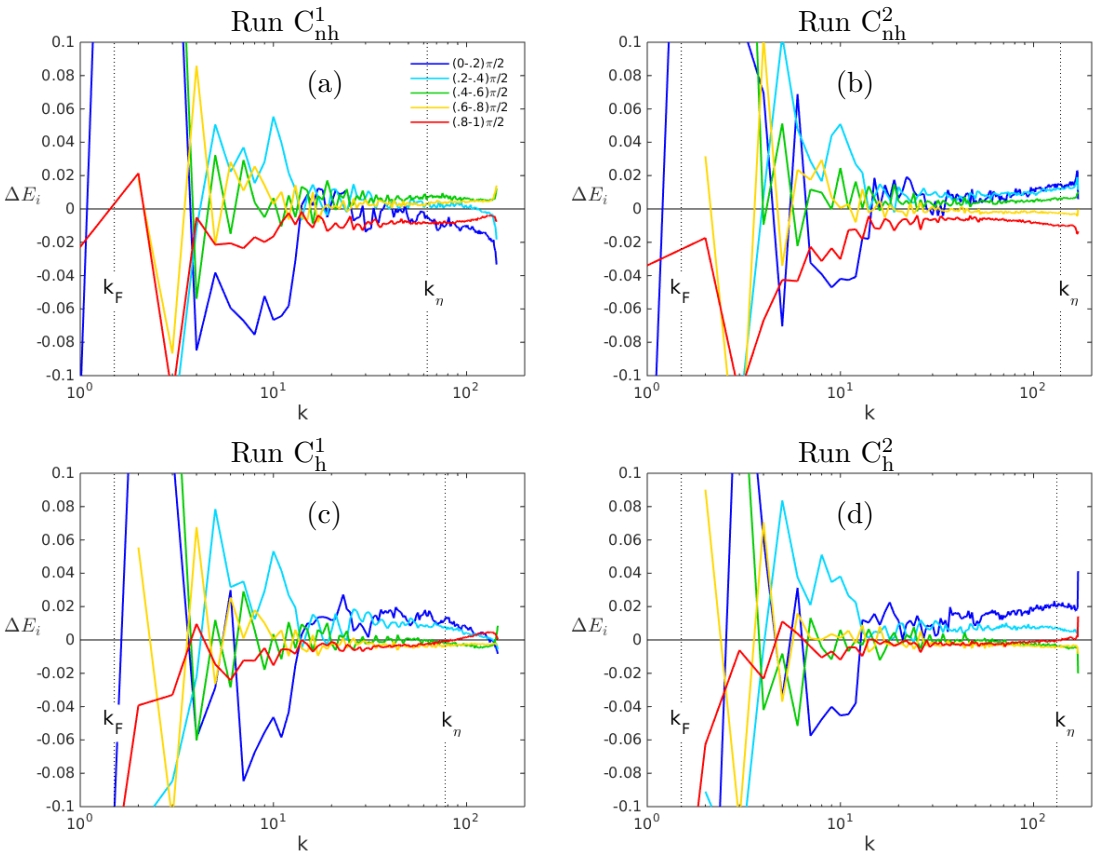

Figure 3.5: Directional anisotropy of kinetic energy $\Delta E_i(k)$ for: (a) run C^1_{nh}; (b) run C^2_{nh}; (c) run C^1_h; (d) run C^2_h. Left column: $Re^\lambda \approx 120$; right column: $Re^\lambda \approx 200$.

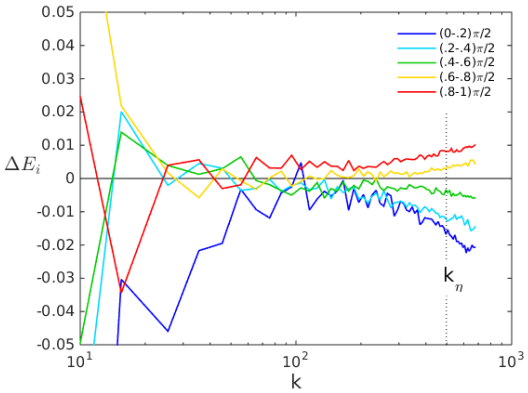

Figure 3.6: Directional anisotropy of kinetic energy $\Delta E_i(k)$ for run D_{nv}.

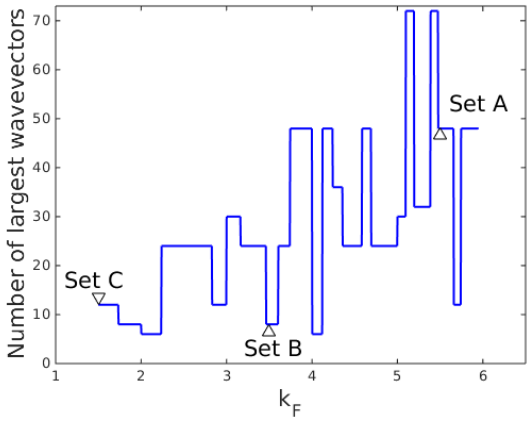

Figure 3.7: Number of largest forced wavevectors in Euler-forced runs as a function of the forcing wavenumber. Markers indicate the values of k_F for sets A, B and C.

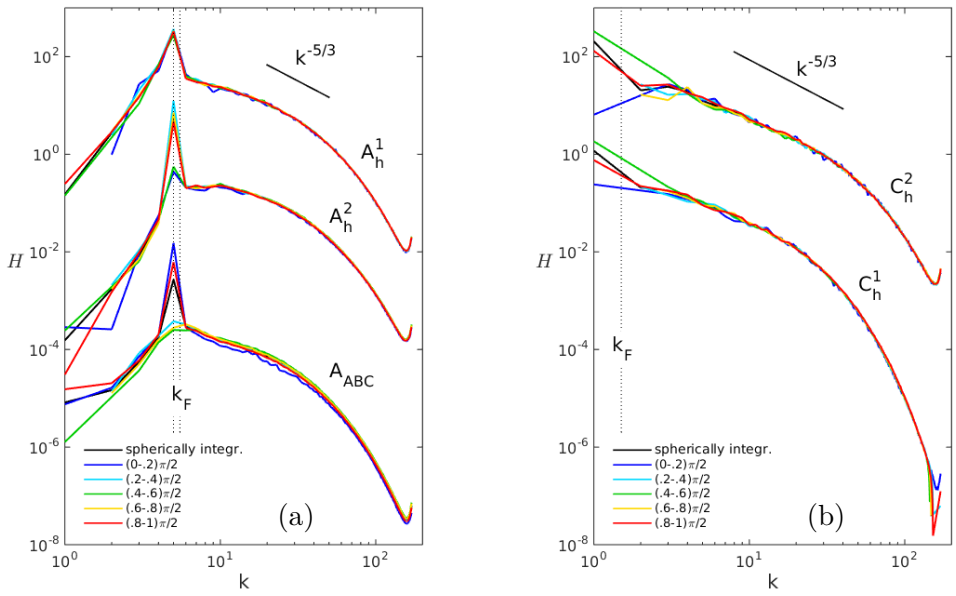

Figure 3.8: Directional helicity spectra $H_i(k)$ for: (a) runs A^1_h, A^2_h and A_ABC; (b) runs C^2_h and C^1_h.

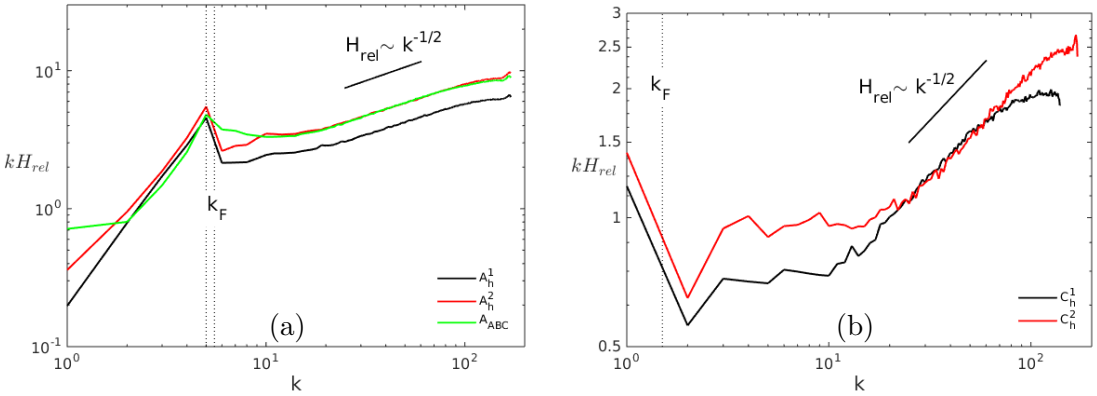

Figure 3.9: Relative helicity spectra $H(k)/(2kE(k))$ compensated by k for helical runs in: (a) set A; (b) set C.

3.4 Helicity spectra and helicity directional anisotropy

Figure 3.8 shows helicity directional spectra for helical runs in sets A and C. As in energy directional spectra, no small scale anisotropy can be detected from these helicity spectra, and large scales seem to be more anisotropic in the case of ABC forcing.

Figure 3.9 shows compensated relative helicity spectra $H(k)/(2kE(k))$ for helical runs in sets A and C. A slope close to -1 at low wavenumbers indicates that energy and helicity spectra scale with the same power of k at large scales. The observed small-scale $-1/2$ slope was reported in previous studies of both isotropic [51] and rotating [53] helical turbulence. The maximal value of relative helicity is approximately 1 and is obtained in the shells containing wavenumbers with modulus k_F for all five simulations.

As for the kinetic energy, we define the normalized departure of the directional helicity spectrum from the spherically-integrated one as $\Delta H_i(k) = (H_i(k) - H(k))/H(k)$. Figure 3.10 shows this for the helical runs in sets A and B. The distribution of directional anisotropy is similar between energy and helicity (compare Fig. 3.10(a-c) with Fig. 3.3(b-d), and Fig. 3.10(d,e) with Fig. 3.4(a,b)). Conclusions similar to those presented in section 3.3 can therefore be drawn for helicity, that is, the ABC-forced runs display a higher level of directional anisotropy with respect to Euler-forced runs, and helicity directional anisotropy increases with relative helicity in Euler-forced runs.

In summary, by looking at the results obtained for the most anisotropic forcings, that is Figs. 3.3(d), 3.4(b), 3.10(c), and 3.10(e), that represent energy and helicity directional anisotropy for the ABC-forced runs with $k_F = 5$ and $k_F = 3$, and Fig. 3.4(a) (directional anisotropy of

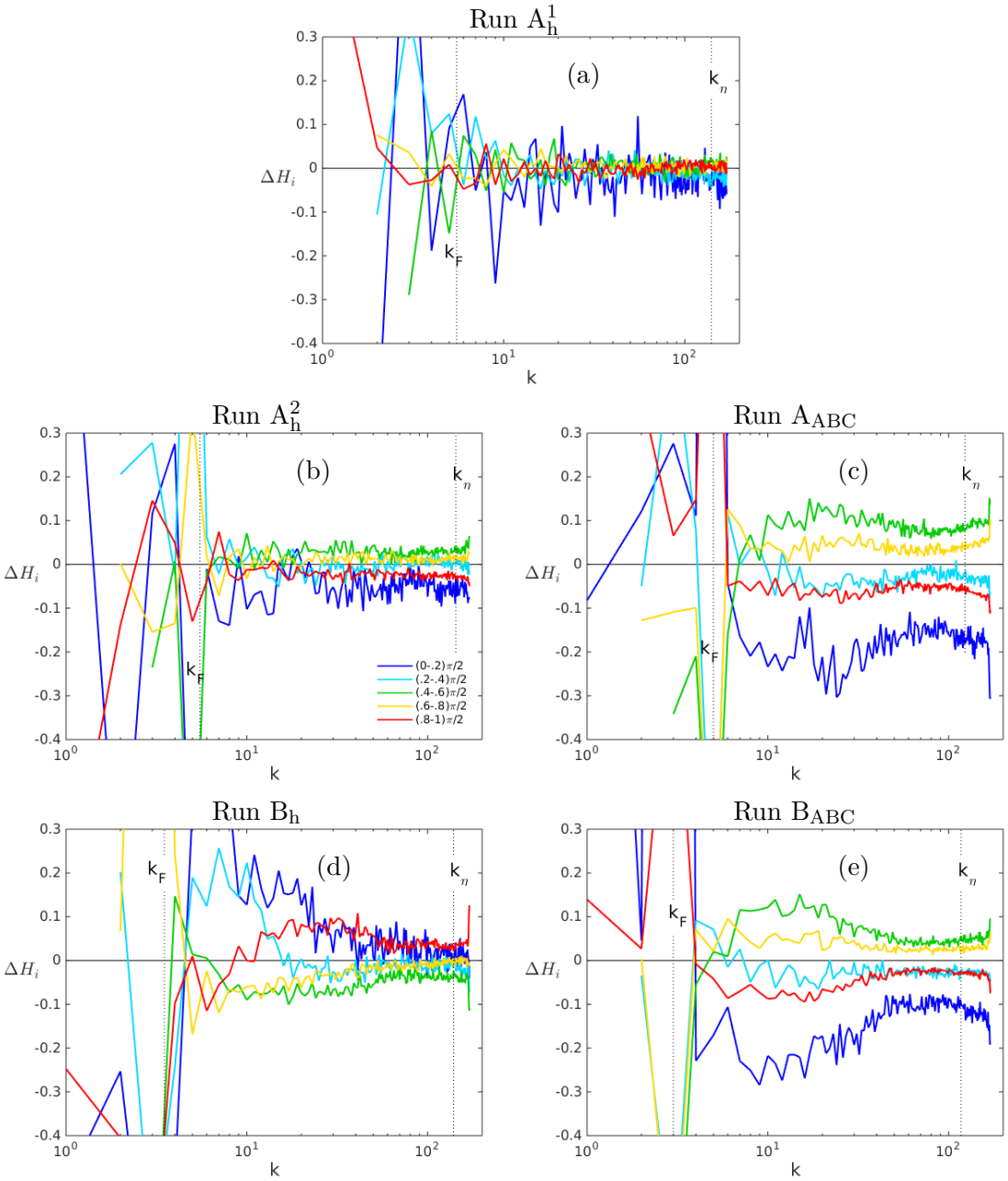

Figure 3.10: Helicity directional anisotropy $\Delta H_i(k,\theta)$ for: (a) run A_h^1; (b) run A_h^2; (c) run A_{ABC}; (d) run B_h; (e) run B_{ABC}.

the highly helical Euler-forced run with $k_F = 3.5$), it is clear that the anisotropy for each angular sector is constant down to the smallest resolved scales or that it even increases with the wavenumber. This is consistent with the results of Yeung & Brasseur [84, 85] for highly anisotropic forcings.

3.5 Polarization anisotropy

We focus now on the directional dependence of the polarization $z(\boldsymbol{k})$, which has been introduced in Chapter 1 (see also [17, 25, 27]) and which we compute numerically according to Eq. (2.6). In particular, we compute the normalized spectrum and the normalized directional spectra of its real part, respectively $\Re Z(k)/E(k) = (E^{\mathrm{pol}}(k) - E^{\mathrm{tor}}(k))/E(k)$ and $\Re Z_i(k)/E(k) = (E_i^{\mathrm{pol}}(k) - E_i^{\mathrm{tor}}(k))/E(k)$. We recall that we compute E^{pol} and E^{tor} as

$$E^{\mathrm{pol}}(k) = \sum_{\text{shell } k} \frac{1}{2}\langle u^{(2)*}(\boldsymbol{k}) u^{(2)}(\boldsymbol{k})\rangle \tag{3.1}$$

$$E^{\mathrm{tor}}(k) = \sum_{\text{shell } k} \frac{1}{2}\langle u^{(1)*}(\boldsymbol{k}) u^{(1)}(\boldsymbol{k})\rangle \tag{3.2}$$

where $u^{(1)}$ and $u^{(2)}$ are the components of $\hat{\boldsymbol{u}}$ in the Craya-Herring frame introduced in section 1.1.2. Also recall that $E^{\mathrm{pol}}(k) = E^{\mathrm{tor}}(k)$ in strictly isotropic turbulence.

The $\Re Z(k)/E(k)$ quantity is plotted in Fig. 3.11 for runs of set A. In the non-helical run (Fig. 3.11a), $\Re Z(k)$ displays the features expected in strictly isotropic turbulence (that is, its spherically integrated spectrum and its directional spectra vanish up to statistical uncertainty), both in the inertial and in the dissipative ranges. Runs $\mathrm{A}_{\mathrm{h}}^1$ (Fig. 3.11b) and $\mathrm{A}_{\mathrm{h}}^2$ (Fig. 3.11c) clearly show that, in Euler forced runs, the presence of helicity induces a slight polarization anisotropy over most of the inertial and dissipative ranges, and that isotropy is obtained only at the smallest scales. Larger values of the polarization anisotropy are found in the inertial range in the ABC-forced run (Fig. 3.11d) due to the relatively low number of excited modes. In this run, the polarization anisotropy level is definitely larger with respect to the highly helical Euler-forced run (Fig. 3.11c), although the relative helicity is the same in both runs.

Figure 3.12 displays the polarization anisotropy of runs in set B. The Euler-forced run B_{h} (Fig. 3.12a) now is only slightly less anisotropic than the ABC-forced run $\mathrm{B}_{\mathrm{ABC}}$ (Fig. 3.12b), confirming that the polarization anisotropy, similarly to the energy and helicity directional anisotropy, depends on the number of sufficiently excited modes.

In order to investigate the effect of an increase in the Reynolds number, we also plot the polarization anisotropy for runs in set C in Fig. 3.13. No difference is observed up to statistical

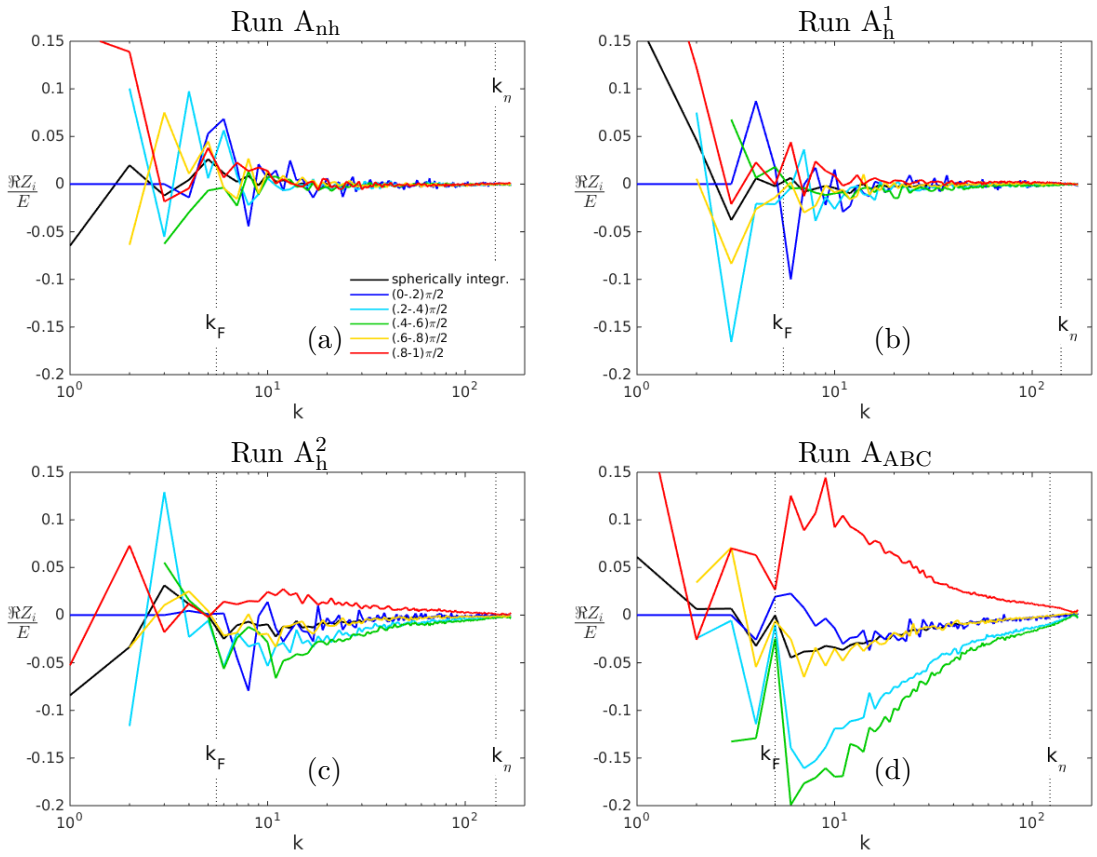

Figure 3.11: normalized directional polarization spectra $\Re Z_i(k)/E(k)$ for: (a) run A_{nh}; (b) run A_h^1; (c) run A_h^2; (d) run A_{ABC}.

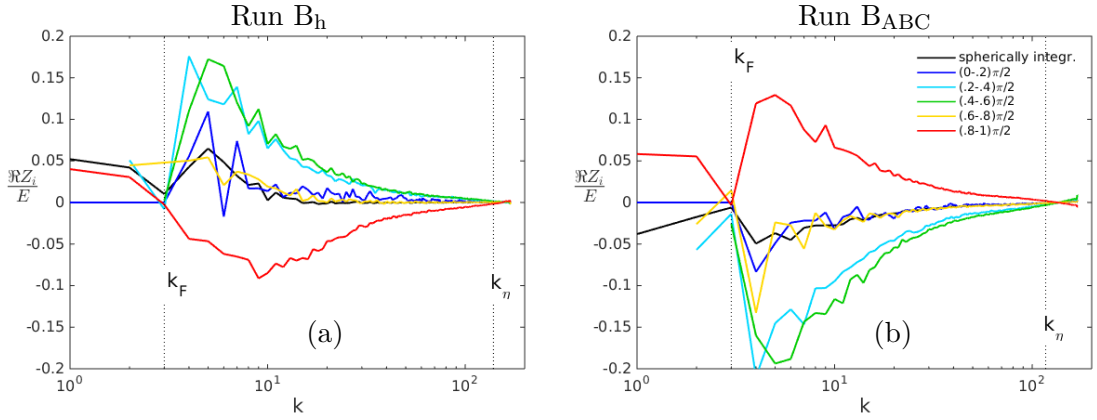

Figure 3.12: normalized directional polarization spectra $\Re Z_i(k)/E(k)$ for: (a) run B_h; (b) run B_{ABC}.

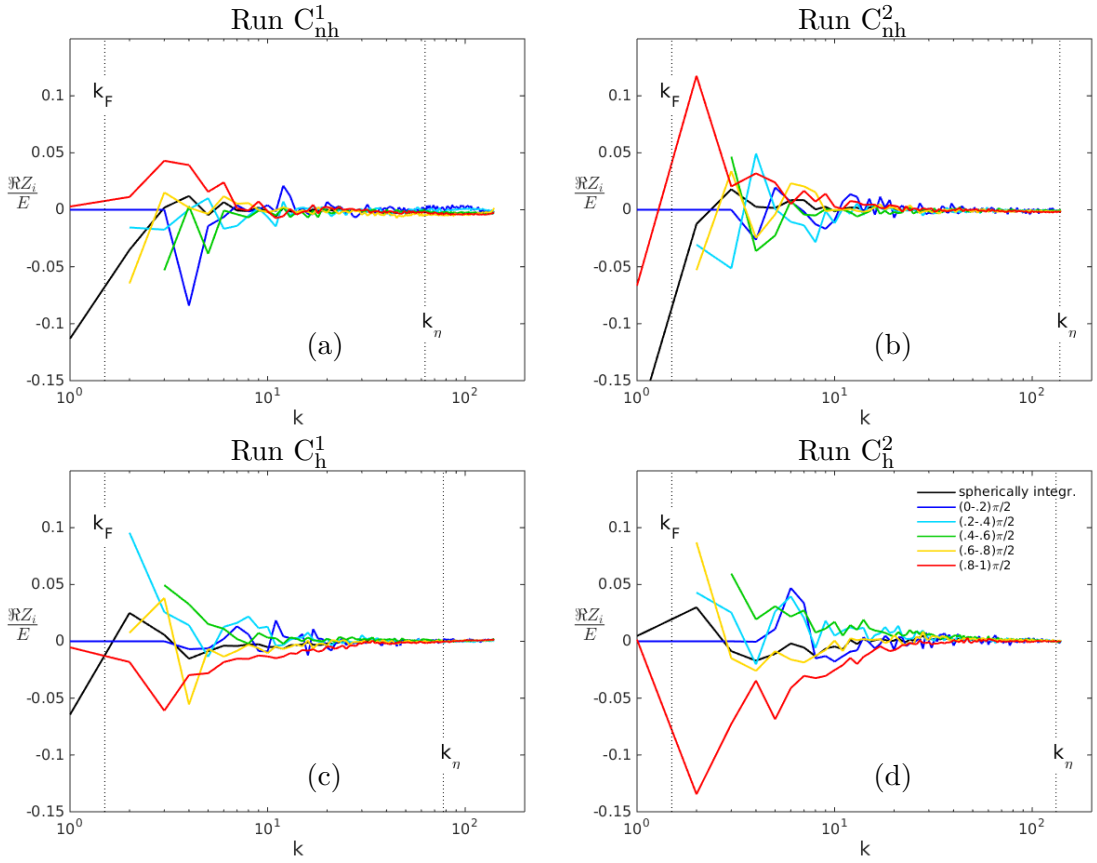

Figure 3.13: normalized directional polarization spectra $\Re Z_i(k)/E(k)$ for: (a) run C^1_{nh}; (b) run C^2_{nh}; (c) run C^1_h; (d) run C^2_h. Left column: $Re^\lambda \approx 120$; right column: $Re^\lambda \approx 200$.

uncertainty between the moderate Reynolds number runs C^1_{nh} and C^1_h (Figs. 3.13(a,c)) and the high Reynolds number runs C^2_{nh} and C^2_h (Figs. 3.13(b,d)), independently of the presence of helicity. A comparison between the non-helical runs C^1_{nh} and C^2_{nh} (Figs. 3.13(a,b)) and the helical runs C^1_h and C^2_h (Figs. 3.13(c,d)) confirms what has already been observed for set A (Fig. 3.11), *i.e.* the presence of helicity in Euler-forced runs increases the polarization anisotropy.

Chapter 4

Anisotropy induced by rotation

In this chapter, the direction- and scale-dependent anisotropy of rotating turbulence is studied. It is first shown that in the ABC-forced simulations the level of polarization anisotropy is similar to that obtained at lower Rossby number in Euler-forced runs and that the slope of the energy spectrum is altered. The first result is due both to the nature of the forcing itself and to the fact that it allows an inverse cascade to develop, while the second one depends only on the presence of the inverse cascade. Then, we show that, even at low rotation rate, the natural anisotropy induced by the Coriolis force is visible at all wavenumbers. We also identify two different wavenumber ranges in which anisotropy behaves differently, and show that the characteristic lenghscale separating them is the one at which rotation and dissipation effects balance, provided that the Rossby number is not too low. Finally, we analyze the distributions of the quantities appearing in the von Kármán-Howarth-Monin equation. We confirm the results already obtained through the spectral analysis: anisotropy is present at all scales and two different anisotropic ranges exist even in separation space. By contrasting our numerical data with experiments by P.-P. Cortet and F. Moisy [21] and with Galtier's inertial law [30], we show that the experiments fit our small scale range, while the large scale range is consistent with the inertial law.

4.1 Rotating turbulence simulations

In Chapter 3 we studied the anisotropy artificially induced by forcing. In the present chapter, we consider forced rotating homogeneous turbulence which we simulate numerically as in the previous chapter but setting $\mathbf{\Omega} \neq \mathbf{0}$ in the momentum equation (1.97). Anisotropy has now two contributions: one, artificial, due to the forcing, and another one inherent to the phenomenology of rotating flows *per se*. However—unlike in the non-rotating case—in the presence of background

Run	Forcing	k_F	$k_{\max}\eta$	k_η	k_Ω	Re^λ	Re^L	Ro^ω	Ro^L	$H_{\rm rel}$	Resolution
$\mathrm{R}^1_{\mathrm{nh}}$	non-hel.	5.5	1.21	140	43.4	111	373	1.26	0.206	-6.60E-3	512^3
$\mathrm{R}^2_{\mathrm{nh}}$	non-hel.	5.5	1.14	149	82.5	149	435	0.857	0.161	-2.70E-3	512^3
$\mathrm{R_h}$	helical	5.5	1.34	127	48.0	116	307	1.10	0.228	0.522	512^3
$\mathrm{R_{ABC}}$	ABC	5	2.42	70.2	25.7	111	351	1.13	0.195	0.591	512^3
$\mathrm{S}^1_{\mathrm{nh}}$	non-hel.	5.5	1.16	295	9.01	151	808	5.91	0.605	-2.85E-3	1024^3
$\mathrm{S}^2_{\mathrm{nh}}$	non-hel.	5.5	1.17	290	44.1	187	959	2.03	0.216	-5.27E-3	1024^3
$\mathrm{S_h}$	helical	5.5	1.29	264	47.5	193	797	1.81	0.240	0.386	1024^3

Table 4.1: Parameters used in the rotating turbulence simulations. $k_\Omega = \left((2\Omega)^3/\epsilon\right)^{1/2}$ is the Zeman wavenumber. Letters R and S refer to runs at resolutions 512^3 and 1024^3, respectively. The other definitions are the same as in Tab. 3.1.

rotation, the Euler and ABC forcing schemes *a priori* give rise to substantially different physical systems: in Euler-forced runs the modes in the spherically truncated system evolve independently of the others, whereas low wavevectors modes in ABC-forced runs are coupled with all the other modes. As a consequence, if the ABC forcing is employed and if rotation is large enough, energy is allowed to cascade backwards. This inverse cascade, previously observed in [72], manifests as an increase of the energy in the smallest wavenumbers, and the flow is not statistically stationary.

Table 4.1 reports the parameters of 512^3 (set R) and 1024^3 (set S) rotating runs forced through Euler and ABC schemes. Runs $\mathrm{R}^1_{\mathrm{nh}}$, $\mathrm{R_h}$ and $\mathrm{R_{ABC}}$ have comparable Reynolds and Rossby numbers, runs $\mathrm{R_h}$ and $\mathrm{R_{ABC}}$ also have comparable relative helicity, and run $\mathrm{R}^2_{\mathrm{nh}}$ has a Rossby number significantly lower than the other three runs. Thus, by comparing run $\mathrm{R_h}$ with run $\mathrm{R_{ABC}}$ one can estimate the differences of anisotropy between ABC-forced runs, with a dual (direct and inverse) cascade, and helical Euler-forced runs, with only forward cascade. The comparison of runs $\mathrm{R}^1_{\mathrm{nh}}$ and $\mathrm{R_h}$ allows to study the effect of helicity, and comparing run $\mathrm{R}^1_{\mathrm{nh}}$ with run $\mathrm{R}^2_{\mathrm{nh}}$ allows to study the effect of a decrease in the Rossby number. High resolution Euler-forced runs of set S have larger scale separation than runs in set R, and are used to study the small-scale anisotropy that naturally arises because of background rotation in the absence of inverse cascade.

Both the rotation rate vector and the fixed direction $\boldsymbol{n}$ defining the Craya frame are in the x_3 direction. In all Euler-forced runs presented in Tab. 4.1, the spherically truncated Euler equation

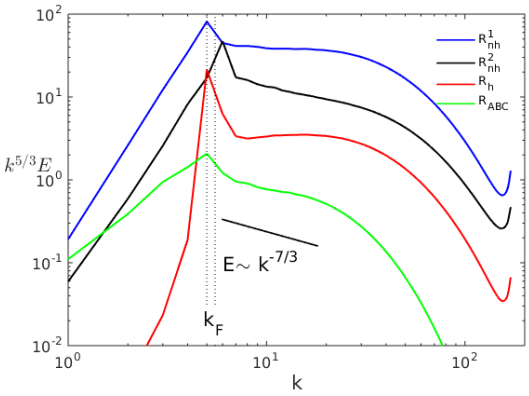

Figure 4.1: Spherically averaged energy spectra $E(k)$ compensated by $k^{5/3}$, for runs in set R.

includes the Coriolis force. We also performed runs without rotation in the Euler system and observed no significant change in the small-scale anisotropy.

4.2 Effects of forcing anisotropy and inverse cascade

Figures 4.1, 4.2 and 4.3 show the spherically averaged energy spectra, energy directional spectra and energy directional anisotropy for runs in set R.

In runs $\mathrm{R}^1_{\mathrm{nh}}$ (moderate Rossby number, non-helical Euler forced) and R_{h} (moderate Rossby number, helical Euler forced) the slope of the energy spectrum is close to $-5/3$. Since the Reynolds number is not very large, this is a consequence of weak rotation, as argued and observed in DNS by [6]. However run $\mathrm{R}_{\mathrm{ABC}}$ (moderate Rossby number ABC-forced), which has Reynolds and Rossby numbers values comparable to those of the Euler forced runs $\mathrm{R}^1_{\mathrm{nh}}$ and R_{h}, shows a steeper spectrum (about $-7/3$ slope), close to the one of run $\mathrm{R}^2_{\mathrm{nh}}$ (low Rossby number, non-helical Euler-forced). Note that a slope equal to -2.2 was already observed in [52, 53] for rotating DNS forced through the ABC forcing.

Figure 4.2 shows the direction-dependent kinetic energy spectra for the same runs. From this energetic point of view, wavevectors closer to the horizontal plane $\boldsymbol{k} \cdot \boldsymbol{\Omega} = 0$ (red curves) hold more energy than wavevectors closer to $\boldsymbol{\Omega}$ (blue curves), thereby indicating a trend towards two-dimensionalisation as expected in the presence of rotation. Directional anisotropy is larger at large scales than at small scales, as shown by the departure between the less energetic vertical orientation ($\theta \simeq 0$) spectrum and the more energetic horizontal orientation ($\theta \simeq \pi/2$) spectrum. However, the small scales are still significantly anisotropic. In fact, for runs in set R, the Zeman wavenumber k_Ω is relatively large ($1.8 \leq k_\eta/k_\Omega \leq 3.2$). Observing anisotropy at all scales is

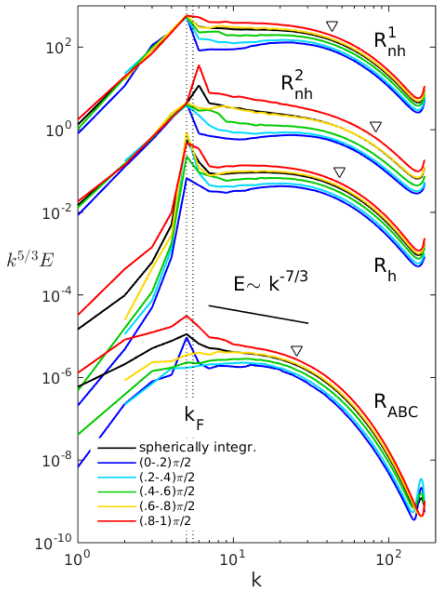

Figure 4.2: Directional energy spectra $E_i(k)$, compensated by $k^{5/3}$ for runs in set R. Markers indicate the Zeman scale $k_\Omega = \sqrt{(2\Omega)^3/\epsilon}$.

therefore consistent with the classical dimensional argument according to which isotropy should be obtained only at scales significantly smaller than the Zeman scale [25, 53, 88].

Considering only the relative anisotropy in the energy spectrum, we compute the scale-normalized departure between each directional spectrum and the corresponding average spectrum, $\Delta E_i(k) = (E_i(k) - E(k))/E(k)$. Figure 4.3 shows this quantity for the four runs of set R. It confirms that the relative anisotropy persists through the inertial scales down to the smallest ones, and that the difference between $E_1(k)$ and $E_5(k)$ for the strongly rotating non-helical Euler-forced flow (run $R^2_{\rm nh}$, Fig. 4.3(b)), is significantly larger than that for the other runs. The energy directional anisotropy inherently induced by the ABC forcing and evidenced in Chapter 3 is partly concealed in the anisotropy due to large rotation, as observed when comparing Figs. 4.3(c) (helical Euler forced) and 4.3(d) (ABC forced). The effect of helicity can be deduced by comparing Figs. 4.3(a) and 4.3(c), which shows that the presence of helicity has no significant effect on the energy spectrum small-scale anisotropy. Note finally that the presence of the inverse cascade has no clear effect on small-scale energy directional anisotropy (compare Figs. 4.3c and d).

The third quantity, plotted in Fig. 4.4 for runs in set R, is the directional anisotropy of the real part of polarization normalized by the energy spectrum, $\Re Z(k)/E(k) = \left(E^{\rm pol}(k) - E^{\rm tor}(k)\right)/E(k)$. When rotation is strong enough, wavevectors close

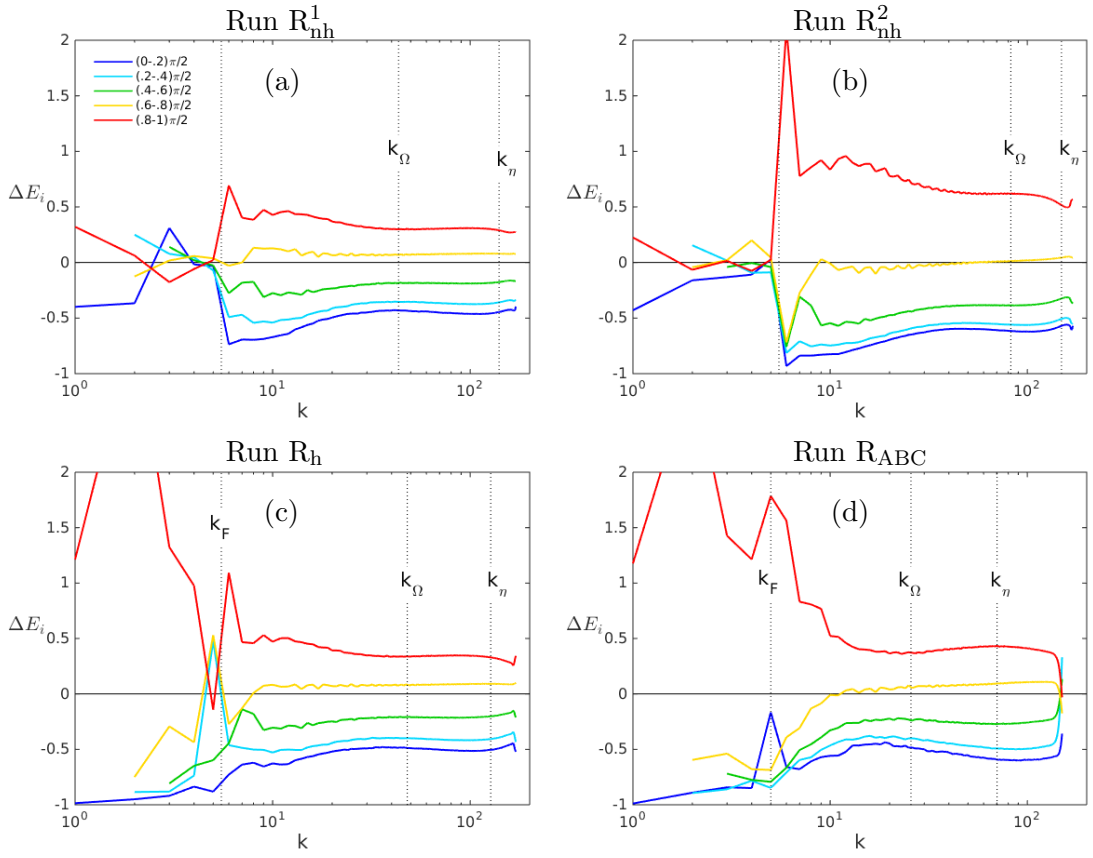

Figure 4.3: Relative directional anisotropy of kinetic energy $\Delta E_i(k) = (E_i(k) - E(k))/E(k)$ for: (a) run R^1_{nh}; (b) run R^2_{nh}; (c) run R_h; (d) run R_{ABC}.

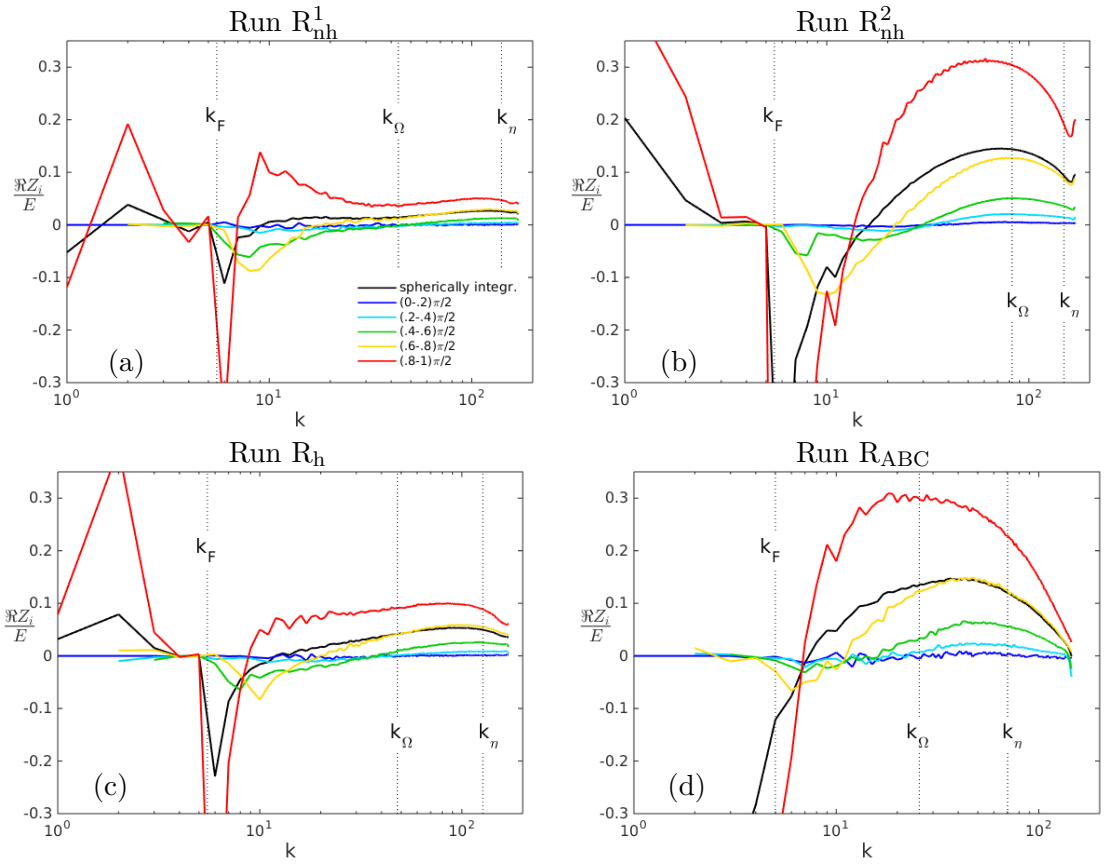

Figure 4.4: Real part of polarization normalized by the energy spectrum $\Re Z(k)/E(k) = \left(E^{\mathrm{pol}}(k) - E^{\mathrm{tor}}(k)\right)/E(k)$ for: (a) run $\mathrm{R}^1_{\mathrm{nh}}$; (b) run $\mathrm{R}^2_{\mathrm{nh}}$; (c) run R_{h}; (d) run $\mathrm{R}_{\mathrm{ABC}}$.

to the horizontal plane hold much more energy than wavevectors close to $\mathbf{\Omega}$ and $\Re Z(k)$ provides information on the structure of turbulence at the considered scale. This concentration of energy is observed for runs in set R in Fig. 4.3. Fig. 4.4 shows that, for all the runs, the real part of the spherically averaged polarization is negative at small wavenumbers (close to k_F), and positive at larger wavenumbers, which indicates that at large scales the toroidal energy is greater than the poloidal one, while at small scales the opposite happens. This is related to the presence of large scale "vortical" structures and of small scale "jetal" structures [25]. Upon comparing Figs. 4.4(a) and (b), one sees that increasing rotation increases the normalized polarization anisotropy, which is largest in the equatorial plane and vanishes in the axial direction, with a monotonous dependence in between.

In run $\mathrm{R}^2_{\mathrm{nh}}$ (non-helical high-rotation Euler-forced, Fig. 4.4b), the real part of polarization reaches a maximum before decreasing towards the smallest dissipative scales, although not reaching isotropy at the largest resolved wavenumber $k_{\max}$. In comparison, the slower rotating case (run $\mathrm{R}^1_{\mathrm{nh}}$) presented in Fig. 4.4(a) maintains moderate polarization anisotropy down to the smallest scales, a behaviour similar to that of the helical case ($\mathrm{R_h}$) of Fig. 4.4(c), even though the presence of helicity clearly increases small-scale polarization anisotropy (compare Figs. 4.4a and 4.4c). Run $\mathrm{R_{ABC}}$ (moderate rotation ABC-forced, Fig. 4.4d), shows a polarization anisotropy level similar to that of run $\mathrm{R}^2_{\mathrm{nh}}$.

Therefore, although the relative helicity and the Reynolds and Rossby numbers of the ABC-forced run $\mathrm{R_{ABC}}$ (Fig. 4.4d) are similar to those of run R_{h} (Fig. 4.4c), the polarization anisotropy of the former is much higher than that of the latter. The level of this anisotropy for run $\mathrm{R_{ABC}}$ is comparable to that obtained with a stronger rotation in Euler-forced runs (Fig. 4.4(b)).

At this point, one may wonder if the differences observed between ABC-forced and Euler-forced simulations depend mainly on the intrinsic anisotropy of the ABC force or on the presence of an inverse cascade. In order to answer this, we also performed a helical shell-Euler-forced rotating run, in which the truncated system includes only modes corresponding to wavenumbers k such that $4.6 \leq k \leq 5.4$, as explained in section 2.3.3. Figure 4.5(a) shows the corresponding energy directional spectra and spherically-integrated spectrum, the slope of the latter is clearly stronger than $-5/3$ (we observe approximately $k^{-8/3}$ for this run). Therefore, while an inverse cascade does not affect substantially energy directional anisotropy, the reason for a steeper energy spectrum slope in ABC forced runs is just the presence of an inverse cascade, absent in standard Euler-forced runs (forced for $k < k_F$). The polarization anisotropy for the shell-Euler-forced run, shown in Fig. 4.5(b), is larger than that of the equivalent Euler-forced run without

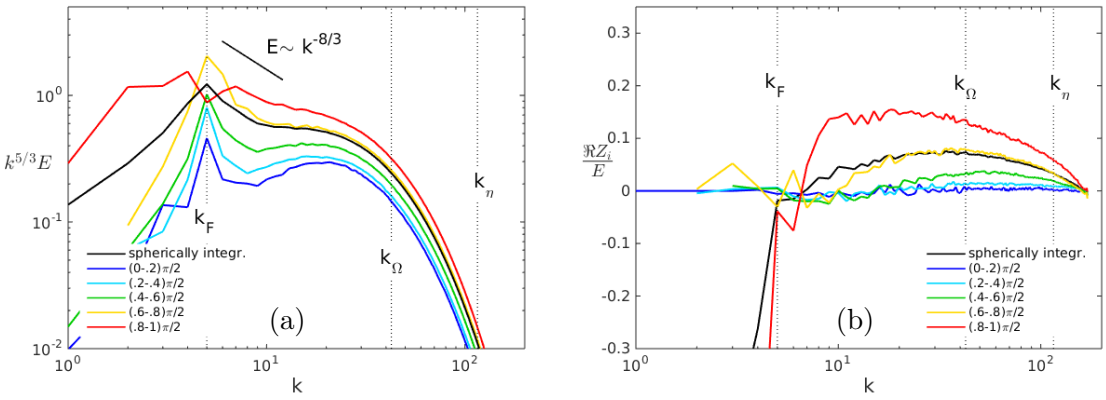

Figure 4.5: Helical shell-Euler forced run: the truncated system includes wavenumbers such that $4.6 \leq k \leq 5.4$ and does not include the Coriolis force. The parameters of the simulation are $Re^{\lambda} = 180$, $Ro^{\omega} = 1.13$, $H_{\mathrm{rel}} = 0.50$. (a) Directional energy spectra compensated by $k^{5/3}$; (b) real part of polarization normalized by the energy spectrum.

inverse cascade (Fig. 4.4c), but smaller than the ABC-forced run (Fig. 4.4d). The increased polarization anisotropy in ABC-forced rotating runs therefore seems to be induced both by the intrinsic anisotropy of the ABC forcing and by the presence of an inverse cascade.

Of course in a forced simulation with inverse cascade, energy increases with time at large scales, and therefore at some time the integral lengthscale L is too large with respect to the box size and confinement effects cannot be neglected any longer. For the shell-Euler run and run $\mathrm{R_{ABC}}$—and in the considered time interval—L is about 20% of the box size, slightly larger than the threshold value (10%) indicated in [50, 77]. However, in this section we analyzed statistics in the inertial and dissipative ranges, and therefore the related results are only negligibly sensitive to confinement [50].

4.3 Effect of rotation in higher Reynolds number cases

In this section we study the anisotropy that naturally arises in the presence of background rotation through 1024^3 resolution simulations, *i.e.* considering runs in set S that have larger Reynolds numbers than those of set R (see Tab. 4.1). Run $\mathrm{S^1_{nh}}$ also has smaller Zeman wavenumber, and thus allows to study the anisotropic features of scales much smaller than the Zeman scale.

The directional energy spectra for runs of set S are plotted in Fig. 4.6. A wide inertial range is observed, with a slope close to $-5/3$ for runs $\mathrm{S^1_{nh}}$ and $\mathrm{S_h}$ due to weak rotation. At first glance,

in the lowest rotation case (run S^1_{nh}) directional spectra collapse on the spherically integrated spectrum and small scales seem to return to directional isotropy.

Fig. 4.7 shows the relative directional energy anisotropy for runs in set S. A comparison between run S_h and run S^2_{nh} confirms that the presence of helicity has no substantial effect on the energy directional anisotropy, as already observed for runs in set R. Surprisingly, this figure shows that, notwithstanding the large scale separation ($5.6 \leq k_\eta/k_\Omega \leq 32.7$) with respect to set R, the relative anisotropy stays roughly constant down to the smallest scales, after decreasing over the upper inertial spectral subrange. Even in the largest Rossby number case, run S^1_{nh} (Fig. 4.7a), the amplitude of the relative energy departure at small scales is still significant and much larger than the anisotropy induced by forcing in the absence of rotation (compare Fig. 4.7a with Fig. 3.3a).

A second important observation is that there seems to be two subranges in the inertial spectral range over which anisotropy behaves differently. In the first one (smallest wavenumbers), the relative anisotropy for all sectors decreases with wavenumber. Then, for wavenumbers greater than an intermediate value, the relative anisotropy remains roughly constant. The separating wavenumber is clearly larger than k_Ω for run S^1_{nh} (large Rossby number) and is close to k_Ω for the other runs, S^2_{nh} and S_h, which have moderate Rossby numbers. Therefore, it is not clear how the separating scale between these two anisotropic ranges depends on the Zeman wavenumber. We will provide the answer to this question in section 4.4.

Finally, we present helicity directional spectra and directional anisotropy in Figs. 4.8(a) and (b), respectively. These figures show that helicity directional isotropy (which does not imply strict isotropy) is reached at some intermediate wavenumber, but that it disappears for larger wavenumbers. Similarly to energy, at small scales, sectors closer to the horizontal plane hold more helicity. Figure 4.8(c) also displays the relative helicity spectrum of every sector, $H_{\mathrm{rel}i}(k) = H_i(k)/\left(2kE_i(k)\right)$. From the viewpoint of relative helicity, no directional isotropy is obtained, and—no matter the scale—sectors closer to the horizontal plane hold lower relative helicity. Therefore, even if both energy and helicity are concentrated in more horizontal wavevectors, the relative contents of helicity is larger for the less energetic and more vertical wavevectors.

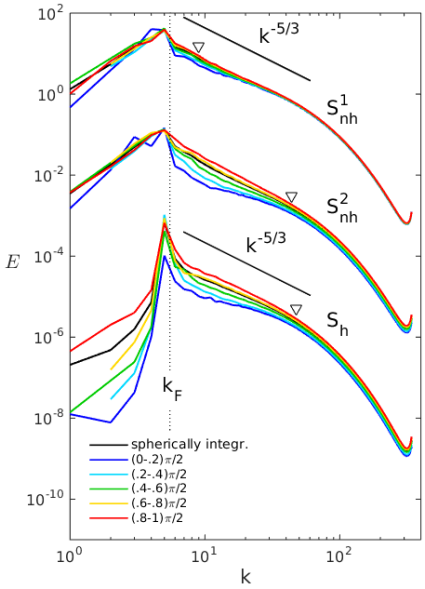

Figure 4.6: Directional energy spectra $E_i(k)$ for runs in set S. Markers indicate the Zeman scale $k_\Omega = \sqrt{(2\Omega)^3/\epsilon}$.

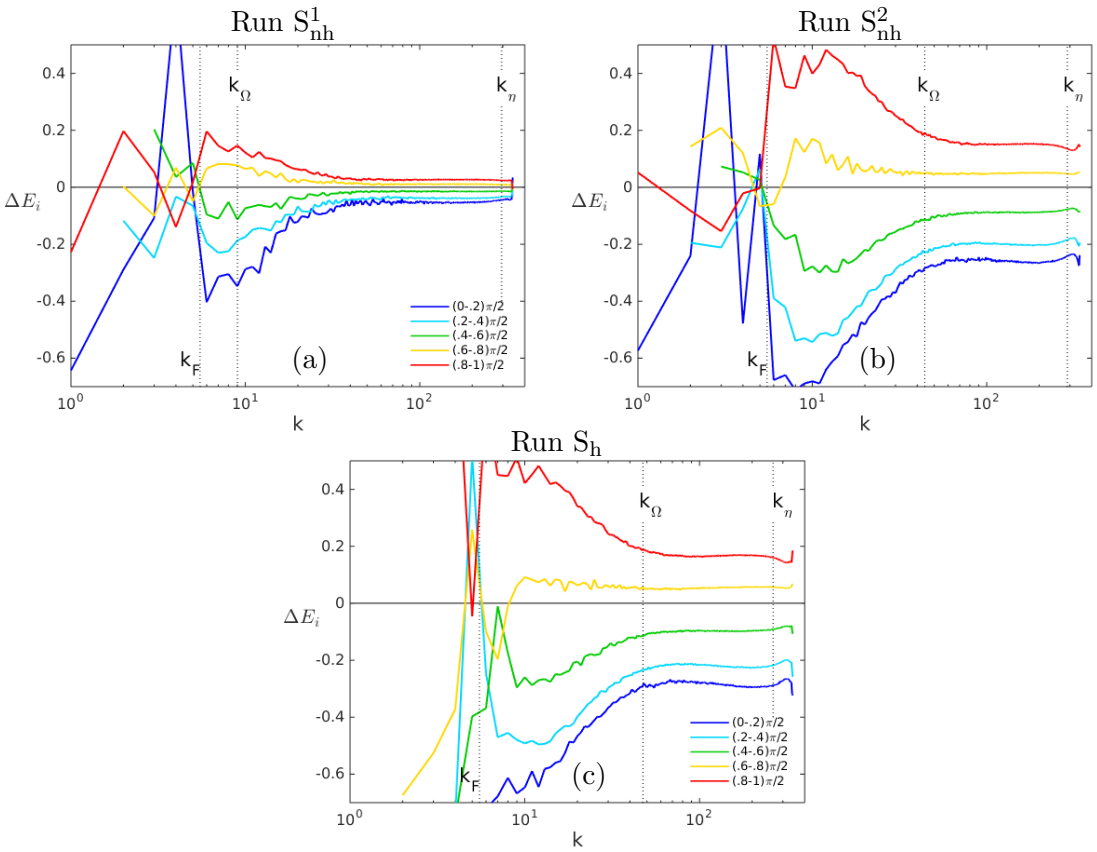

Figure 4.7: Energy directional anisotropy $\Delta E_i(k)$ for: (a) run $\mathrm{S}^1_{\mathrm{nh}}$; (b) run $\mathrm{S}^2_{\mathrm{nh}}$; (c) run S_{h}.

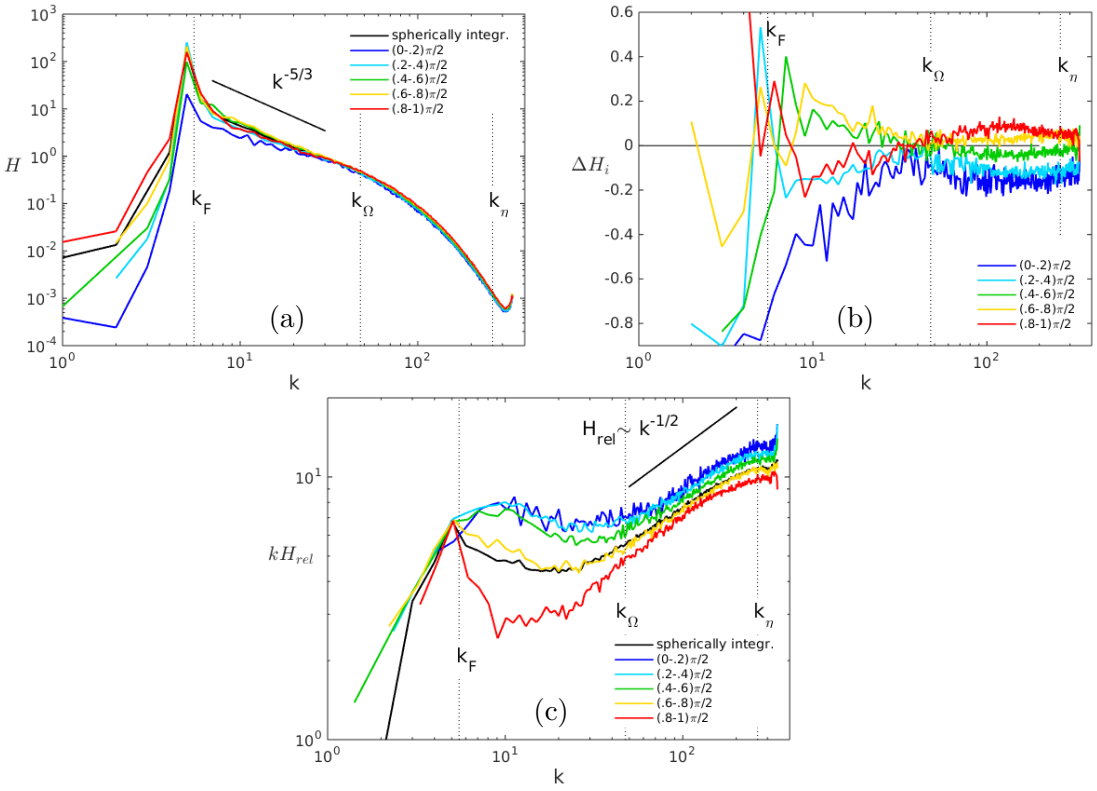

Figure 4.8: (a) Directional helicity spectra $H_i(k)$, (b) helicity directional anisotropy $\Delta H_i(k)$, (c) relative helicity directional spectra $H_{\mathrm{rel}i}(k) = H_i(k)/\left(2kE_i(k)\right)$, for run $\mathrm{S_h}$.

4.4 Threshold wavenumber

Recall from Chapter 1 that if the kinematic viscosity ν tends to zero (and the Reynolds number tends to infinity), both η and $r_{\Omega d}$ tend to zero. If the integral scale tends to infinity, the only relevant characteristic lengthscale is then the Zeman scale r_Ω, which is the scale at which the characteristic rotation time equals the characteristic inertia time. For this reason, according to classical dimensional arguments [25, 53, 88], in the asymptotically inviscid limit, scales much larger than r_Ω should be strongly affected by rotation and should therefore be more anisotropic, while scales much smaller than r_Ω are expected to be dominated by the nonlinear dynamics and to have isotropic properties.

However, only finite Reynolds number turbulence can be tackled through simulations and experiments, and very large Reynolds numbers are needed to achieve a good scale separation. DNS by [25, 53] seem to confirm return to isotropy at small scales, while in experiments by [46] the anisotropy is found to be stronger at small scales. In particular, in the forced rotating simulation of [53] isotropization seems to occur at a precise wavenumber (close to k_Ω). In [25], in which decaying rotating turbulence is investigated, isotropy is obtained only if rotation is weak enough, and a link between k_Ω and the wavenumber corresponding to maximum anisotropy is observed. Therefore, both the anisotropic character of small scales and the role of the Zeman scale are not fully understood.

In section 4.3, our analysis—that uses normalized indicators and includes simulations with large Rossby numbers—shows no return to isotropy, in contrast with previous numerical results [25, 53] but in agreement with experiments [46]. Nevertheless, even if isotropy is not obtained at small scales in our simulations, two different anisotropic ranges with qualitatively different anisotropic features can be identified (see *e.g.* Figs. 4.6 and 4.7). The low-wavenumber range shows large anisotropy decreasing with wavenumber, while the anisotropy level at larger wavenumbers is significantly lower, although not zero. Then, one may wonder if the threshold wavenumber between these two ranges has a specific physical interpretation. In order to answer this question, we analyze a larger number of Euler-forced runs (17 runs with 512^3 resolution and 6 runs with 1024^3 resolution), with Ro^ω ranging from 0.69 to 9.6, Re^λ ranging from 73.9 to 414, and scale separation r_Ω/η ranging from 1.3 to 68. Note that this set also includes runs with different forcing scales ($k_F = 1.5$ and 5.5), different relative helicity (ranging from 0 to 0.84), and runs that include or not the Coriolis force in the spherically truncated system.

First, we define a systematic method to compute the threshold wavenumber k_T, separating small-wavenumber (large anisotropy) and large-wavenumber (low anisotropy) ranges. Then, we

investigate its dependence on the other parameters of the flow and look for a physical interpretation of k_T.

Since for every run five energy directional-anisotropy indicators $\Delta E_i(k)$ are available, we first reduce them to a single indicator $a(k)$. In particular, we normalize every $\Delta E_i(k)$ by its mean value over the range $k > k_F$, and then average them:

$$a(k) = \frac{1}{5}\sum_{i=1}^{5} \frac{\Delta E_i(k)}{\overline{\Delta E_i}}. \tag{4.1}$$

Figure 4.9 shows the anisotropy indicator $a(k)$ corresponding to run $\mathrm{S}^2_{\mathrm{nh}}$ (Fig. 4.7b). In all rotating runs we found that $a(k)$ quickly decreases with wavenumber at large scales, reaches a minimum and then slowly increases with wavenumber up to the dissipative scales. Therefore, we compute k_T as the wavenumber corresponding to the minimum of $a(k)$, after smoothing.

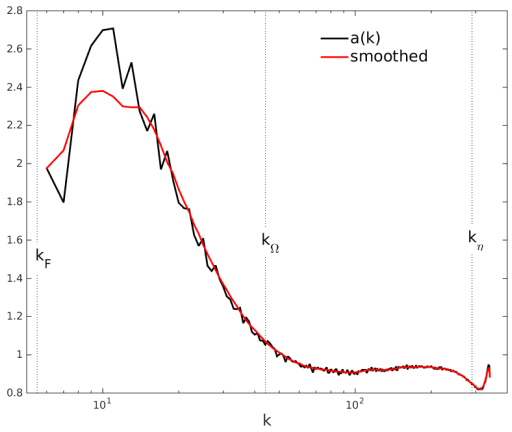

Figure 4.9: Anisotropy indicator (defined by Eq. (4.1)) for run $\mathrm{S}^2_{\mathrm{nh}}$.

As a first attempt, it is natural to investigate the dependence of k_T on the Zeman wavenumber k_Ω, with the purpose of checking the existence of a range in which $k_T \sim k_\Omega$. In Fig. 4.10(a), k_T/k_η is plotted as a function of k_Ω/k_η. For $k_\Omega/k_\eta \lesssim 1/4$ (weak or moderate rotation), k_T/k_η clearly increases with k_Ω/k_η, with a power law of exponent 1/3. For larger values of k_Ω/k_η, markers are more scattered, and no clear trend is observed. One possible explanation for the existence of these two regimes is that, if rotation is too strong (or equivalently k_Ω/k_η is too large), the threshold wavenumber k_T is located in the dissipative range, whereas in the opposite case it is in the inertial range. These two ranges are phenomenologically different, and different laws can be expected in the two cases. The rest of our discussion will be performed in the regime $k_\Omega/k_\eta \lesssim 1/4$, in which $k_T/k_\eta \sim (k_\Omega/k_\eta)^{1/3}$. This amounts to discarding the lowest Rossby number runs.

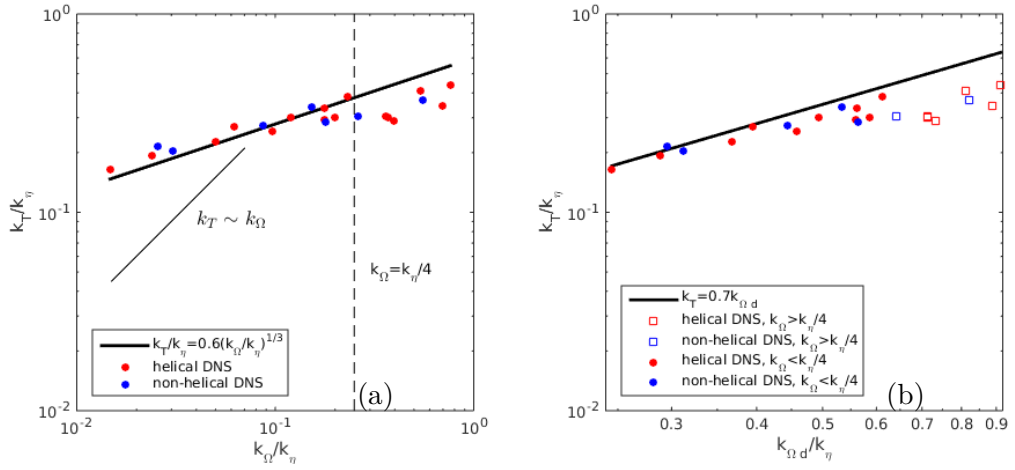

Figure 4.10: k_T/k_η plotted as a function of (a) k_Ω/k_η, (b) $k_{\Omega d}/k_\eta$. For comparison, the slope corresponding to $k_T \sim k_\Omega$ is shown too.

In short, Fig. 4.10(a) shows two important results: first, depending on the closeness of k_Ω to k_η two subranges with different behaviours are observed and second, in the low k_Ω range, k_T scales as $k_\Omega^{1/3} k_\eta^{2/3}$. In this regime, k_T is therefore not proportional to k_Ω, and depends on the dissipative scale as well. Recalling from Chapter 1 that, from the definitions of $k_{\Omega d}$, k_Ω and k_η, $k_{\Omega d} = k_\Omega^{1/3} k_\eta^{2/3}$, this means that k_T scales as $k_{\Omega d}$. This result is confirmed by Fig. 4.10(b), which furthermore shows that the factor between k_T and $k_{\Omega d}$ is close to 1, therefore:

$$k_T \approx k_{\Omega d} = \left(\frac{2\Omega}{\nu}\right)^{1/2}. \tag{4.2}$$

This relation identifies k_T as the wavenumber at which the rotation time equals the characteristic dissipation time, provided that k_Ω/k_η is not too large (in practice, $k_\Omega \lesssim k_\eta/4$). In other words, at small wavenumbers anisotropy quickly decreases with the wavenumber, then reaches a minimum at $k \approx k_{\Omega d}$, after which it slowly increases up to the dissipative scales. Also recalling from Chapter 1 that, under the hypothesis $\omega' \sim \nu k_\eta^2$, Ro^ω should scale as $(k_\eta/k_\Omega)^{2/3}$, Eq. (4.2) yields

$$k_T \sim k_\Omega Ro^\omega. \tag{4.3}$$

To check this, k_T/k_Ω is plotted as a function of Ro^ω in Fig. 4.11(a). Again, this scaling is satisfied for the data corresponding to $k_\Omega < k_\eta/4$, and the proportionality factor is close to 1.

In order to make sure that the scaling law found above is not artificially induced by the forcing, further investigation is required. If rotation is too weak, the threshold wavenumber k_T may be close enough to k_F for the forcing scheme to affect its value. In Fig. 4.11(b), k_T/k_F

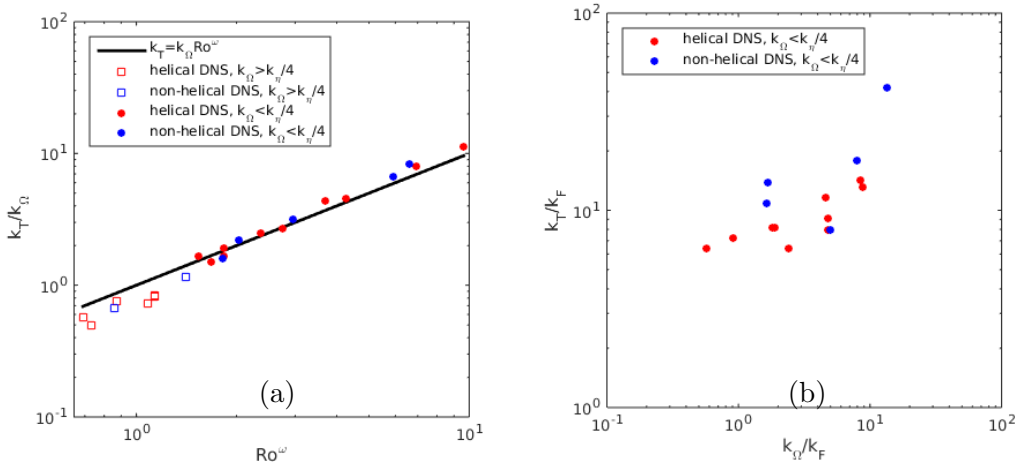

Figure 4.11: (a) k_T/k_Ω plotted as a function of Ro^ω, (b) k_T/k_F plotted as a function of k_Ω/k_F.

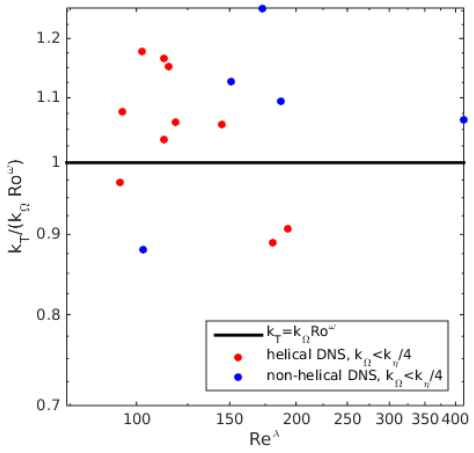

Figure 4.12: Dependence of the k_T scaling law on the Reynolds number.

is plotted as a function of k_Ω/k_F (runs for which $k_\Omega > k_\eta/4$ are not included). No trend is visible from these data, so that no forcing effect is detected. Such an effect might, however, be evidenced in simulations with larger forcing wavenumber or larger Rossby number.

Finally, we investigate the dependence of the k_T scaling law on the Reynolds number. In Fig. 4.12 $k_T/\left(k_\Omega Ro^\omega\right)$ is plotted as a function of Re^λ. As already shown in Fig. 4.11(a), this quantity is always close to one. Moreover, there is no correlation between it and Re^λ. It seems therefore that, in the range covered by our runs, the scaling law of k_T (Eq. (4.2) or (4.3)) does not depend on the Reynolds number.

Note that in the asymptotic inviscid limit, according to our scaling law, $k_T \sim k_{\Omega d} \to \infty$

and thus only the low-wavenumber anisotropic range ($k < k_T$) should persist. In this range anisotropy decreases with wavenumber, which is consistent with the classical argument according to which isotropy should be obtained at scales infinitely smaller than the Zeman scale (if the minimum of $a(k)$ tends to zero).

Comparing the above results—in particular the presence of small scale anisotropy and the scaling law for the threshold wavenumber in large Rossby number rotating turbulence—with data from other works in the literature would be essential. Three main articles focusing on small scale anisotropy in rotating turbulence are currently available [25, 46, 53]. However, in [46, 53] no scale-normalized indicator is shown, and therefore it is impossible to estimate the anisotropy level at small scales and to compute the threshold wavenumber. In [25] a scale-normalized indicator is shown for several runs, but only in one run this indicator displays a minimum and a visual estimation of k_T is difficult. Furthermore, in these three works non-equilibrium turbulence (decaying turbulence in [25, 46] and forced unsteady turbulence with the presence of an inverse cascade in [53]) is studied, which may give rise to different phenomenological laws with respect to forced statistically stationary turbulence.

4.5 Statistics in separation space

In this section the anisotropic scale-dependent structure of rotating turbulence is analyzed in the space of separation vectors in physical space. In particular, we show the distributions of the quantities appearing in the Kármán-Howarth-Monin equation (1.88): the two-point velocity correlation $R(\boldsymbol{r})$, the third-order vector moment $\boldsymbol{\mathcal{F}}(\boldsymbol{r}) = \langle \delta\boldsymbol{u}\delta u_i \delta u_i \rangle$ and its divergence, the dissipation term $\nu\nabla^2 R(\boldsymbol{r})$ and the forcing term $\Phi(\boldsymbol{r})$, computed as described in section 2.2.2. We only recall here that $\delta\boldsymbol{u}$ is the velocity increment and that we call ρ and ζ the horizontal (normal to the axis of symmetry) and vertical (parallel to the axis) components of the separation vector $\boldsymbol{r}$ in physical space. The separation distances are nondimensionalized by the Kolmogorov scale η which can be easily computed in the simulations.

Our numerical results are also compared to experimental data obtained by P.-P. Cortet and F. Moisy [21] from decaying turbulence generated by a towed grid. Similar measurements were recently achieved by Lamriben *et al.* [46]. In these experiments, velocity is measured in a vertical plane (containing $\boldsymbol{\Omega}$) using corotating two-dimensional particle image velocimetry. When compared to data from simulations, the difference amounts essentially to the contribution of the off-plane velocity component. Although experiments and simulations are not designed

for a one-to-one comparison, rather universal features are observed, which attests of generic mechanisms generating anisotropy in rotating turbulence. Estimating ϵ from $-\partial_t R/2(\boldsymbol{r}=\mathbf{0})$ in the experiment gives $\eta \approx 0.6$ mm. The axes values in the experiment figures presented below are in dimensional form and the axis labels r_x and r_z are the components of $\boldsymbol{r}$ in a cartesian frame (x, y, z) with z parallel to $\boldsymbol{\Omega}$.

4.5.1 Two-point velocity correlation

Figure 4.13 provides the maps of the velocity correlation $R(\mathbf{r})$ at $\Omega = 0$ for runs $\mathrm{A_{nh}}$ (Euler-forced, $k_F = 5.5$) and $\mathrm{D_{nv}}$ (negative viscosity scheme, $k_F = 2.5$). The white dashed circle shows the forcing scale $L_F = 2\pi/k_F$. The same quantity is plotted in Figs. 4.14(a) and (b), for the non-rotating experiment by P.-P. Cortet and F. Moisy [21], at times $t\,V_g/M = 50$ and 400 after the grid translation, where $V_g = 1$ m s^{-1} and $M = 40$ mm are the grid velocity and mesh size, respectively. For run $\mathrm{A_{nh}}$ no departure from isotropy can be detected at any scales, as shown in Figs 4.13(a) and (b). For run $\mathrm{D_{nv}}$ in Figure 4.13(c), the large scales deviate slightly from isotropy, but smaller inertial scales sufficiently separated from the forcing one quickly become isotropic (Figure 4.13d). In the experiment, at $t\,V_g/M = 50$ the iso-level curves are nearly circular, but a slight decrease of $R(\boldsymbol{r})$ along the directions $\theta = 0$ and $\theta = \pi/2$ is observed for scales r larger than $0.6M$. However, at $t\,V_g/M = 400$, the distribution of $R(\mathbf{r}, t)$ is almost perfectly isotropic at all the resolved scales (Fig. 4.14b). In all the simulations and in the experiment $R(\boldsymbol{r})$ is maximal at $\boldsymbol{r} = \mathbf{0}$ and, for a fixed direction θ, it monotonically decreases with the scale.

The two-point velocity correlation is computed in DNS of forced rotating turbulence for runs $\mathrm{S^2_{nh}}$ ($Re^\lambda = 187$ and $Ro^\omega = 2.02$) and $\mathrm{R^2_{nh}}$ ($Re^\lambda = 149$ and $Ro^\omega = 0.857$), and plotted in Fig. 4.15. For the higher Rossby number run ($\mathrm{S^2_{nh}}$) the isolines of $R(\boldsymbol{r})$ are clearly elongated along the vertical direction. For the lower Rossby number run ($\mathrm{R^2_{nh}}$) the same behaviour (although more evident) is observed at small scales, while at large scales $R(\boldsymbol{r})$ is almost independent of ζ. In all the rotating runs the correlation is systematically larger at lower θ, *i.e.* closer to the rotation axis. Of course the isolines are more anisotropic in the lower Rossby number case. For the rotating experiment by P.-P. Cortet and F. Moisy [21] (Figures 4.14c and d), at $tV_g/M = 50$, the two-point correlation is almost identical to that found at $\Omega = 0$, confirming that the turbulence generated by the grid is not affected by rotation. However, at time $t\,V_g/M = 400$, $R(\boldsymbol{r})$ is strongly anisotropic with an enhanced correlation along the rotation axis, in agreement with the DNS.

These anisotropic features suggest the presence of vertically elongated structures, consistently

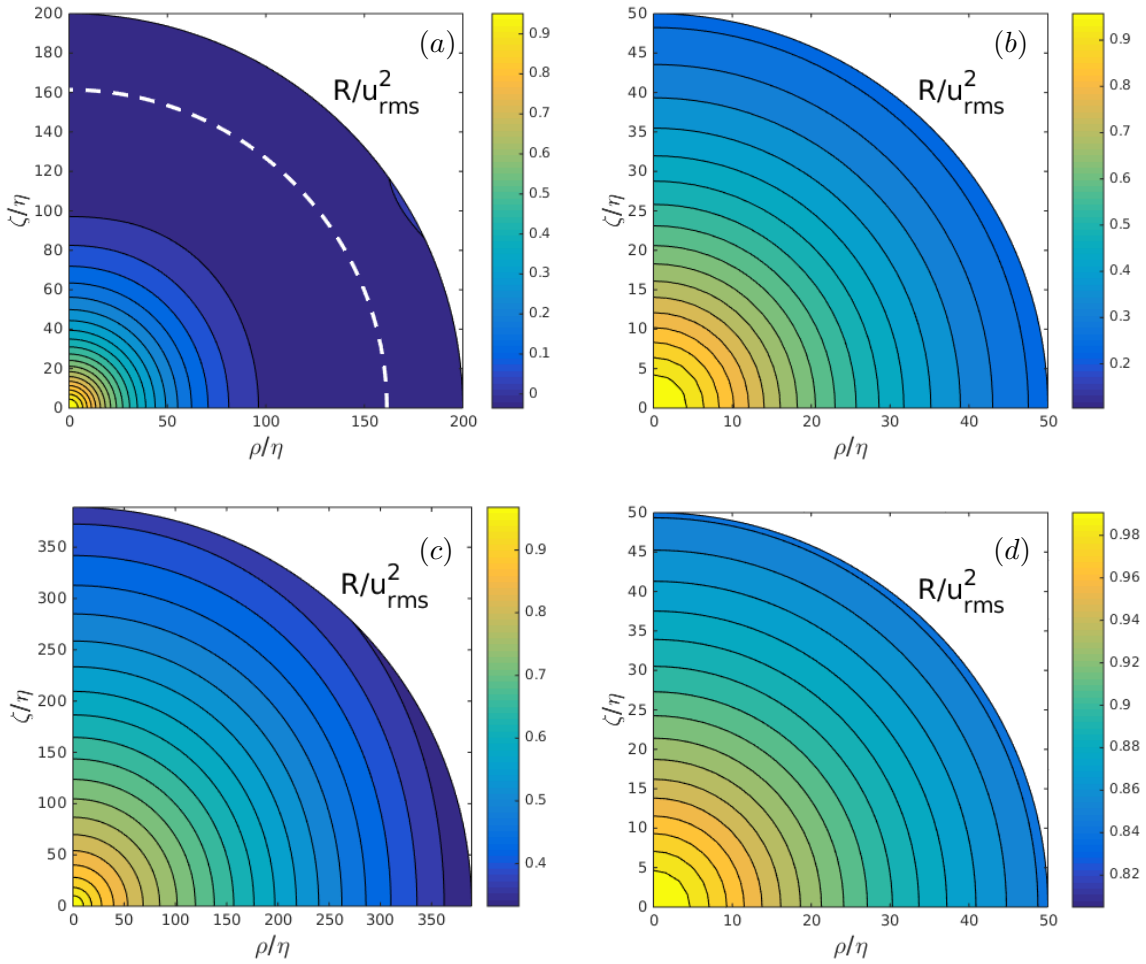

Figure 4.13: Maps of the two-point velocity correlation $R(\boldsymbol{r})$ for: (a) and (b) run $\mathrm{A_{nh}}$ corresponding to non-rotating Euler-forced turbulence, and (c) and (d) run $\mathrm{D_{nv}}$ corresponding to non-rotating turbulence forced through the negative viscosity scheme [38]. Two different plotting ranges are used in the right and left columns. The white dashed circle shows the forcing scale $L_F = 2\pi/k_F$.

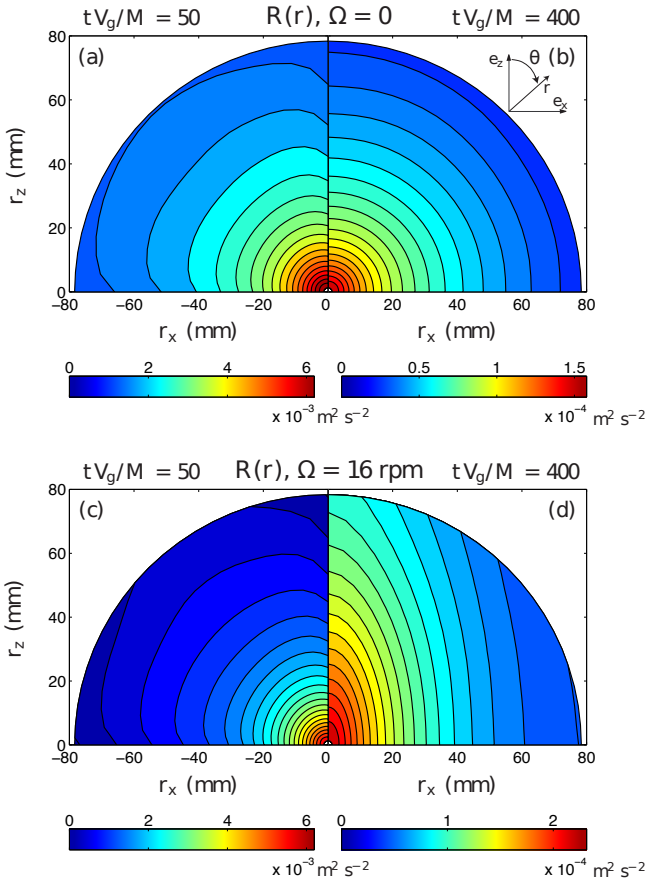

Figure 4.14: Maps of the two-point velocity correlation $R(\mathbf{r})$ at times $t\,V_g/M = 50$ (a and c) and $t\,V_g/M = 400$ (b and d) after the grid translation, for $\Omega = 0$ and 16 rpm. Experimental results by P.-P. Cortet and F. Moisy [21].

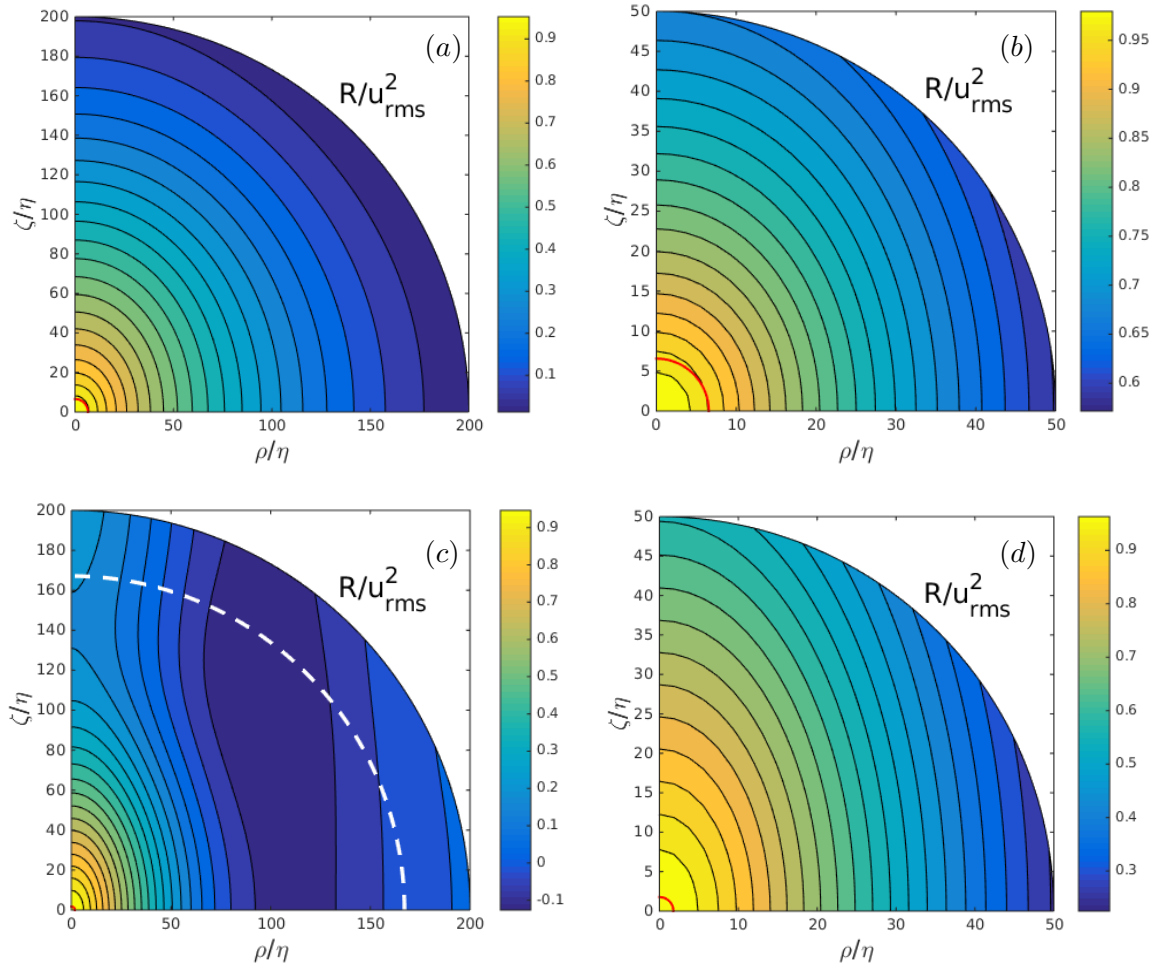

Figure 4.15: Maps of the two-point velocity correlation $R(\boldsymbol{r})$ for: (a) and (b) run $\mathrm{S}^2_{\mathrm{nh}}$ (Euler-forced, $Re^{\lambda} = 187$ and $Ro^{\omega} = 2.02$), and (c) and (d) run $\mathrm{R}^2_{\mathrm{nh}}$ (Euler-forced, $Re^{\lambda} = 149$ and $Ro^{\omega} = 0.857$). The white dashed circle shows the forcing scale $L_F = 2\pi/k_F$. The red circles show the Zeman scale $r_\Omega = \sqrt{\epsilon/(2\Omega)^3}$.

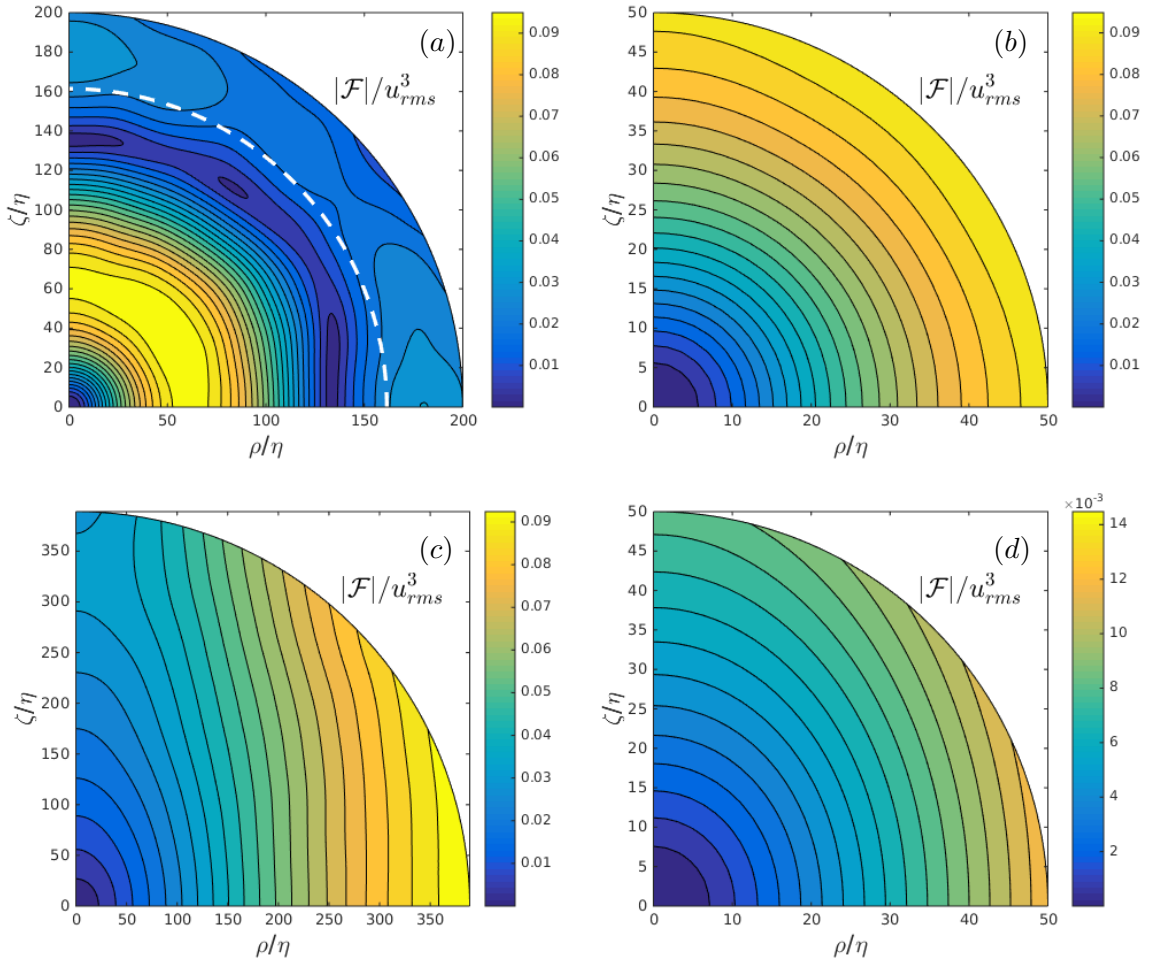

Figure 4.16: Modulus of the third-order vector moment $|\boldsymbol{\mathcal{F}}(\boldsymbol{r})|$ for: (a) and (b) run A_{nh} corresponding to non-rotating Euler-forced turbulence, and (c) and (d) run D_{nv} corresponding to non-rotating turbulence forced through the negative viscosity scheme [38]. The white dashed circle shows the forcing scale $L_F = 2\pi/k_F$.

with the analysis of the energy and polarization directional spectra carried out in sections 4.2 and 4.3. A purely 2D-3C turbulence would correspond to $R(\boldsymbol{r})$ independent of ζ, *i.e.* to vertical iso-R lines.

4.5.2 Third-order vector moment

We now consider the third-order vector moment $\boldsymbol{\mathcal{F}}(\boldsymbol{r})$, and compare its magnitude $|\boldsymbol{\mathcal{F}}|$ between the non-rotating and rotating cases.

For the non-rotating case, the iso-magnitude curves are shown in Fig. 4.16 for the non-rotating DNS and in Fig. 4.19b for the experiment by P.-P. Cortet and F. Moisy [21]. Since

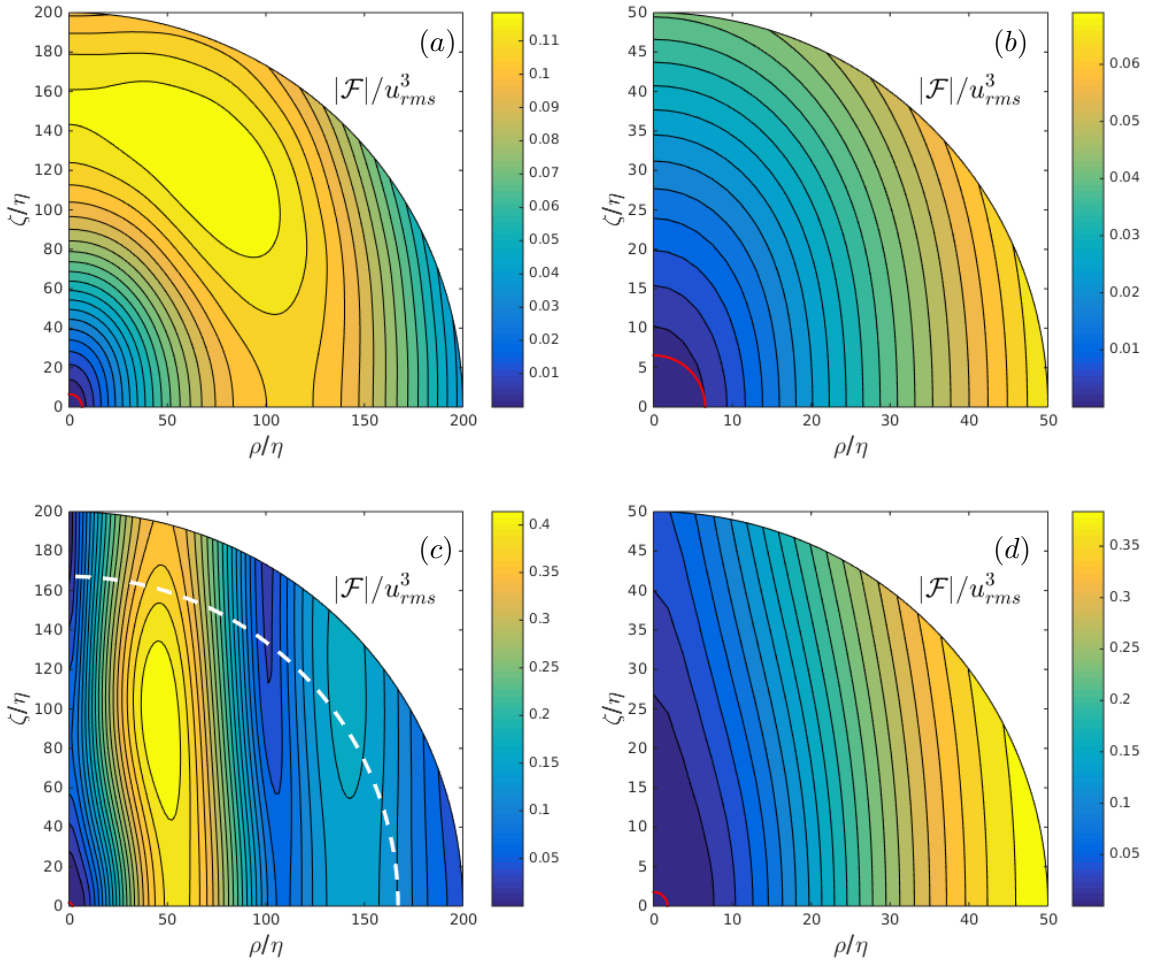

Figure 4.17: Modulus of the third-order vector moment $|\boldsymbol{\mathcal{F}}(\boldsymbol{r})|$ for: (a) and (b) run $\mathrm{S}^2_{\mathrm{nh}}$ (Euler-forced, $Re^\lambda = 187$ and $Ro^\omega = 2.02$), and (c) and (d) run $\mathrm{R}^2_{\mathrm{nh}}$ (Euler-forced, $Re^\lambda = 149$ and $Ro^\omega = 0.857$). The red dashed circle shows the forcing scale $L_F = 2\pi/k_F$. The white circles show the Zeman scale $r_\Omega = \sqrt{\epsilon/(2\Omega)^3}$.

the azimuthal component F_φ is not measured in the experiment, the magnitude in Fig. 4.19 is actually the 2D norm in a vertical plane $|(\mathcal{F}_\rho, \mathcal{F}_\zeta)|$. For both run $\mathrm{A_{nh}}$ and the non-rotating experiment, the iso-$|\boldsymbol{\mathcal{F}}|$ are nearly circular. On the other side, the run forced through the negative viscosity scheme ($\mathrm{D_{nv}}$) displays a more anisotropic distribution for $|\boldsymbol{\mathcal{F}}|$, and only the smaller scales are approximately isotropic. This behaviour depends on the anisotropy artificially created by the forcing method, as explained in Chapter 3. Note that in the DNS a wider range has been retained for Fig. 4.16 with respect to the experiment (Fig. 4.19b), where statistical convergence limits the large-scale resolution to about 67η.

For the experimental case rotating at $\Omega = 16$ rpm, Fig. 4.19(d), the iso-$|\boldsymbol{\mathcal{F}}|$ lines show a

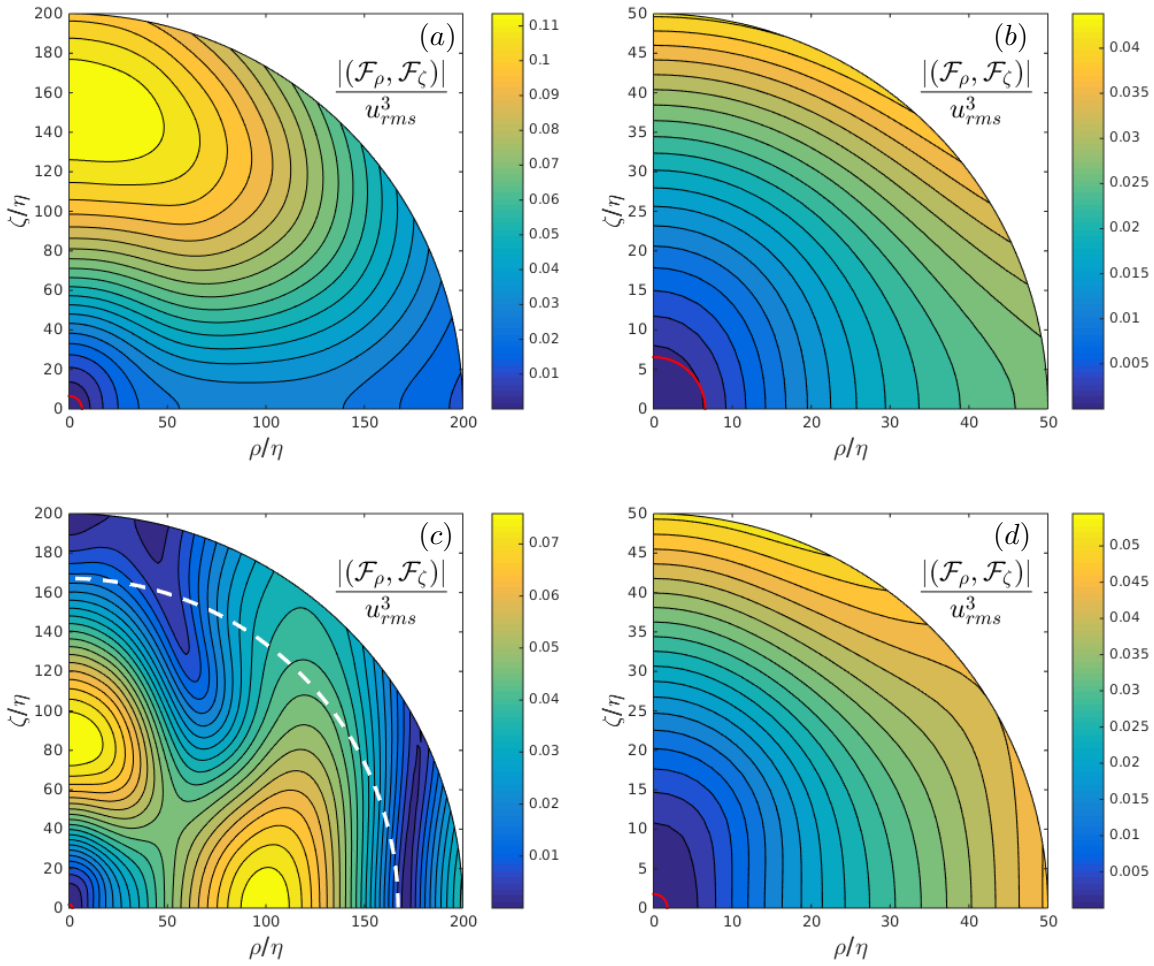

Figure 4.18: Modulus of $(\mathcal{F}_\rho, \mathcal{F}_\zeta)$ for: (a) and (b) run $\mathrm{S}^2_{\mathrm{nh}}$ (Euler-forced, $Re^\lambda = 187$ and $Ro^\omega = 2.02$), and (c) and (d) run $\mathrm{R}^2_{\mathrm{nh}}$ (Euler-forced, $Re^\lambda = 149$ and $Ro^\omega = 0.857$). The white dashed circle shows the forcing scale $L_F = 2\pi/k_F$. The red circles show the Zeman scale $r_\Omega = \sqrt{\epsilon/(2\Omega)^3}$.

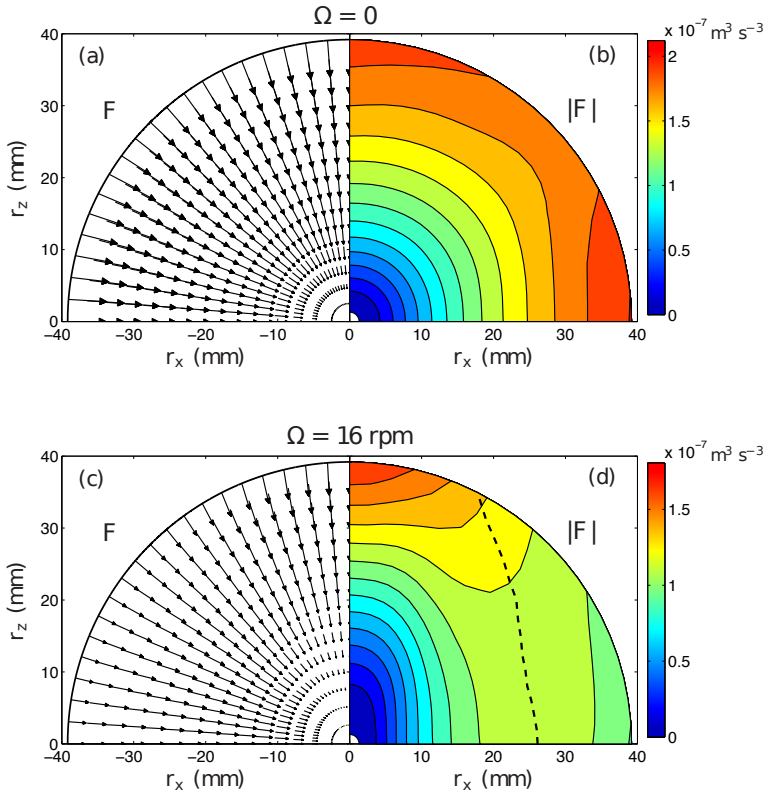

Figure 4.19: Third-order vector moment $\boldsymbol{\mathcal{F}}$ at time $t\,V_g/M = 400$ after the grid translation for $\Omega = 0$ (top) and $\Omega = 16$ rpm (bottom). In (d), the dashed line shows the "crest line" following the local maximum of $|\boldsymbol{\mathcal{F}}|$. Experimental results by P.-P. Cortet and F. Moisy [21].

strong anisotropy that extends up to the largest resolved scales, similar to that of $R(\boldsymbol{r})$. At fixed scale r, the maximum of $|\boldsymbol{\mathcal{F}}|$ is systematically encountered for vertical separations ($\theta = 0$). Along the horizontal direction ($\theta = \pi/2$) $|\boldsymbol{\mathcal{F}}|$ reaches a maximum before decreasing. A similar concentration of magnitude is also observed in the rotating DNS of runs $\mathrm{S}^2_{\mathrm{nh}}$ and $\mathrm{R}^2_{\mathrm{nh}}$ in Fig. 4.17. Nevertheless, the shape of the isolines of Fig. 4.17(d) significantly differs from the experimental one of Fig. 4.19(d). However, if one adopts the same way of computing $\boldsymbol{\mathcal{F}}$ as the experiments, *i.e.* by considering only the $\mathcal{F}_\rho$ and $\mathcal{F}_\zeta$ components, Fig. 4.18 is obtained. This figure displays a distribution more similar to that in the experiment, especially for the lower Rossby number run ($\mathrm{R}^2_{\mathrm{nh}}$, Figs. 4.18c-d). This also shows that the azimuthal component of $\boldsymbol{\mathcal{F}}$ is relevant with respect to the other ones.

Maps of the radial, polar and azimuthal components of $\boldsymbol{\mathcal{F}}$ for the non-rotating and the rotating DNS are plotted in Fig. 4.20. For run A_{nh} (non-rotating, Euler-forced, panels a-c), the amplitudes of $\mathcal{F}_\theta$ and $\mathcal{F}_\varphi$ are naturally much smaller than that of $\mathcal{F}_r$, which is θ-independent, so that their contribution to the third-order vector moment magnitude is unimportant. As expected from the results of Chapter 3 on forcing anisotropy, for run D_{nv} (non-rotating, forced through the negative viscosity scheme, panels d-f) the off-radial components are more important and $\mathcal{F}_r$ slightly depends on θ. Therefore, these figures confirm the isotropic distribution in the non rotating case of run A_{nh} and the anisotropic effect of forcing in run D_{nv}. On the other hand, for the rotating cases, Figs. 4.20(g)-(n) show that $\mathcal{F}_r$ is responsible for the concentration of $|\boldsymbol{\mathcal{F}}|$ along the vertical axis. In particular, at smaller scales $\mathcal{F}_r$ decreases with θ, while at larger scales it increases with θ. At small scales F_φ does not depend on ζ, is zero for $\rho = 0$ and it increases with ρ. This is related to the cyclone-anticyclone asymmetry [7, 29, 36, 59, 60, 78]. Now both $\mathcal{F}_\varphi$ and $\mathcal{F}_\theta$ in Figs. 4.20(g)-(n) do contribute significantly to $|\boldsymbol{\mathcal{F}}|$ and tend to shift its peak away from the ζ-axis. Note that, while $\mathcal{F}_\varphi$ is always positive in the range of scales shown, $\mathcal{F}_\theta$ is positive everywhere but in a small region at small scales and intermediate θ, where it is slightly negative.

Although the third-order vector moment $\boldsymbol{\mathcal{F}}$ is the most direct signature of non-linearity that can be computed from the velocity fields, it enters into the KHM equation only through its divergence. The physical interpretation of $\boldsymbol{\mathcal{F}}$ itself is therefore delicate, and the anisotropy generation mechanism is investigated in the following directly from the non-linear term $\Pi = \nabla \cdot \boldsymbol{\mathcal{F}}/4$, which is the source of anisotropy for the two-point correlation in the KHM equation (1.88).

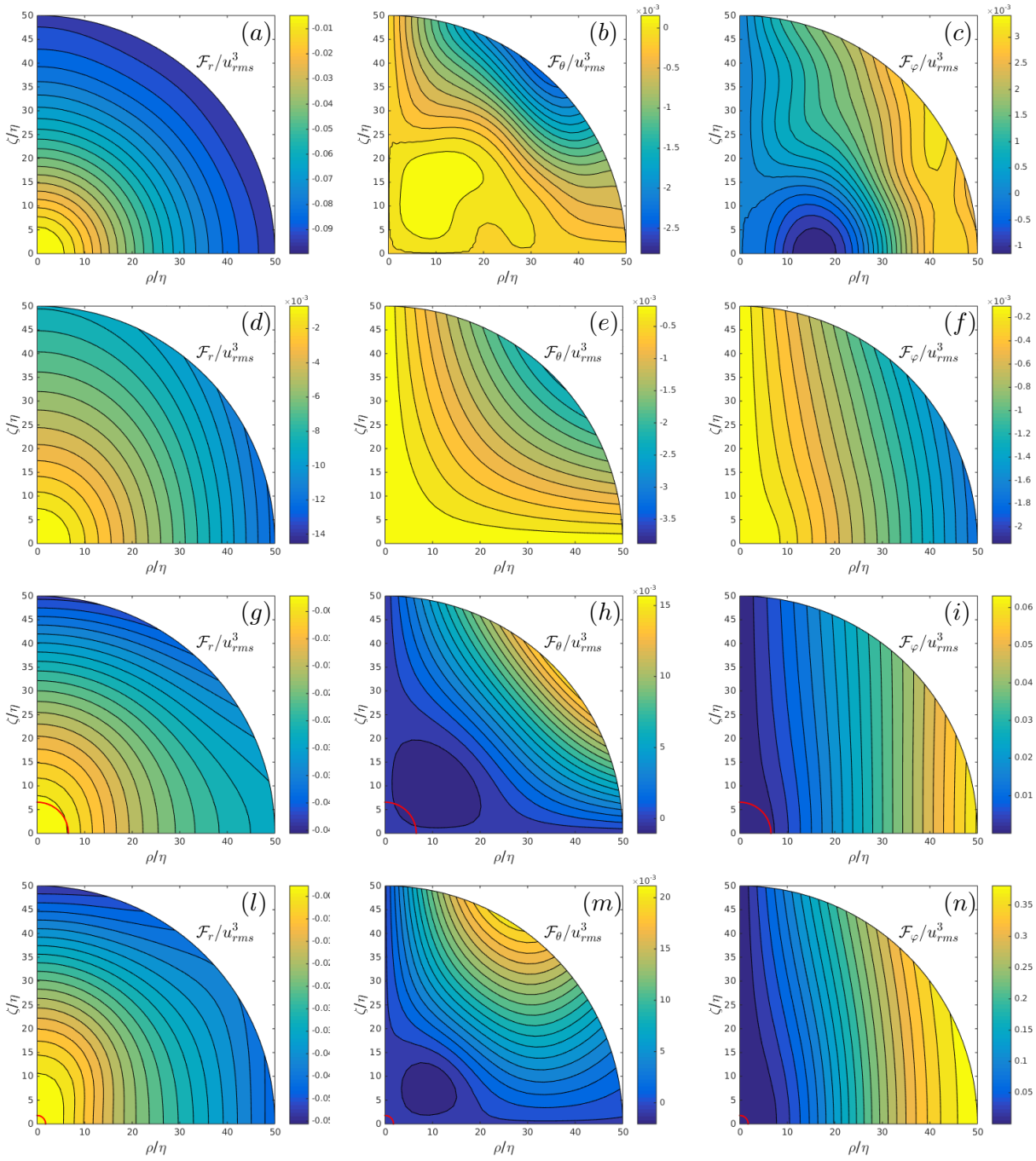

Figure 4.20: Maps of the components of the third-order vector moment $\boldsymbol{\mathcal{F}}$ in the polar-spherical reference frame. Left column for the radial component $\mathcal{F}_r$, middle column for the polar component $\mathcal{F}_\theta$, right column for the azimuthal component $\mathcal{F}_\varphi$. Panels (a)-(c) for run $\mathrm{A_{nh}}$ (non-rotating Euler-forced); panels (d)-(f) for run $\mathrm{D_{nv}}$ (non-rotating forced through the negative viscosity scheme); panels (g)-(i) for run $\mathrm{S^2_{nh}}$ (moderate Rossby number, Euler-forced); panels (l)-(n) for run $\mathrm{R^2_{nh}}$ (low Rossby number, Euler-forced). The red circles show the Zeman scale $r_\Omega = \sqrt{\epsilon/\left(2\Omega\right)^3}$.

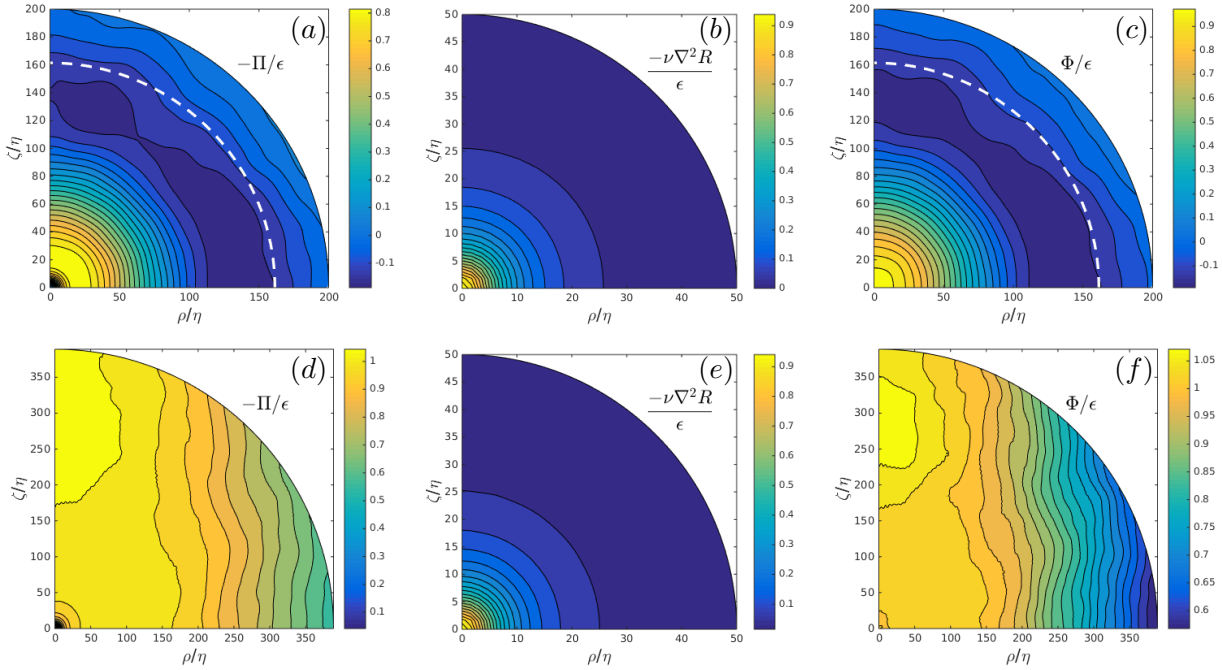

Figure 4.21: Maps of the terms appearing in the KHM equation, for DNS of isotropic turbulence, for (a)-(c) run A_{nh} corresponding to non-rotating Euler-forced turbulence, and (d)-(f) run D_{nv} corresponding to non-rotating turbulence forced through the negative viscosity scheme. White dashed circles indicate the forcing scale. A smaller range of scales is considered for the viscous term $\nu\nabla^2 R$.

4.5.3 Balance of the terms in the KHM equation

Isotropic case

In this section we examine in detail the distributions of the different terms in the KHM equation (1.88), in terms of scale and anisotropy. According to this equation, the dynamics of the flow results from: (i) the non-linear term $\Pi(\boldsymbol{r}) = \nabla \cdot \boldsymbol{\mathcal{F}}/4$, which accounts for the effect of advection; (ii) the dissipative term $D(\boldsymbol{r}) = -\nu\nabla^2 R$; (iii) the forcing term $\Phi(\boldsymbol{r})$ (statistically stationary forced simulations) or $\partial R(\boldsymbol{r})/\partial t$ (experiments of freely decaying turbulence).

We show the maps of these quantities for the DNS data of isotropic turbulence with Euler forcing and for the non-rotating experiment by P.-P. Cortet and F. Moisy [21] in Figs. 4.21 and 4.23, respectively. Both Φ in the simulation and $-\partial R/\partial t$ in the experiment are maximal at $\boldsymbol{r} = \boldsymbol{0}$. As expected from the arguments explained in section 1.2.2, the DNS also show that Φ is almost constant and approximately equal to ϵ in a range of small scales, this range being wider

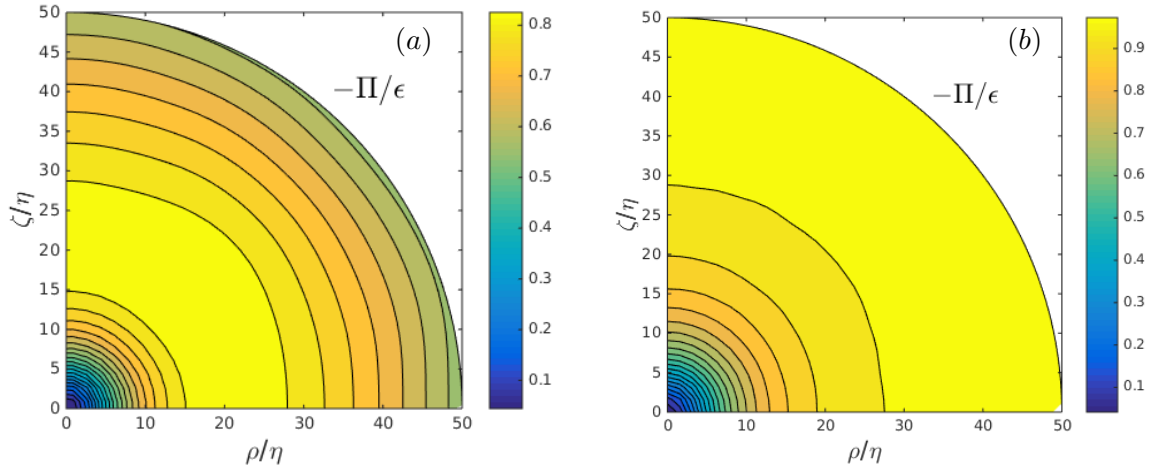

Figure 4.22: Maps of the nonlinear terms appearing in the KHM equation, for DNS of isotropic tubulence, for (a) run A_{nh} corresponding to non-rotating Euler-forced turbulence, and (b) run D_{nv} corresponding to non-rotating turbulence forced through the negative viscosity scheme. A reduced range of scales has been used with respect to Fig. 4.21. The red circles show the Zeman scale $r_\Omega = \sqrt{\epsilon/(2\Omega)^3}$.

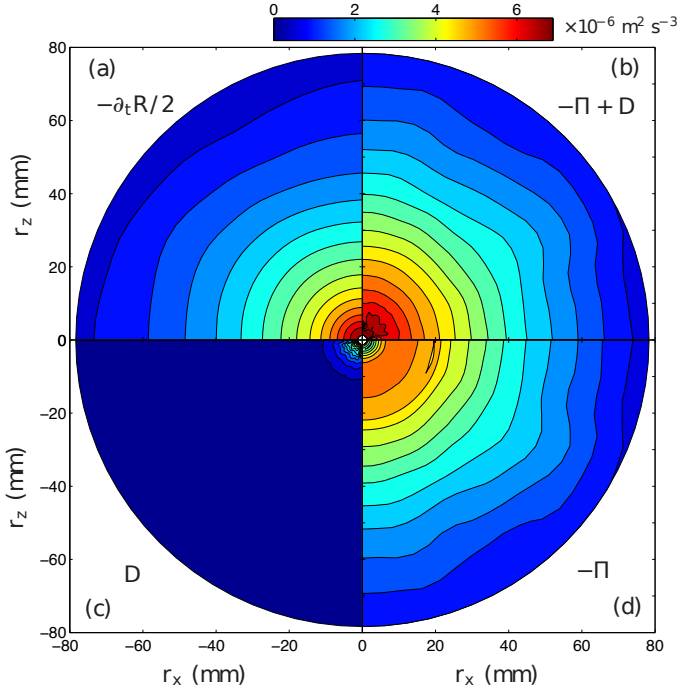

Figure 4.23: Maps of the terms of the KHM equation for the non-rotating experiment at time $t\,V_g/M = 400$. (a) Unstationary term $-\partial_t R/2$, (c) dissipative term $D = -\nu\nabla^2 R$, (d) nonlinear term $-\Pi = -\nabla \cdot \mathbf{F}/4$, (b) r.h.s. of the KHM equation $-\Pi + D$. Experimental results by P.-P. Cortet and F. Moisy [21].

in the case of the larger Reynolds number run (D_{nv}, Fig. 4.21f). For run A_{nh}, Φ also displays a negative minimum close to $L_F = 2\pi/k_F$ in Fig. 4.21(c). If only wavenumbers of modulus k_F were excited, the most negative contribution of the forcing term (which is the even part of the velocity-external force correlation) would be at π/k_F, but since Euler forcing involves lower wavenumbers too this minimum shifts to a larger scale.

Figure 4.21(a) shows the non-linear term $\Pi = \nabla \cdot \boldsymbol{\mathcal{F}}/4$ for run A_{nh}, with a slight departure from exact circular distribution in the large scales due to noise, as also observed in the experimental data by P.-P. Cortet and F. Moisy [21] of Fig. 4.23(d). Π tends to zero at small scales, and shows a broad negative minimum (close to $-\epsilon$ for the DNS) in an annular region, as expected in the inertial range. Very good isotropy is obtained at smaller scales, as shown in Fig. 4.22(a). For run D_{nv} (Figs. 4.21d and 4.22b) $\Pi(\boldsymbol{r})$ is approximately isotropic at small scales and is almost constant in a wide range of large scales.

The dissipative term shown in Figs. 4.21(b) and (e) for the DNS over a reduced range of scales, exhibits a perfect isotropic distribution, while the noise in $D = -\nu\nabla^2 R$ for the experiment in Fig. 4.23(c) originates from discretization effects at small scale in the computation of the discretized Laplacian. The viscous term takes significant values only at small scales, for $r \lesssim 20\eta$ in the DNS.

A reasonable match between the shape of the experiment maps of $-\partial_t R/2$ and $-\Pi + D$ is observed in Figs. 4.23(a,b). The discrepancy, of order of 30% at this time, originates from the missing azimuthal component in the 2D surrogates.

It is also useful to plot the quantities appearing in the KHM equation as a function of the scale r for a constant θ. Figure 4.24 displays Φ, $-\Pi = -\nabla \cdot \boldsymbol{\mathcal{F}}/4$ and $D = -\nu\nabla^2 R$ as functions of r along $\theta = 0$ and $\theta = \pi/2$ for runs A_{nh} and D_{nv}. Similarly, in Fig. 4.25(a) $\partial R/\partial t$, $-\Pi$ and D averaged over θ are plotted as functions of the scale r for the non-rotating experiment by P.-P. Cortet and F. Moisy [21]. The crossover between the inertial and dissipative terms in the KHM equation ($-\Pi = D$) is found at $r_\nu \approx 6\eta$ in numerical simulations of isotropic turbulence. In the non-rotating experiment one finds $r_\nu \approx 2.5$ mm, corresponding to $r_\nu \approx 4.5\eta$, which is slightly smaller (but of the same order) than the ratio reported in numerical simulations. A good agreement is found in Figure 4.25(b) between the time evolutions of the measured crossover r_ν and the computed value of $4.5\,\eta$. An extended inertial range, where $\Pi(\mathbf{r}) = -\epsilon$, is visible in Fig. 4.24(c)-(d) for run D_{nv}. For run A_{nh} (Fig. 4.24(a)-(b)) and the experiment (Fig. 4.25), only in a small range of scales $\Pi(\mathbf{r}) \approx -\epsilon$ due to moderate Reynolds numbers.

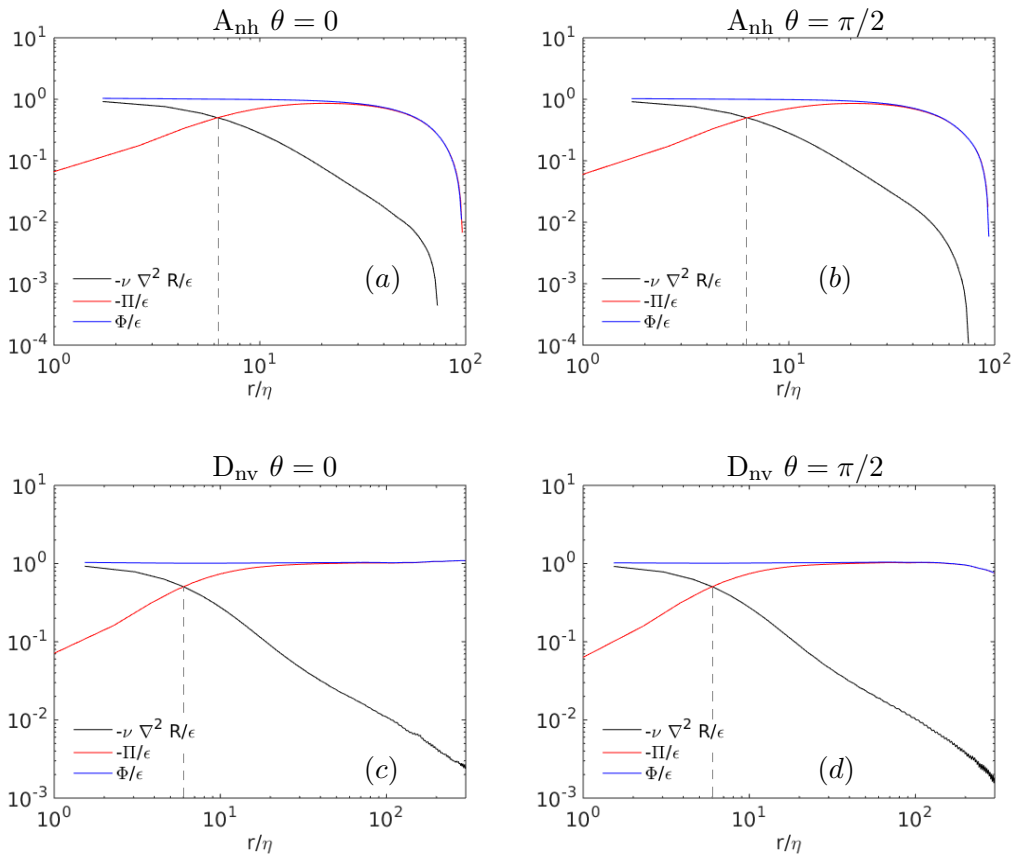

Figure 4.24: Terms of the KHM equation from DNS data of runs A_{nh} (bottom row) and D_{nv} (top row) along $\theta = 0$ (left column) and $\theta = \pi/2$ (right column).

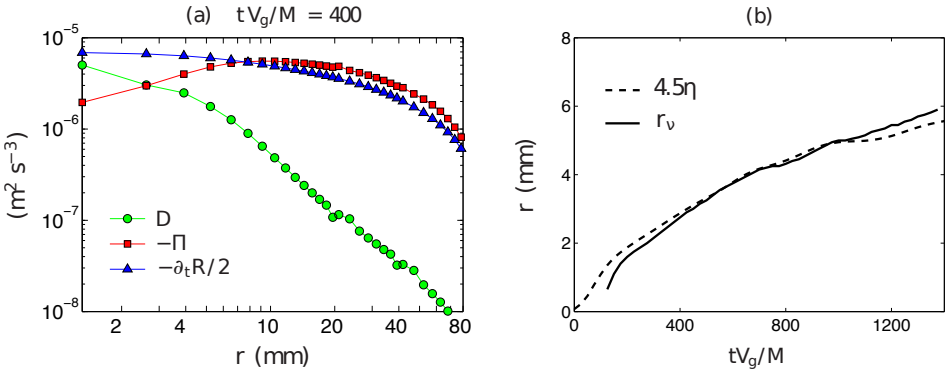

Figure 4.25: (a) Terms of the KHM equation averaged over θ for the non-rotating experiment as functions of r at $t\,V_g/M = 400$. (b) Time evolution of the cross-over scale r_ν and 4.5η. Experimental results by P.-P. Cortet and F. Moisy [21].

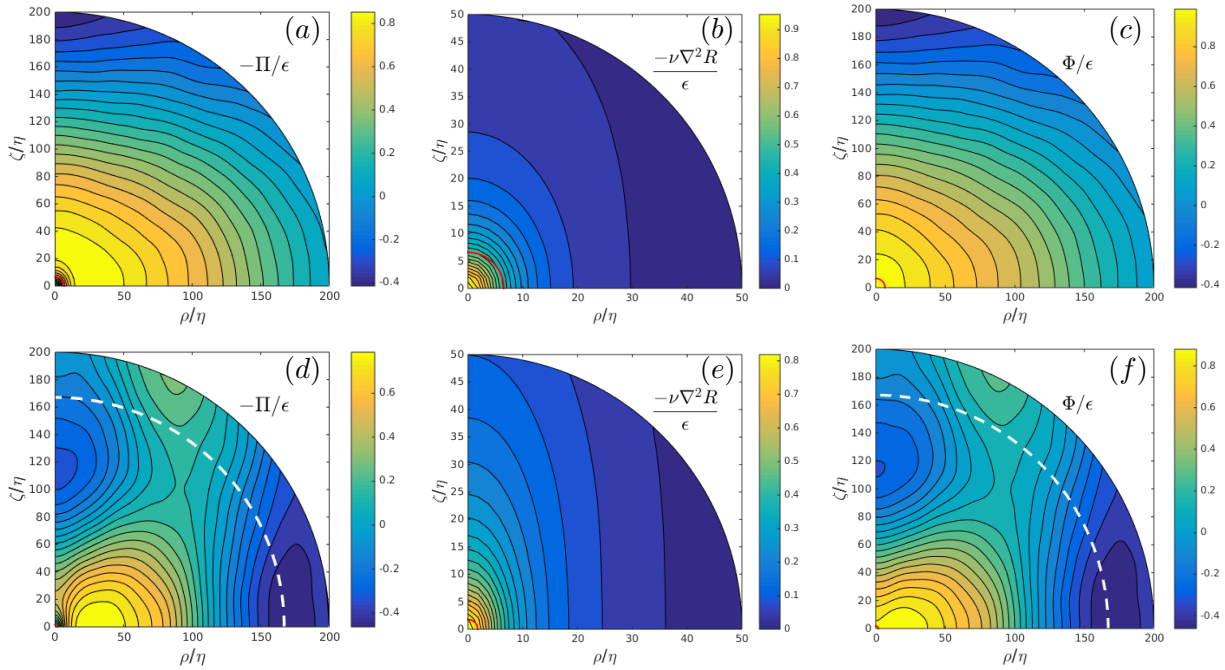

Figure 4.26: Maps of the terms appearing in the KHM equation for (a)-(c) run S^2_{nh}, and (d)-(f) run R^2_{nh} corresponding to rotating Euler-forced turbulence. A smaller range of scales is considered for the viscous term $\nu\nabla^2 R$. The white dashed circles indicate the forcing scale $L_F = 2\pi/k_F$. The red circles indicate the Zeman scale $r_\Omega = \sqrt{\epsilon/(2\Omega)^3}$.

Rotating case

In Figs. 4.26, 4.27 and 4.28, we compare again the maps of the three terms of the KHM equation, but now in the rotating DNS and the rotating experiment by P.-P. Cortet and F. Moisy [21]. The budget is qualitatively similar to that of the non-rotating case. However, in the experiment and in the DNS at sufficiently small scales $\Pi = \nabla \cdot \boldsymbol{\mathcal{F}}/4$ and $D = -\nu\nabla^2 R$ show the characteristic shape elongated along the rotation axis. The region where $-\Pi$ is most positive is along the horizontal axis, inducing a stronger reduction of the velocity correlation R at large θ than at small θ, and therefore resulting in a relative growth of the correlation along the vertical axis. Here again, this is consistent with a 2D trend. For the DNS, when even smaller scales are considered (Fig. 4.27), a trend towards isotropy is observed in $-\Pi$, as in the dissipative term (Fig. 4.26b).

A remarkable feature of Figs. 4.26 and 4.28 is that the balance between the dissipation term and the nonlinear term now strongly depends on the polar angle θ. The terms of the KHM equation for two polar angles $\theta = 0$ and $\pi/2$ are shown in Fig. 4.29 for the rotating turbulence

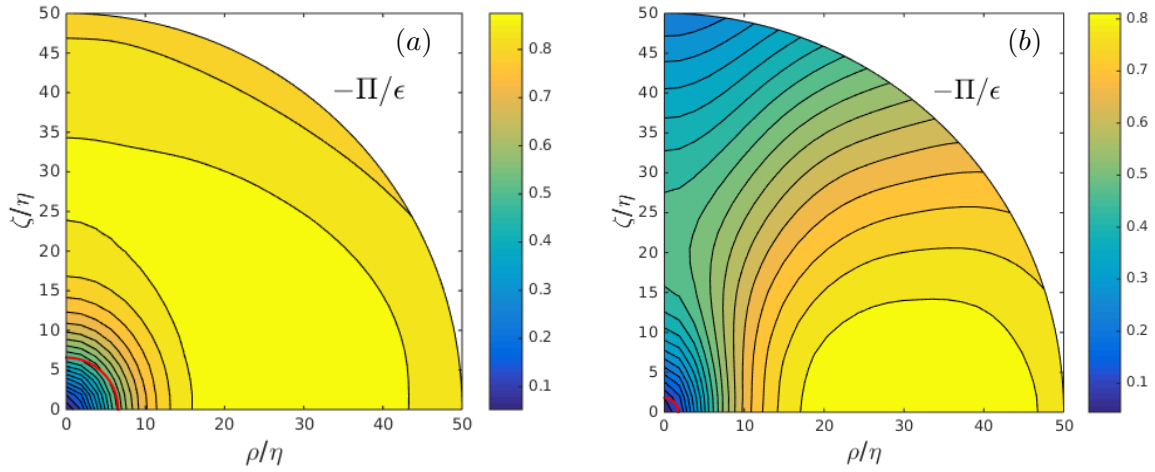

Figure 4.27: Maps of the non-linear term appearing in the KHM equation, for (a) run S^2_{nh}, and (b) run R^2_{nh} corresponding to rotating Euler-forced turbulence. A smaller range of scales is considered here with respect to Fig. 4.26 in order to show small scale anisotropy. The red circles show the Zeman scale $r_\Omega = \sqrt{\epsilon/(2\Omega)^3}$.

DNS data. Conclusions similar to the non-rotating DNS cases can be drawn. The larger cross-over scale r_ν found at $\theta = 0$ (vertical separation) is a simple consequence of the weaker nonlinear term Π in the vertical direction. In order to quantify this effect, we also computed the cross-over scales of other rotating DNS and plotted them as functions of the Rossby number in Fig. 4.30. This figure shows that, while the horizontal cross-over scale $r_\nu(\theta = \pi/2)$ is constant and equal to the value corresponding to the isotropic case ($r_\nu \approx 6\eta$), the cross-over scale can vary significantly for $\theta = 0$: it is within a range from 6η to 12η depending on the value of the micro-Rossby number in the range 9.6 (weak rotation) to 0.86 (strong rotation). In other words, decreasing the Rossby number significantly affects only the vertical cross-over scale.

4.6 Inertial law and dissipative range anisotropy

Returning to the third-order vector moment, inertial laws are available from the literature in both the isotropic and the rotating cases. In isotropic turbulence $\mathcal{F}_\varphi = \mathcal{F}_\theta = 0$ and $\mathcal{F}_r$ is given by the four-thirds Kolmogorov law (1.94) [4] recalled in section 1.2.2.

Figures 4.32(a)-(b) show that the streamlines of $\boldsymbol{\mathcal{F}}$ are exactly radial in the isotropic case of the Euler forced run (A_{nh}). However, Figs. 4.32(c)-(d) show that the anisotropy artificially

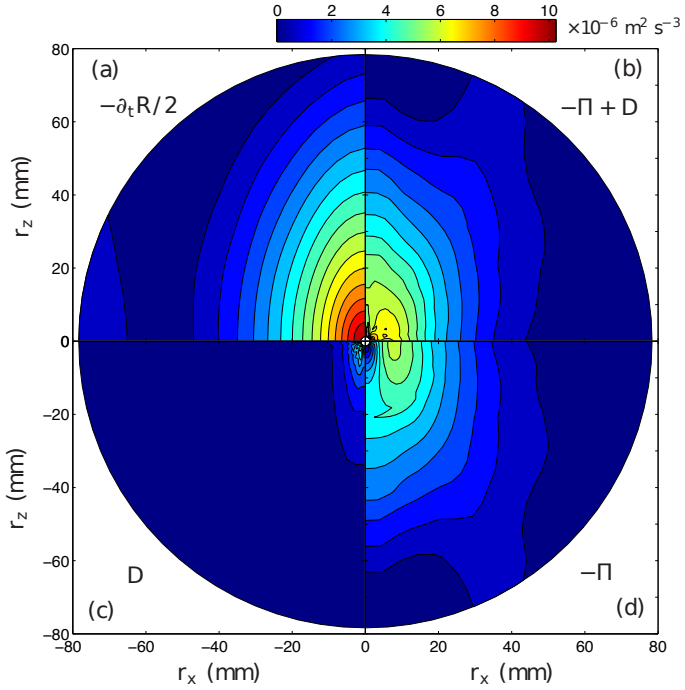

Figure 4.28: Maps of the terms of the KHM equation for the rotating experiment at $\Omega = 16$ rpm at time $t\,V_g/M = 400$ ($Re = 600$, $Ro = 0.06$). (a) Unstationary term $-\partial_t R/2$, (c) dissipative term $D = -\nu\nabla^2 R$, (d) transfer term $-\Pi = -\nabla \cdot \mathbf{F}/4$, (b) r.h.s. of the KHM equation $-\Pi + D$. Experimental results by P.-P. Cortet and F. Moisy [21].

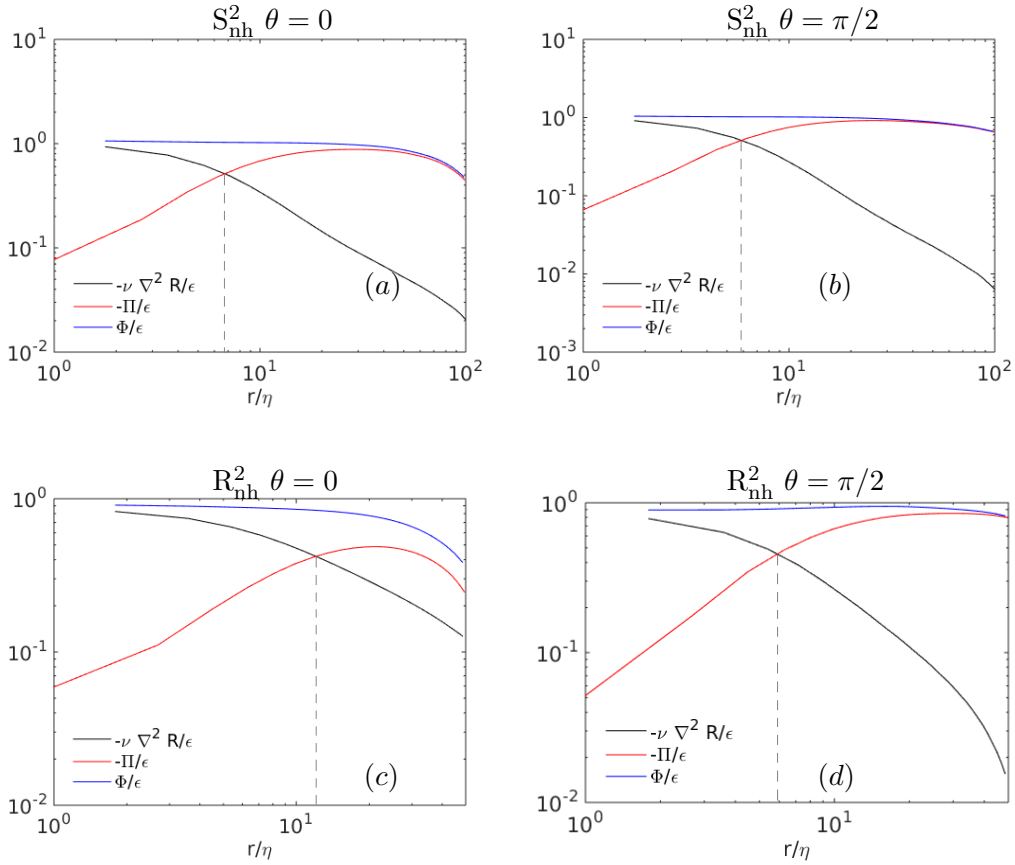

Figure 4.29: Terms of the KHM equation from DNS data of runs S^2_{nh} (bottom row) and R^2_{nh} (top row) along $\theta = 0$ (left column) and $\theta = \pi/2$ (right column).

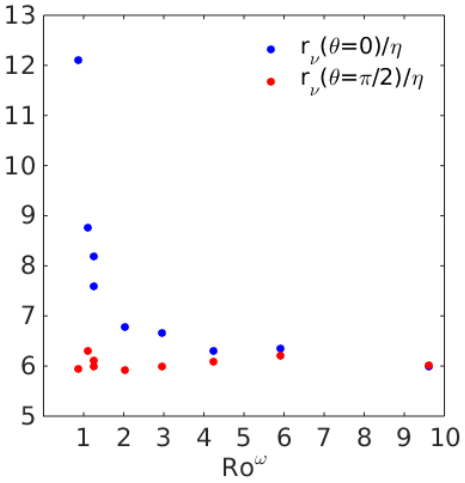

Figure 4.30: Cross-over scales along the vertical (blue markers) and the horizontal (red markers) directions as functions of the Rossby number.

generated by the forcing scheme in run D_{nv} significantly affects the third-order vector moment, leading to non radial streamlines even at the smallest resolved scales. As expected, also for the decaying isotropic turbulence experiment by P.-P. Cortet and F. Moisy [21], Fig. 4.19(a), $\boldsymbol{\mathcal{F}}$ is radial. Because the uncertainty on $\boldsymbol{\mathcal{F}}$ for $r > M$ is significantly larger than for second order quantities, the experimental visualizations are restricted to $r \leq M \approx 67\eta$. Figure 4.31 also shows the Kolmogorov-normalized radial component $\mathcal{F}_r/(-4\epsilon r/3)$ for $\theta = 0$ and $\theta = \pi/2$ for the non-rotating runs A_{nh} and D_{nv}, and for the rotating run S^2_{nh}. In the isotropic case of Fig. 4.31(a) the two curves superpose and the four-thirds Kolmogorov law is approximately verified in the inertial range. Note that moderate Reynolds number simulations are expected to display values $\mathcal{F}_r/(-4\epsilon r/3) < 1$ [3]. Very large Reynolds numbers are required to reach $\mathcal{F}_r/(-4\epsilon r/3) = 1$, but $\mathcal{F}_r$ should never overshoot the theoretical inertial value. Figure 4.31(b) shows that the anisotropy of run D_{nv} prevents $\mathcal{F}_r$ from reaching a plateau at this theoretical inertial value. In the case of rotating turbulence (Fig. 4.31c), while $\mathcal{F}_r(\theta = \pi/2)$ (red curve) seems to behave as in the isotropic case, $\mathcal{F}_r(\theta = 0)$ (blue curve) is significantly modified by rotation: compared with $\mathcal{F}_r(\theta = \pi/2)$ its modulus is smaller at small scales and larger at large scales (overshooting with respect to the isotropic inertial value). Again, as observed above for the cross-over scale, only the statistics along $\theta = 0$ appear to be affected by rotation.

A corresponding inertial law for rapidly rotating turbulence has been proposed by Galtier

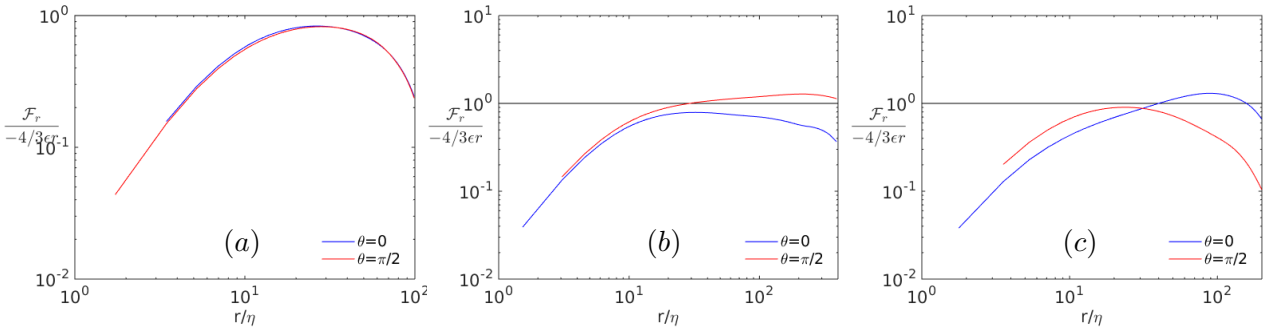

Figure 4.31: Third-order vector moment radial component $\mathcal{F}_r$ non dimensionalized by $-4\epsilon r/3$, along the directions $\theta = 0$ and $\pi/2$. Data for (a) Euler-forced non-rotating run A_{nh}; (b) run D_{nv}, forced through the negative viscosity scheme; (c) rotating turbulence simulation S^2_{nh}.

[30], the theory is also recalled in section 1.3.2. According to this theory, the streamlines of $\boldsymbol{\mathcal{F}}$ should be proportional to $\zeta = \rho^{4/3}$, $|\mathcal{F}_r|$ should slightly decrease with θ and $\mathcal{F}_\theta$ should be positive, *i.e.* $\boldsymbol{\mathcal{F}}$ should be deflected towards the horizontal axis with respect to the radial direction.

We plot the streamlines $\zeta(\rho)$ in linear and logarithmic scale for runs S^2_{nh} (moderate Rossby number) and R^2_{nh} (low Rossby number) in Figs 4.32(e)-(h). In both the moderate and the low Rossby number runs the streamlines are basically divided into two parts, one at large scale with a slope larger than one (corresponding to radial $\boldsymbol{\mathcal{F}}$), the other at smaller scale with a slope smaller than one. However, only the low Rossby number run (R^2_{nh}, Figs 4.32g-h) displays the predicted 4/3 slope in the inertial range, which is consistent with the assumption of rapid rotation of the inertial theory.

We now quantitatively compare the radial and polar components of $\boldsymbol{\mathcal{F}}$ in run S^2_{nh} with the predictions of Galtier's theory. The other rotating runs have similar behaviours. Starting from $r = 0$, where $\boldsymbol{\mathcal{F}} = \mathbf{0}$, $\mathcal{F}_r$ and $\mathcal{F}_\theta$ quickly decrease with r (and their magnitudes increase), as shown in Fig. 4.33(a). Furthermore, at a fixed small scale, $\mathcal{F}_\theta(\theta)$ displays a minimum while $\mathcal{F}_r(\theta)$ monotonically increases with θ (and its magnitude decreases). However, at some point $\mathcal{F}_\theta$ starts to increase and $\mathcal{F}_r(\theta)$ start to flatten. Nevertheless, this dissipative range behaviour persists up to scales significantly larger than the dissipative scale (consider that the vertical

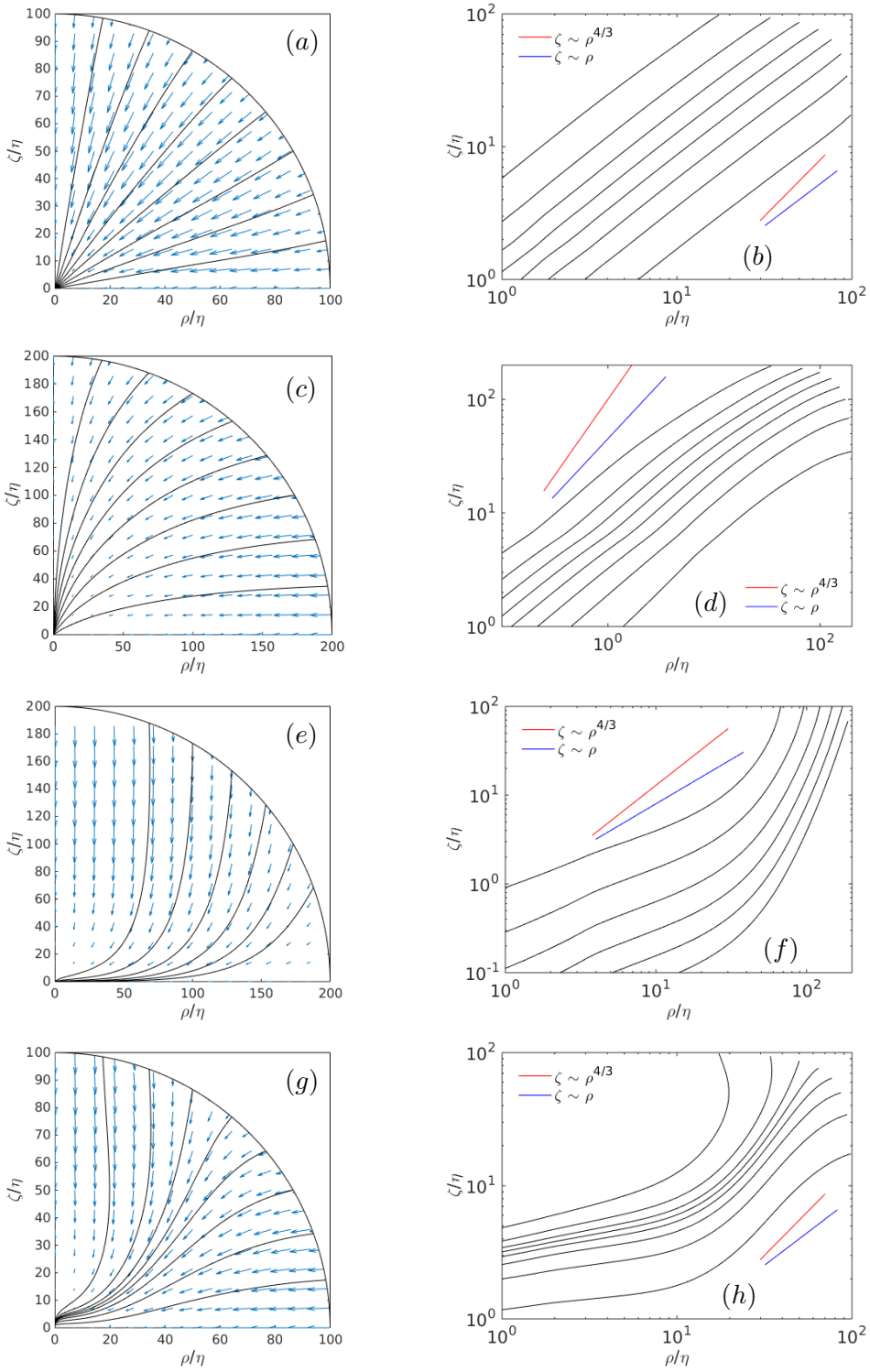

Figure 4.32: Vector field $(\mathcal{F}_r, \mathcal{F}_\theta)$ in the (ρ, ζ) plane, and corresponding streamlines in linear (left panels) and logarithmic (right panels) scale. (a)-(b) run $\mathrm{D_{nv}}$ corresponding to non-rotating turbulence forced through the negative viscosity scheme, (c)-(d) run $\mathrm{A_{nh}}$ corresponding to Euler-forced non-rotating turbulence, (e)-(f) run $\mathrm{S^2_{nh}}$ corresponding to moderate Rossby number rotating turbulence, and (g)-(h) run $\mathrm{R^2_{nh}}$ corresponding to low Rossby number rotating turbulence.

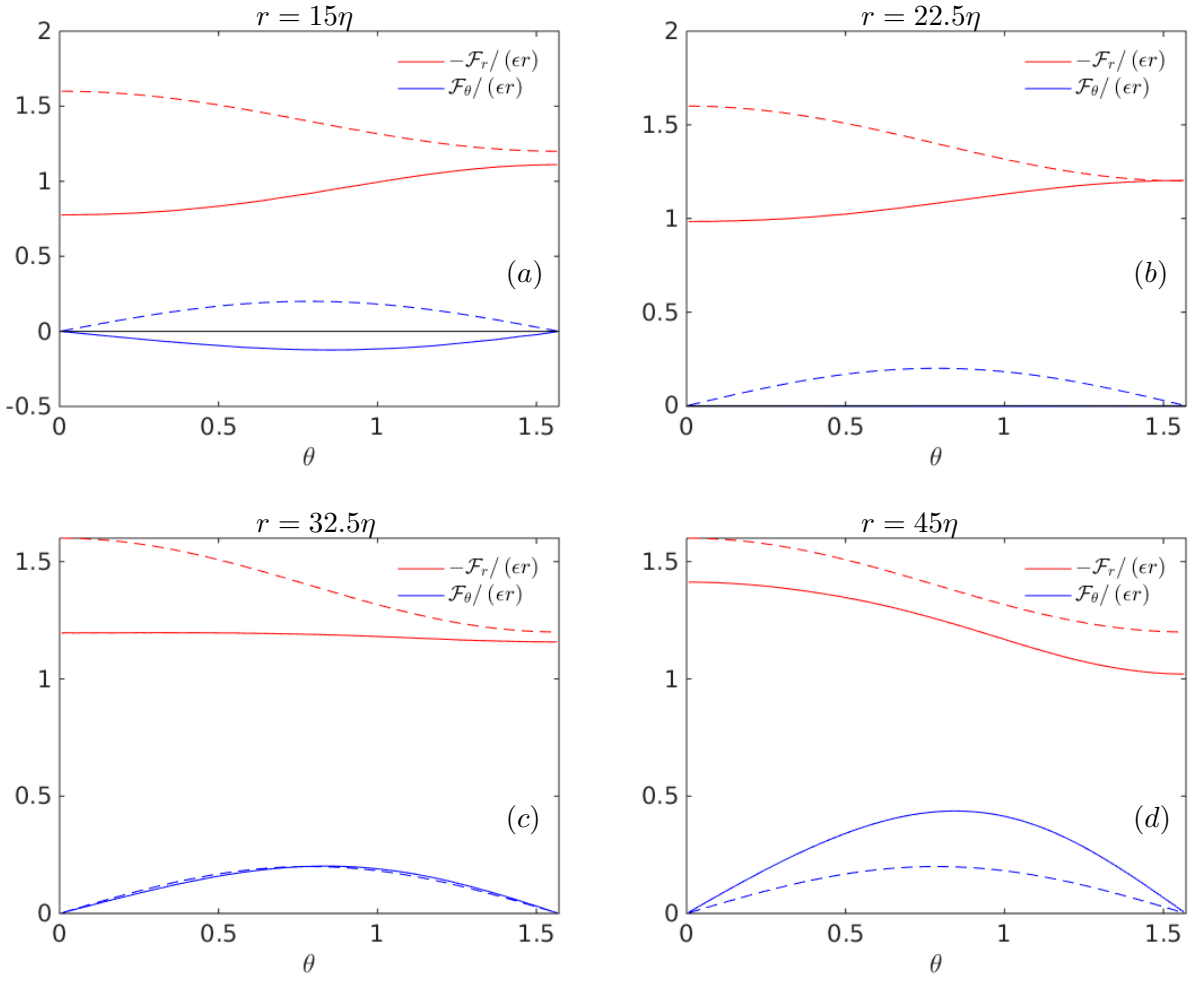

Figure 4.33: Solid lines: radial and polar components of the third-order vector moment $\boldsymbol{\mathcal{F}}$ for run S^2_{nh} (rotating turbulence) as functions of θ at different scales r. (a) $r = 15\eta$; (b) $r = 22.5\eta$; (c) $r = 32.5\eta$; (d) $r = 45\eta$. The dashed lines represent the values predicted by Galtier's inertial theory [30], see also section 1.3.2.

cross-over scale corresponding to Fig. 4.33 is 6.8η). Clearly, these trends ($\mathcal{F}_\theta < 0$, $\mathcal{F}_r$ decreasing with θ) are opposite to those predicted by the inertial theory, suggesting that larger scales need to be considered to observe the inertial behaviour.

In the decaying rotating turbulence experiment by P.-P. Cortet and F. Moisy [21], Fig. 4.19(c), at first sight the vector field $\boldsymbol{\mathcal{F}}$ looks nearly radial, pointing towards the origin. But a closer look shows that a departure from the radial direction appears at small scales, for $r < 10$ mm$\approx 17\eta$, where a deflection towards the rotation axis is observed. This is consistent with the anisotropic dissipative range of the simulations. Unfortunately, the limited large-scale resolution in the experiment does not allow to investigate the inertial prediction.

Returning to the DNS data, Fig. 4.33(b) corresponds to the scale where $\mathcal{F}_\theta(\theta) = 0$. At larger scales $\mathcal{F}_\theta(\theta)$ is positive and displays a maximum. Figure 4.33(c) shows the components of $\boldsymbol{\mathcal{F}}$ at a scale where $\mathcal{F}_\theta$ crosses the theoretical prediction and $\mathcal{F}_r$ is almost constant. At even larger scales $\mathcal{F}_\theta$ keeps increasing and $\mathcal{F}_r(\theta)$ becomes a monotonically increasing function of θ (with a decreasing magnitude), as illustrated in Fig. 4.33(d). The values of $\mathcal{F}_r$ and $\mathcal{F}_\theta$ repeat almost unaltered in the range $40 - 50\eta$. For these inertial scales $\mathcal{F}_r(\theta)$ is only slightly larger than its theoretical prediction, with a maximal relative error of 15%, while $\mathcal{F}_\theta$ is about two times its prediction.

These qualitatively opposed trends at small and large scales in the separation space were observed even in large Rossby number runs (not reported here), confirming the presence of anisotropy even at scales much smaller than the Zeman scale.

In summary, one can again identify a dissipative and an inertial anisotropic range in separation space, similarly to the low-wavenumber high-anisotropy range and the high-wavenumber low-anisotropy range we observed through the spectral analysis of sections 4.4 and 4.3. The features of the third-order vector moment at large-scales are consistent with Galtier's inertial law [30], while the anisotropic characteristics displayed in experiments by P.-P. Cortet and F. Moisy [21] correspond to the anisotropic dissipative range in our DNS data. This explains the apparently conflicting trends between experiments and inertial predictions.

Chapter 5

Scale-dependent anisotropy in the von Kármán flow

In this chapter we investigate scale- and direction-dependent anisotropy of a realistic turbulent flow through the separation space indicators used in Chapter 4 in the context of homogeneous isotropic and rotating turbulence. In particular, we perform confined simulations of the von Kármán flow by coupling our pseudo-spectral code to the penalization method described in Chapter 2. First, we compute the mean velocity field and the fluctuating field in the fluid domain. Then, we investigate second- and third-order two-point statistics from the fluctuating velocity in separation space. We show that anisotropy is present in all the studied distributions, and for the third-order vector moment all the resolved scales are strongly anisotropic. Moreover, depending on the region of the domain and on the investigated quantity, trends typical of rotating turbulence can be observed in the von Kármán flow as well. In particular, vertically elongated structures develop in all the portions of the fluid domain that are studied, while the classical cyclone-anticyclone asymmetry and the two anisotropic ranges described in section 4.6 arise in a part of the domain. This region corresponds to a larger average rotation rate in the mean flow, suggesting that the effect of rotation can overcome mechanisms depending on inhomogeneity.

5.1 Real turbulent flows and von Kármán flow

In Chapters 3 and 4 we studied statistically stationary homogeneous turbulence forced through non-helical and helical spectral forcings. However, these forcing schemes do not represent a specific physical configuration and are rather a model force aimed at feeding turbulence. Fur-

thermore, in most real turbulent flows—even statistically stationary—no external force is present and other mechanisms, like transport and production, directly feed turbulence. Studying real turbulent flows is therefore fundamental to understand the actual features of turbulence in real applications.

Special care must be taken when analyzing real turbulent flows: although they can be statistically stationary (if an energy injection mechanism is present) they are never exactly homogeneous. Indeed homogeneous turbulence simulations are more a research tool aimed at disentangling the effects of turbulence from the effects of boundaries than a precise representation of reality. Because of statistical inhomogeneity, classical Fourier analysis may not be suitable for real turbulence. In practice, if the flow is only weakly inhomogeneous, a spectral analysis would represent a first simple tool useful to extract qualitative conclusions and trends. On the other hand, one can always perform instead an analysis in separation space, like the one described in Chapter 4, although the computed distributions in general depend on the shape and size of the region of the fluid domain selected for the analysis.

We choose to simulate the flow between two counter-rotating disks equipped with blades and enclosed by cylindrical walls, and wish to investigate the features of the generated turbulence far from the walls. This flow is referred to as von Kármán flow, even though it differs from the so-called von Kármán swirling flow [8, 87], in which no blades are present and the rotating disks are infinite. Many experimental studies about the von Kármán flow have been carried out so far (see *e.g.* [57]), and different aspect ratios, blades shapes and numbers of blades have been adopted. However, few numerical works have been devoted to the von Kármán flow. In particular, [9, 10, 62] simulate the unbladed disks configuration. In [67] blades are taken into account but, since they are difficult to represent in numerical codes, their effect on the flow is modeled instead. In [45] and [43] the bladed disks are more realistically represented through an immersed boundary method. For our simulations, we use the same code as [45], in which the penalization method described in section 2.1.3 is implemented.

5.2 Geometry and symmetries of the flow

The turbulence generated in this type of flow also depends on the geometry of the cavity and of the blades. We choose to investigate a counter-rotating configuration with a height-to-radius aspect ratio equal to $H_c/R_c = 1.8$, where R_c is the radius of the cylinder and H_c is the distance between the disks. Every disk has radius equal to $R_d = 0.925R_c$ and is equipped with four

straight blades of height equal to $H_p = 0.2R_c$. The Reynolds number based on the disks' radius and their rotation rate Ω_d is equal to $Re = \frac{R_d^2 \Omega_d}{\nu} = 21490$. The upper disk rotates anticlockwise, while the lower one rotates clockwise. The numerical domain consists of a parallelepiped of size $2\pi \times 2\pi \times 4\pi$, a regular grid of $512 \times 512 \times 1024$ equally spaced nodes is used for the discretization. R_c is equal to 0.9π.

Consider a cylindrical frame (x_ρ,x_φ,x_ζ) with the origin in the center of the considered geometry, *i.e.* on the axis of the cylinder and at the same distance from the two rotors. x_ρ and x_ζ are therefore the distance from the axis of symmetry and the signed distance from the horizontal middle plane. Despite the presence of blades on the disks, we make the hypothesis that sufficiently far from the blades the von Kármán flow is statistically axisymmetric. Furthermore, since in our case the rotors are exactly counter-rotative, the flow possesses another symmetry: it is statistically invariant under a rotation of π radians about any horizontal axis passing through the geometrical center. The mean velocity field $\boldsymbol{U}$ with components U_ρ, U_φ, U_ζ along x_ρ, x_φ, x_ζ therefore possesses the following symmetries:

$$\left[\frac{\partial^{2m}}{\partial x_\rho^{2m}} U_\rho\right]_{\rho=0} = \left[\frac{\partial^{2m+1}}{\partial x_\zeta^{2m+1}} U_\rho\right]_{\zeta=0} = 0 \tag{5.1}$$

$$\left[\frac{\partial^{2m}}{\partial x_\rho^{2m}} U_\varphi\right]_{\rho=0} = \left[\frac{\partial^{2m}}{\partial x_\zeta^{2m}} U_\varphi\right]_{\zeta=0} = 0 \tag{5.2}$$

$$\left[\frac{\partial^{2m+1}}{\partial x_\rho^{2m+1}} U_\zeta\right]_{\rho=0} = \left[\frac{\partial^{2m}}{\partial x_\zeta^{2m}} U_\zeta\right]_{\zeta=0} = 0 \tag{5.3}$$

for $m \geq 0$ (the zero-th order derivatives are included).

In order to limit the effect of inhomogeneity, we use small regions of the domain to average our statistics in space. Since we consider only cylindrical sub-regions centered on the symmetry axis, in separation space we compute distributions only for positive values of ρ and ζ, where ρ and ζ are the components of the separation vector $\boldsymbol{r}$ along x_ρ and x_ζ. Distributions in the (ρ,ζ) plane are averaged in time, space (within the selected cylindrical sub-region in physical space) and along the azimuthal direction in separation space φ.

The mean kinetic energy is plotted in Fig. 5.1 as a function of time normalized by the disks rotation rate, $t\Omega_d$. After less than 50 characteristic times the flow seems to reach a statistically stationary state. The velocity fields analyzed in section 5.4 correspond to times later than $t\Omega_d = 69$.

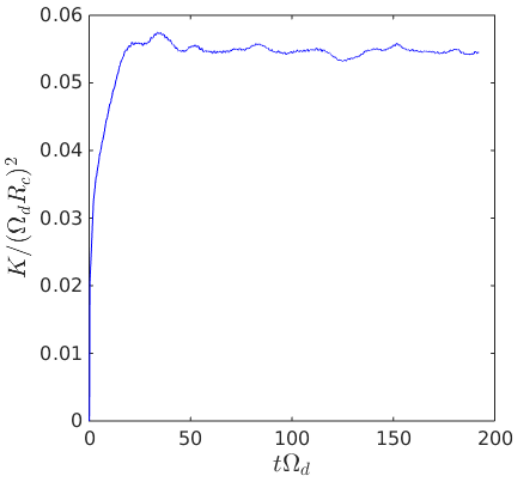

Figure 5.1: Mean kinetic energy normalized by $(\Omega_d R_c)^2$ as a function of time normalized by Ω_d.

5.3 Mean velocity field

Since we are interested in the fluctuating velocity field, the mean velocity field has to be subtracted from the total velocity. We compute the mean flow by space- and time-averaging. 100 velocity fields at 100 times in the interval $69 \leq t\Omega_d \leq 192$ are considered. At every time, space average is computed over four azimuthal directions, $x_\varphi = 0, \pi/2, \pi, 3/2\pi$. For every value of x_φ, we consider the velocity field over the nodes of the numerical grid that fall in the corresponding plane. In order to further improve the estimation of the mean field we also perform a 7th-order polynomial fitting of the three components in the region $x_\rho, x_\zeta \leq 0.45 R_c$, after taking incompressibility and symmetries (5.1)-(5.3) into account.

Figure 5.2 shows the mean velocity in the (x_ρ, x_ζ) plane. As expected from symmetries (5.1)-(5.3), the mean flow is weak near $x_\rho = x_\zeta = 0$. However, U_ζ increases with x_ζ. For small values of x_ρ, U_ρ and U_φ stay weak, although the azimuthal shear $\partial U_\varphi / \partial x_\rho$ increases with x_ζ. For larger values of x_ρ, a strong azimuthal shear develops at $x_\zeta = 0$ and both U_ζ and U_φ increase at large x_ζ.

Once the mean velocity is estimated, we compute the fluctuating field used in the following section to study the anisotropic features of the turbulent flow.

5.4 Scale-dependent anisotropy

Since the von Kármán flow is strongly inhomogeneous we restrict our study to the same analysis performed in separation space for statistically homogeneous rotating turbulence in Chapter 4. One way to show how a direct Fourier projection would affect the velocity field is to compute the

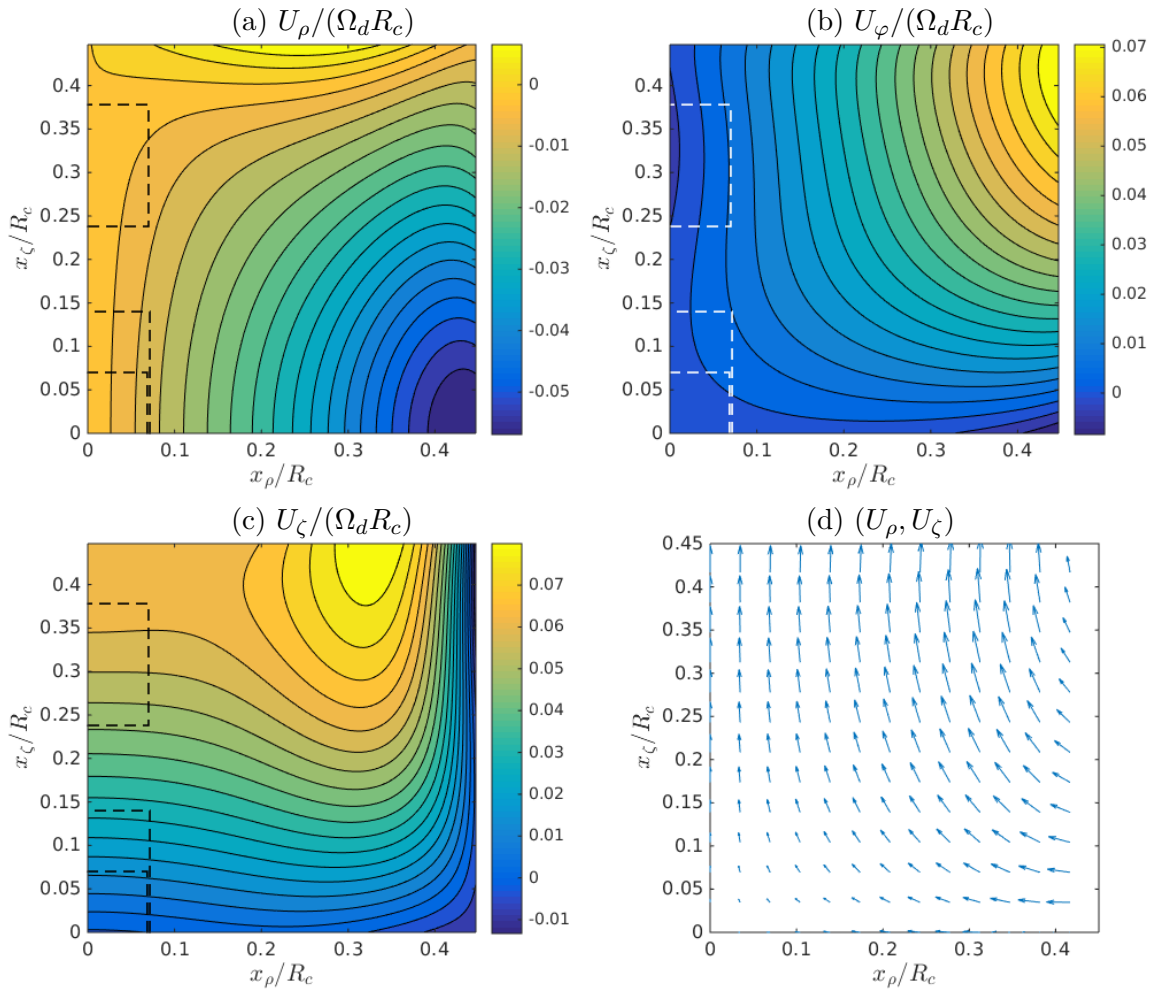

Figure 5.2: Mean velocity field normalized by $\Omega_d R_c$: (a) radial (along x_ρ) component; (b) azimuthal component; (c) axial component; (d) (U_ρ, U_ζ) vector field in the (x_ρ, x_ζ) plane. The dashed lines represent the averaging regions in the fluid domain: the cylinder centered in $x_\rho = x_\zeta = 0$, the cylinder contained in the upper half of the domain with the lower base in the middle pane, and the cylinder contained in the upper half of the domain centered at $x_\zeta = 0.308 R_c$. All the represented cylinders have size equal to $\mathcal{S} = 0.14 R_c$.

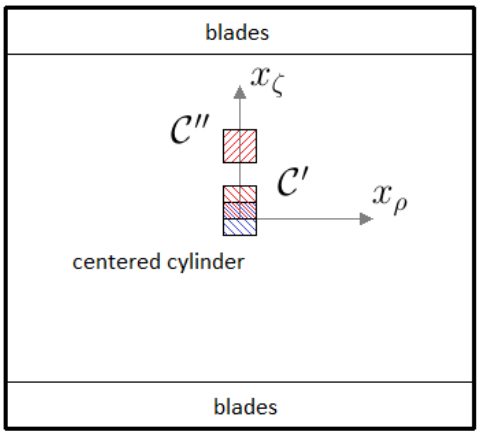

Figure 5.3: Averaging regions in the fluid domain: cylinder centered in $x_\rho = x_\zeta = 0$ (blue lines), and cylinders contained in the upper half of the domain (red lines). All the represented cylinders have size equal to $\mathcal{S} = 0.14R_c$.

same statistics in both spectral and separation space and then to compare the two computations. As an example, we computed the turbulent kinetic energy in a cube of size $0.14R_c$ centered in $x_\rho = x_\zeta = 0$ before and after Fourier projection, and found that 2/3 of the energy gets lost in the operation.

5.4.1 Core region

We consider first a region centered in $x_\rho = x_\zeta = 0$, in particular a cylindrical sub-domain with diameter equal to longitudinal length. This region is represented in Fig. 5.3 (blue lines). As shown by Fig. 5.2, the portion of the domain near the center corresponds to a weak mean flow. Furthermore, in the upper and lower parts of the core region the mean flow has opposite rotation directions, and by symmetry the average rotation rate in the cylinder is zero. Since, as explained in section 5.1, the computed statistics in general depend on the size of the cylinder, we compute the velocity correlation $R(\boldsymbol{r})$, the dissipative term $-\nu\nabla^2 R(\boldsymbol{r})$, the third-order vector moment $\boldsymbol{\mathcal{F}}(\boldsymbol{r})$ and $-\Pi = -\nabla \cdot \boldsymbol{\mathcal{F}}/4$ by spatial averaging in three cylinders of different sizes, $\mathcal{S}/R_c = 0.14, 0.28, 0.56$, where $\mathcal{S}$ is the diameter or the length of the cylinder. For the sake of simplicity we keep the same symbols as in the previous chapters.

Figures 5.4(a)-(c) show the distributions of the viscous term $-\nu\nabla^2 R(\boldsymbol{r})$. The values on the horizontal and vertical axes are slightly affected by numerical error. The maximal value in $\boldsymbol{r} = \boldsymbol{0}$, which we call $\tilde{\epsilon}$, is plotted in Fig. 5.4(d) as a function of the cylinder size and is of the same

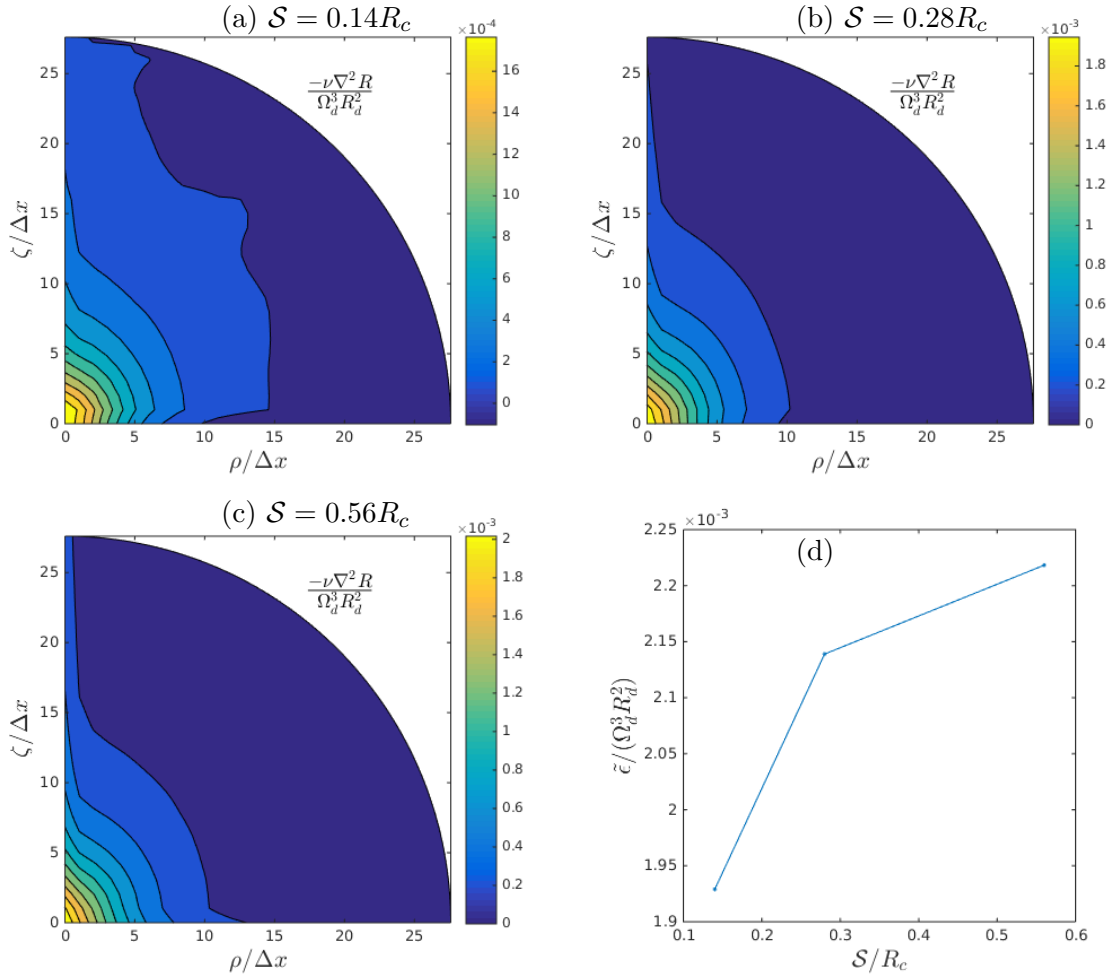

Figure 5.4: $-\nu\nabla^2 R(\boldsymbol{r})$ normalized by $\Omega_d^3 R_d^2$, where Ω_d and R_d are the rotation rate and the radius of the disks, computed in the core of the flow domain. (a) $\mathcal{S} = 0.14R_c$; (b) $\mathcal{S} = 0.28R_c$; (c) $\mathcal{S} = 0.56R_c$; (d) maximal value normalized by $\Omega_d^3 R_d^2$ as a function of the cylinder size normalized by R_c. Δx is the numerical grid resolution.

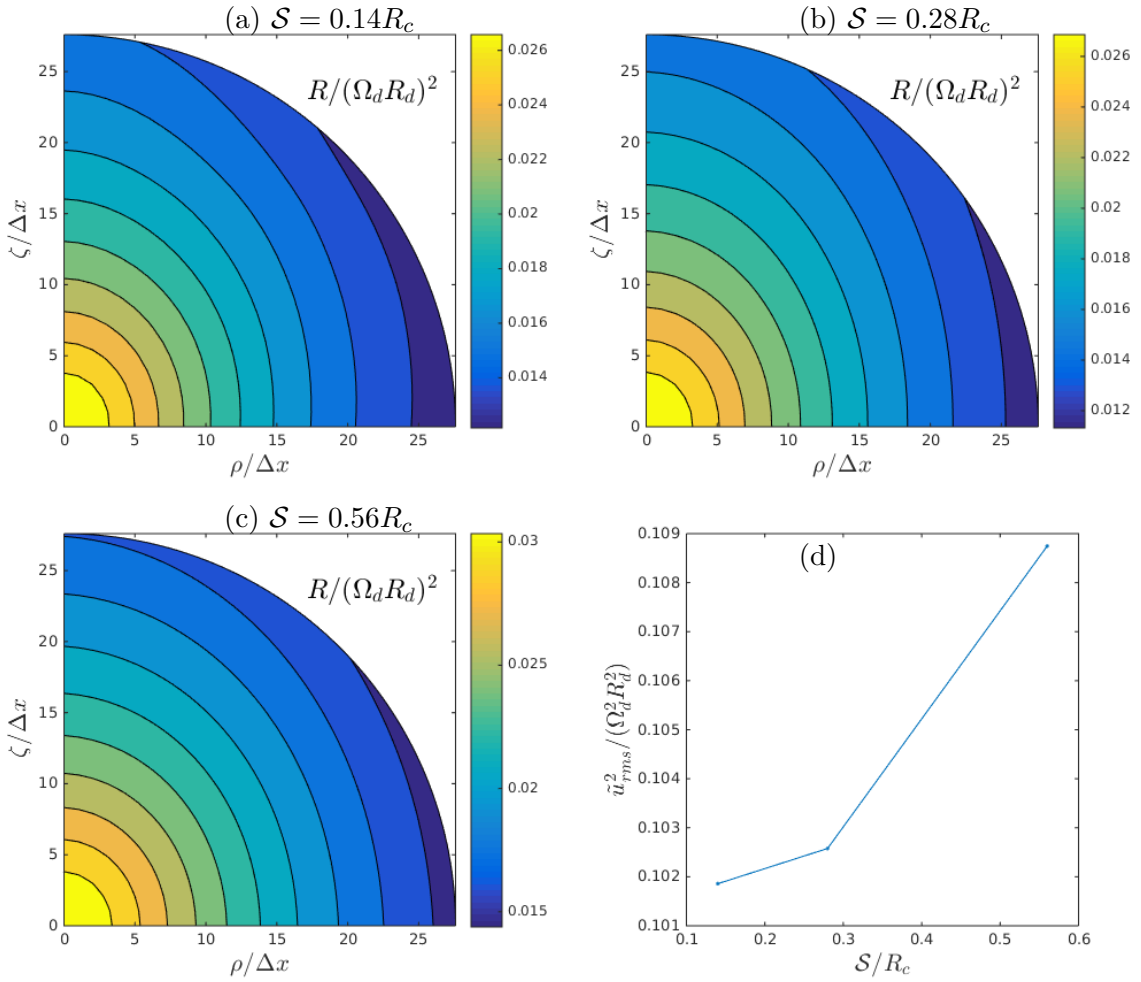

Figure 5.5: Velocity correlation $R(\boldsymbol{r})$ normalized by $\Omega_d^2 R_d^2$, where Ω_d and R_d are the rotation rate and the radius of the disks, computed in the core of the flow domain. (a) $\mathcal{S} = 0.14R_c$; (b) $\mathcal{S} = 0.28R_c$; (c) $\mathcal{S} = 0.56R_c$; (d) $\tilde{u}^2_{\rm rms}$ normalized by $\Omega_d^2 R_d^2$ as a function of the cylinder size normalized by R_c. Δx is the numerical grid resolution.

order for all of the three sizes (13% decrease between $\mathcal{S} = 0.56R_c$ and $\mathcal{S} = 0.14R_c$). Moreover, the qualitative features of the distribution do not depend on the size of the selected region. The isolines are vertically elongated and a trend towards isotropy is observed at decreasing scales, similarly to rotating turbulence (compare with Figs. 4.26b,e), meaning that the viscous term is stronger for smaller θ, *i.e.* along directions closer to the vertical axis. In these figures, at the largest resolved scales, $-\nu\nabla^2 R$ is about 10% of its maximal value, so that only for a small range of the analyzed scales the dissipative term is expected to be negligible with respect to the nonlinear term.

The distributions of $R(\boldsymbol{r})$ and its maximal value in $\boldsymbol{r} = \boldsymbol{0}$, $\tilde{u}^2_{\rm rms}$, are plotted in Fig. 5.5.

Again, there is no evident dependence on the region size for both the distribution and $\tilde{u}^2_{\rm rms}$ (6% decrease between $\mathcal{S} = 0.56R_c$ and $\mathcal{S} = 0.14R_c$). The velocity correlation is systematically stronger at smaller θ, which means that, like in the case of rotating turbulence of Fig. 4.15, vertically elongated structures are present.

The same conclusions about the negligible dependence of the statistics on the cylinder size may be drawn for all the distributions we analyzed (in the range of the resolved scales) except for the nonlinear term $-\Pi = -\nabla \cdot \boldsymbol{\mathcal{F}}/4$. In the rest of this section, apart from $-\Pi$, we will therefore present only the smallest size cases, *i.e.* $\mathcal{S} = 0.14R_c$.

Figure 5.6 displays the distributions of the components of the third-order vector moment $\boldsymbol{\mathcal{F}}(\boldsymbol{r})$, its modulus, and the vector field $(\mathcal{F}_r, \mathcal{F}_\theta)$ in the (ρ, ζ) plane. While for larger θ the radial (along $\boldsymbol{r}$) component $\mathcal{F}_r$ (Fig. 5.6a) is negative, at lower θ $\mathcal{F}_r > 0$. The polar component $\mathcal{F}_\theta$ (Fig. 5.6b) is always negative in the range of displayed scales, and is of the same order as $\mathcal{F}_r$. As expected from the symmetry of the selected region, the azimuthal component (Fig. 5.6c) is less important and reaches about 1/3 of the magnitudes of the other two components only at the very largest scales, where r is of the same order as $\mathcal{S}$ and the statistical convergence error is important. Observing now the behaviour of $\boldsymbol{\mathcal{F}}(\boldsymbol{r})$ in the (ρ, ζ) plane (Fig. 5.6d), for a fixed scale r, at large θ the vector field is almost radial (consistently with the symmetry condition $\mathcal{F}_\theta(\zeta = 0) = 0$) and oriented towards the origin, as usual in isotropic and rotating turbulence at all orientations. However, as θ decreases $\boldsymbol{\mathcal{F}}$ deflects toward the vertical axis, until at some point the radial component becomes positive (the opposite of isotropic and rotating turbulence). $|\boldsymbol{\mathcal{F}}|$ isolines (Fig. 5.6e) are vertically elongated and therefore show that the anisotropic features of the third-order vector moment are also evident in its modulus.

Finally, the distributions of the nonlinear term $-\Pi = -\nabla \cdot \boldsymbol{\mathcal{F}}/4$, which is more sensitive to the cylinder size, are plotted in Fig. 5.7 for different values of $\mathcal{S}$. At smaller scales r, independently of $\mathcal{S}$, $-\Pi$ is smaller (as expected, since $\Pi(\boldsymbol{r} = \boldsymbol{0}) = 0$). Furthermore, the isolines are slightly elongated along the vertical axis with a trend towards isotropy at decreasing scales, similarly to rotating turbulence (compare with Fig. 4.27). At larger scales $-\Pi$ presents a maximum, but the corresponding $\boldsymbol{r}$ is close to the horizontal axis for the larger size cylinder and gradually shifts towards the vertical axis as the region size decreases.

In summary, all the analyzed distributions present anisotropic features, the third-order vector moment being the most anisotropic quantity with strong anisotropy at all resolved scales. Apart from the distributions of R and $\nu\nabla^2 R$, these statistics display anisotropic features strongly different from those of rotating turbulence. This is not surprising, since the mean flow of the

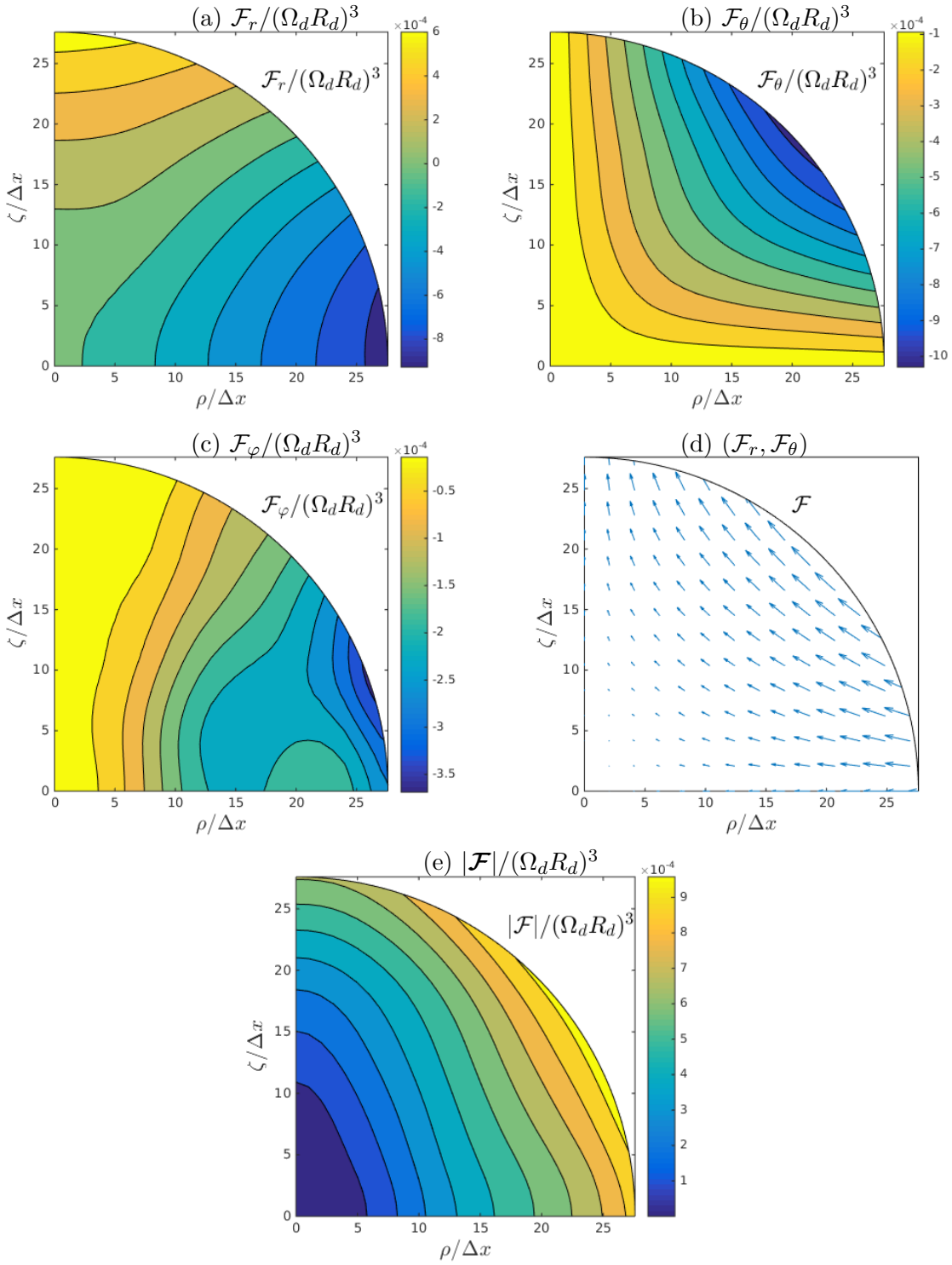

Figure 5.6: Third-order vector moment $\boldsymbol{\mathcal{F}}(\boldsymbol{r})$. (a) radial (along the separation vector $\boldsymbol{r}$) component; (b) polar component; (c) azimuthal component; (d) vector field $(\mathcal{F}_r, \mathcal{F}_\theta)$ in the (ρ, ζ) plane; (e) modulus of $\boldsymbol{\mathcal{F}}$. Δx is the numerical grid resolution.

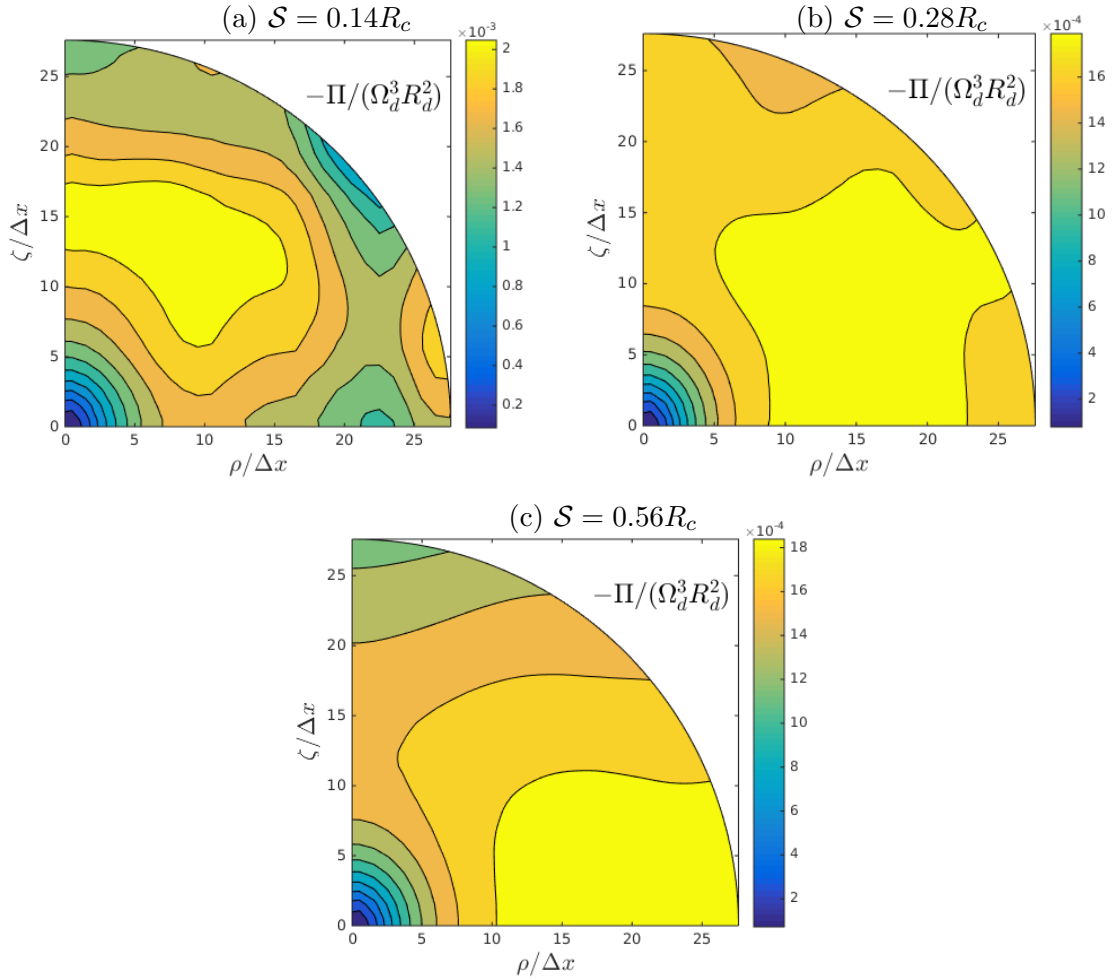

Figure 5.7: Nonlinear term $-\Pi = -\nabla \cdot \boldsymbol{\mathcal{F}}/4$. (a) $\mathcal{S} = 0.14R_c$; (b) $\mathcal{S} = 0.28R_c$; (c) $\mathcal{S} = 0.56R_c$. Δx is the numerical grid resolution.

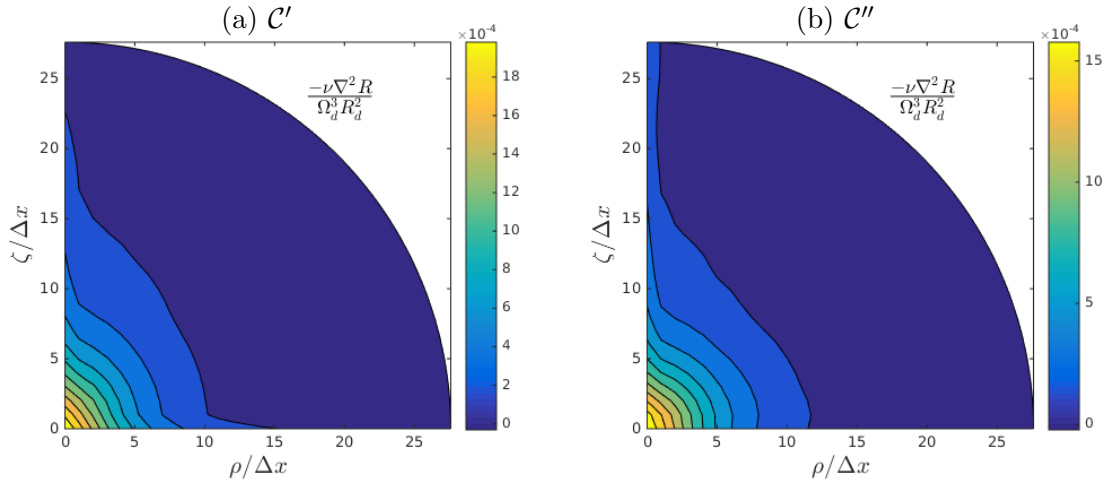

Figure 5.8: $-\nu\nabla^2 R(\boldsymbol{r})$ normalized by $\Omega_d^3 R_d^2$, where Ω_d and R_d are the rotation rate and the radius of the disks, computed in (a) the cylinder $\mathcal{C}'$ (upper half, lower base in the middle plane) and (b) the cylinder $\mathcal{C}''$ (centered in $x_\zeta = 0.308 R_c$). Δx is the numerical grid resolution.

selected portion of the domain (a cylinder centered on both the axis of symmetry and the middle horizontal plane) is far different from a solid body rotation, as displayed in Fig. 5.2. Therefore, if one looks for similarities between the von Kármán flow and homogeneous rotating turbulence, upper regions (with a non-vanishing average rotation rate) should be investigated.

5.4.2 Upper regions

We compute the same statistics in: (i) a cylinder $\mathcal{C}'$ contained in the upper half of the domain, with the lower base lying in the middle plane, and (ii) a cylinder $\mathcal{C}''$ centered at an upper $x_\zeta = 0.308 R_c$. These regions are represented in Fig. 5.3. In $\mathcal{C}''$ the average rotation rate is stronger than in $\mathcal{C}'$. When we show only one distribution for a quantity, the corresponding cylinder has size equal to $\mathcal{S} = 0.14 R_c$, and it has been verified that the qualitative features of the distribution do not depend on the size of the cylinder, even though these features may be more or less important depending on $\mathcal{S}$.

Figures 5.8 and 5.9 show the distributions of $-\nu\nabla^2 R(\boldsymbol{r})$ and $R(\boldsymbol{r})$ computed in $\mathcal{C}'$ and $\mathcal{C}''$. Both the statistics in both the cylinders are similar to the corresponding distribution computed in the perfectly centered cylinder, compare with Fig. 5.4.

Figure 5.10 displays the distributions of the components of $\boldsymbol{\mathcal{F}}(\boldsymbol{r})$, the vector field $(\mathcal{F}_r, \mathcal{F}_\theta)$ in the (ρ, ζ) plane, and $|\boldsymbol{\mathcal{F}}(\boldsymbol{r})|$ computed in the cylinder $\mathcal{C}'$ (upper half, lower base in the middle plane). $\mathcal{F}_\theta$ (Fig. 5.10b) is still negative at all scales, but now $(\mathcal{F}_r, \mathcal{F}_\theta)$ is almost horizontal

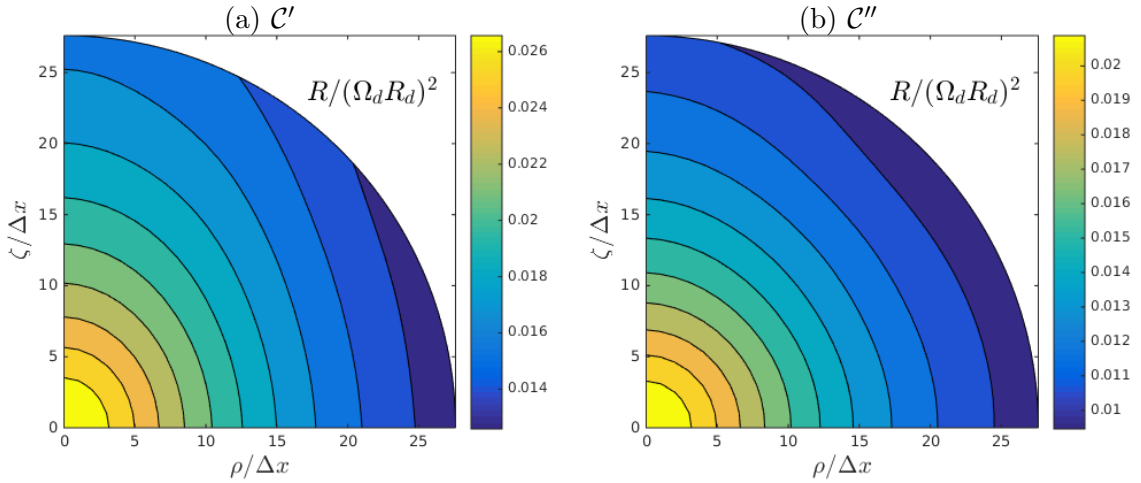

Figure 5.9: Velocity correlation $R(\boldsymbol{r})$ normalized by $\Omega_d^2 R_d^2$, where Ω_d and R_d are the rotation rate and the radius of the disks, computed in (a) the cylinder $\mathcal{C}'$ (upper half, lower base in the middle plane) and (b) the cylinder $\mathcal{C}''$ (centered in $x_\zeta = 0.308 R_c$). Δx is the numerical grid resolution.

and bidimensional (Fig. 5.10a,d,e), with a negative radial component $\mathcal{F}_r$ (Fig. 5.10a). Only at lower ρ, where its magnitude is small, the third-order vector moment deflects towards the origin, as shown in the $\mathcal{F}_\theta$ distribution (Fig. 5.10b). Even though in $\mathcal{C}'$ the azimuthal component does not need to vanish, $\mathcal{F}_\varphi$ is still smaller than the other two components of $\boldsymbol{\mathcal{F}}$, and becomes significantly positive only at the largest resolved scales along large θ directions, after a slight negative minimum.

Some of these features vaguely resemble those of rotating turbulence: the vertically elongated isolines of R and $-\nu\nabla^2 R$, and the third-order vector moment, for which $\mathcal{F}_\theta < 0$, $\mathcal{F}_r < 0$ and decreases with θ, which is similar to the behaviour of the anisotropic dissipative range of rotating turbulence (see section 4.6 and Fig. 4.33a). Nevertheless, the other quantities clearly differ from the rotating turbulence ones and no range with the typical inertial features ($\mathcal{F}_\theta > 0$, $\mathcal{F}_r < 0$ and increasing with θ, Fig. 4.33d) is visible in these figures, not even at the largest scales.

We repeat the same analysis for cylinder $\mathcal{C}''$ (centered in $x_\zeta = 0.308 R_c$, upper than $\mathcal{C}'$ and with a stronger average rotation rate) in Fig. 5.11. Now $\mathcal{F}_\varphi$ (Fig. 5.11c) is clearly positive, it increases with ρ and is only weakly dependent of ζ, exhibiting cyclone-anticyclone asymmetry just like rotating turbulence (compare with Figs. 4.20i,n). The vector field $(\mathcal{F}_r, \mathcal{F}_\theta)$ in the (ρ, ζ) plane (Fig. 5.11d) is mainly radial, with the radial component $\mathcal{F}_r$ (Fig. 5.11a) negative and increasing with θ. As for $\mathcal{F}_\theta$, the negative values are restricted to the smallest scales (although

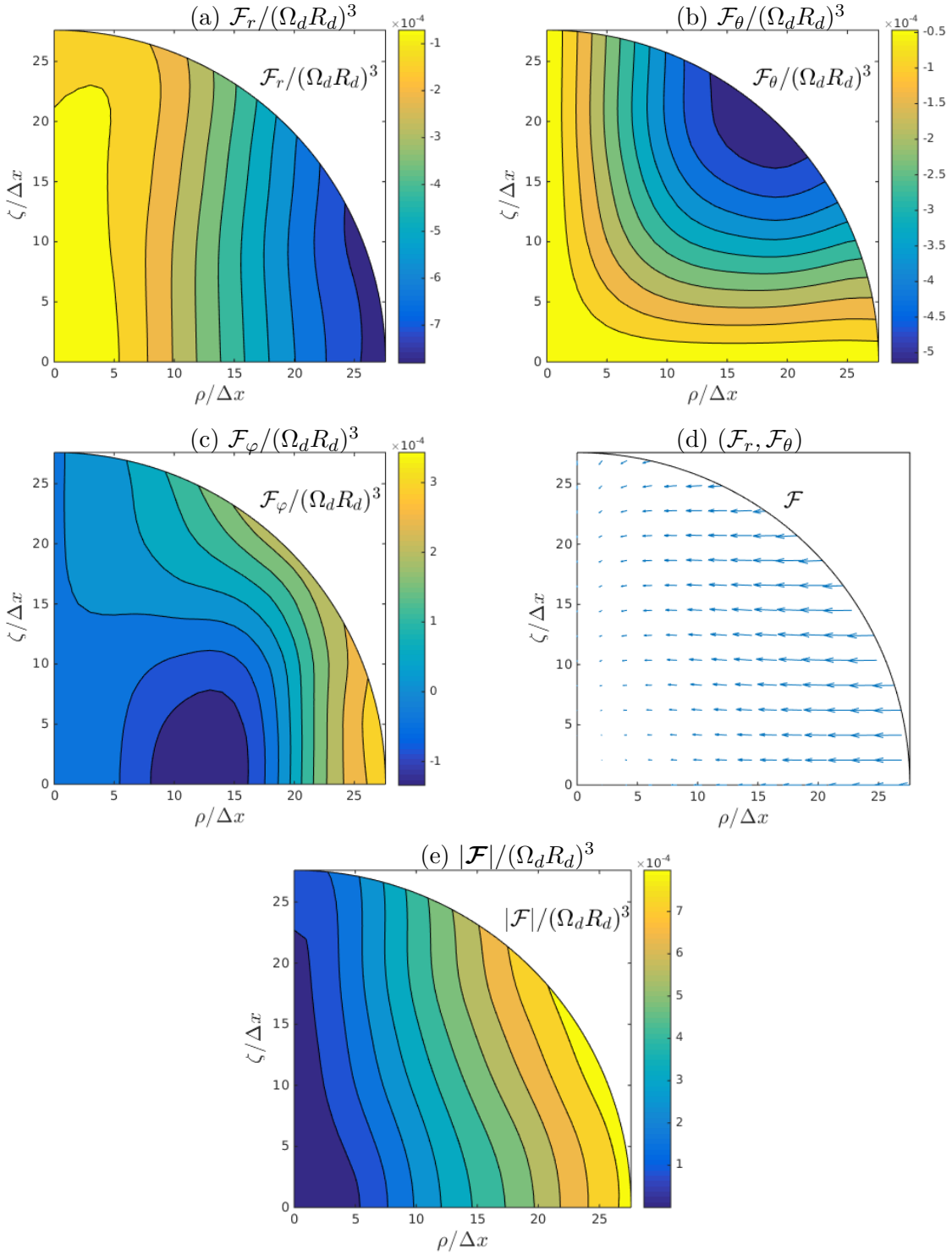

Figure 5.10: Third-order vector moment $\boldsymbol{\mathcal{F}}(\boldsymbol{r})$ computed in the cylinder $\mathcal{C}'$ (upper half, lower base in the middle plane). (a) radial (along the separation vector $\boldsymbol{r}$) component; (b) polar component; (c) azimuthal component; (d) vector field $(\mathcal{F}_r, \mathcal{F}_\theta)$ in the (ρ, ζ) plane; (e) modulus of $\boldsymbol{\mathcal{F}}$. Δx is the numerical grid resolution.

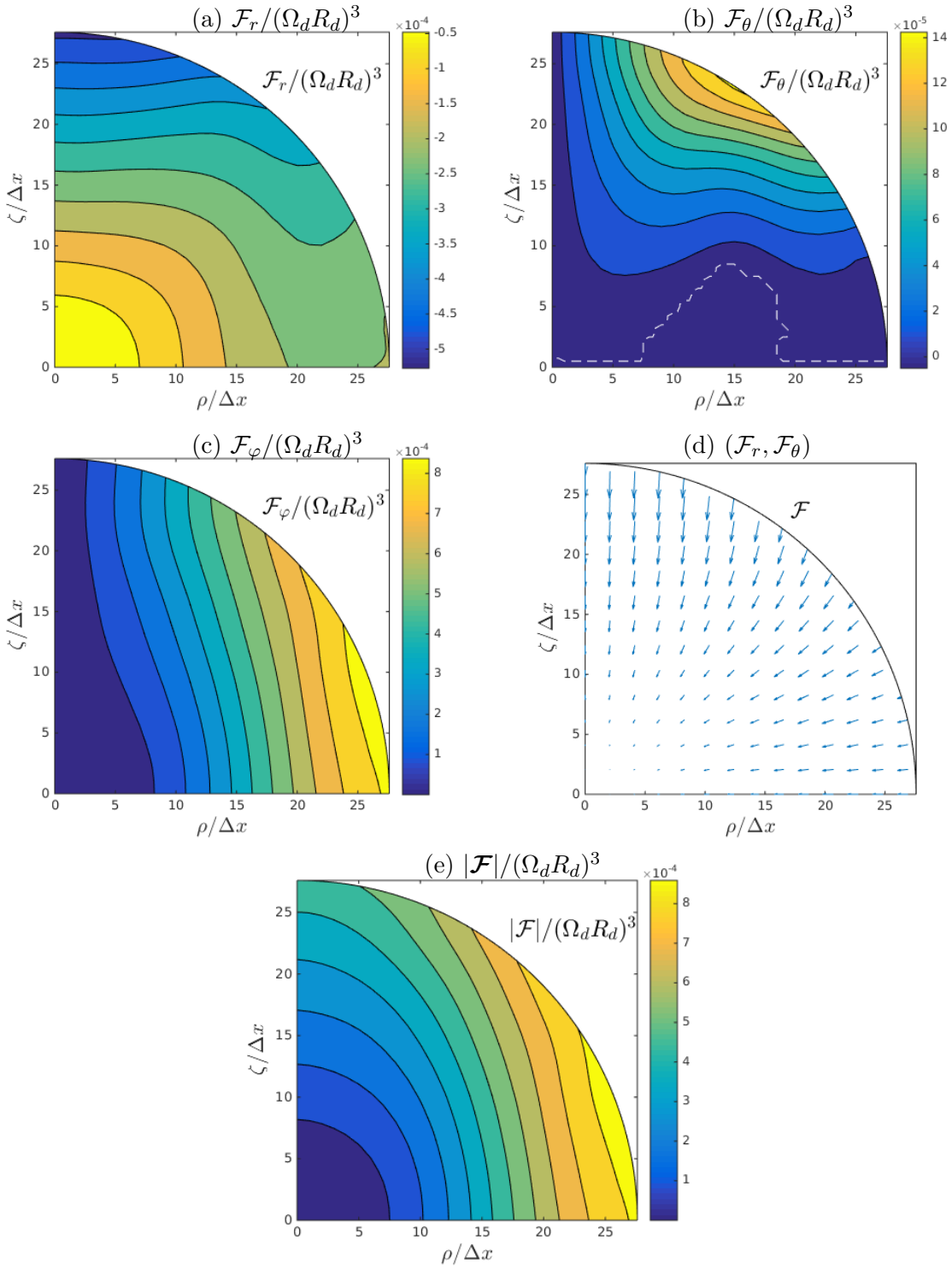

Figure 5.11: Third-order vector moment $\boldsymbol{\mathcal{F}}(\boldsymbol{r})$ computed in the cylinder $\mathcal{C}''$ (centered in $x_\zeta = 0.308R_c$). (a) radial (along the separation vector $\boldsymbol{r}$) component; (b) polar component; (c) azimuthal component; (d) vector field $(\mathcal{F}_r, \mathcal{F}_\theta)$ in the (ρ, ζ) plane; (e) modulus of $\boldsymbol{\mathcal{F}}$. The dashed white line in (b) represents the threshold between negative and positive values. Δx is the numerical grid resolution.

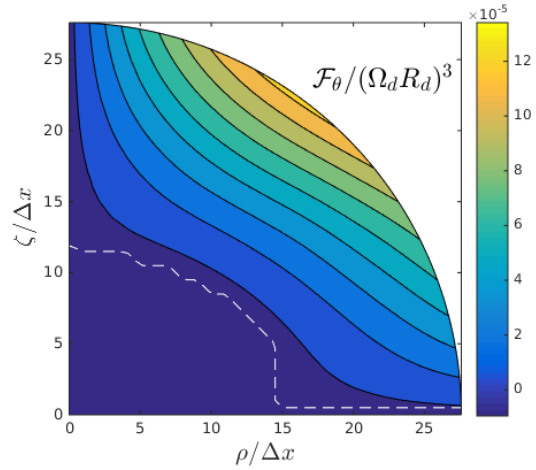

Figure 5.12: Distribution of the polar component of $\boldsymbol{\mathcal{F}}$ computed in the cylinder centered in $x_\zeta = 0.308R_c$ (as $\mathcal{C}''$) but with size $\mathcal{S} = 0.28R_c$ (larger than $\mathcal{C}''$). The dashed white line represents the threshold between negative and positive values. Δx is the numerical grid resolution.

at orientations closer to the horizontal axis) and the large scales display positive values. The dashed white line in Fig. 5.11b represents the threshold between negative and positive values. This behaviour resembles the one already observed for rotating turbulence, with a small-scale negative-$\mathcal{F}_\theta$ range and a large-scale positive-$\mathcal{F}_\theta$ range (Figs. 4.20m and 4.33). The negative values are actually shifted towards larger x_ρ with respect to the rotating turbulence case of Fig. 4.20(m). However, if a larger size cylinder ($\mathcal{S} = 0.28R_c$, but centered in $x_\zeta = 0.308R_c$ like $\mathcal{C}''$) is used, the distribution of $\mathcal{F}_\theta$, plotted in Fig. 5.12, becomes identical to the rotating case. It is not clear if this difference between $\mathcal{S} = 0.14R_c$ and $\mathcal{S} = 0.28R_c$ depends on inhomogeneity or on the lower number of samples used to average in space for the small size case. Also $|\boldsymbol{\mathcal{F}}|$ shows the characteristic anisotropy of rotating turbulence, with isolines elongated in the vertical direction.

The last distributions we plot are the ones of $-\Pi = \nabla \cdot \boldsymbol{\mathcal{F}}/4$, for $\mathcal{C}'$ and $\mathcal{C}''$, in Fig. 5.13. As for the core region, the large scale features in the $-\Pi$ distribution depend on the cylinder size, and are not discussed here. At small scales, the nonlinear term is stronger at lower θ, in opposition with rotating turbulence (compare with Fig. 4.27).

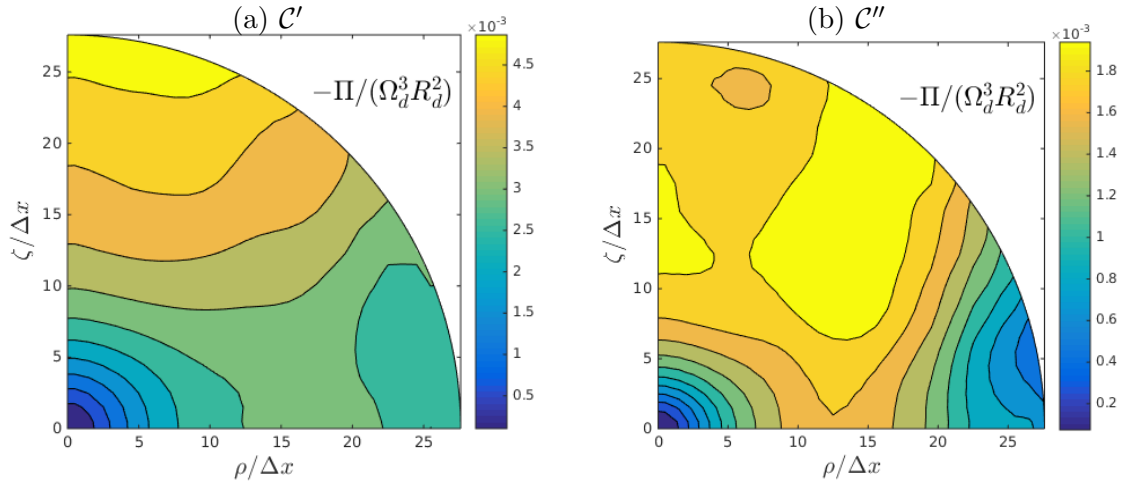

Figure 5.13: Nonlinear term $-\Pi = -\nabla \cdot \boldsymbol{\mathcal{F}}/4$ normalized by $\Omega_d^3 R_d^2$, where Ω_d and R_d are the rotation rate and the radius of the disks, computed in (a) the cylinder $\mathcal{C}'$ (upper half, lower base in the middle plane) and (b) the cylinder $\mathcal{C}''$ (centered in $x_\zeta = 0.308 R_c$). Δx is the numerical grid resolution.

5.5 Conclusions

In conclusion, in the von Kármán flow and for the parameters we chose (geometry, disks rotation rate, viscosity), $R(\boldsymbol{r})$, $-\nu\nabla^2 R(\boldsymbol{r})$, the components of $\boldsymbol{\mathcal{F}}(\boldsymbol{r})$ and $-\Pi(\boldsymbol{r})$ are anisotropic and may display features similar to simple homogeneous rotating turbulence, depending on the region of the domain and on the considered statistics. $-\nu\nabla^2 R(\boldsymbol{r})$ and $R(\boldsymbol{r})$ are stronger at orientations closer to the vertical axis (like in rotating turbulence), no matter the subdomain in which they are computed; $\boldsymbol{\mathcal{F}}(\boldsymbol{r})$ is the most anisotropic quantity, with anisotropy at all scales, and it strongly depends on the region of the domain. In regions closer to the middle horizontal plane its behaviour strongly differs from rotating turbulence trends. However, in upper sub-domains, where the mean flow is closer to a solid body rotation, it shows (i) a positive $\mathcal{F}_\varphi$ increasing with ρ, like in rotating turbulence (Figs. 4.20i,n); (ii) a small scale range with $\mathcal{F}_\theta < 0$ and $\mathcal{F}_r < 0$ decreasing with θ (like in the rotating turbulence dissipative range, Fig. 4.33a), and (iii) a large scale range with $\mathcal{F}_\theta > 0$ and $\mathcal{F}_r < 0$ decreasing with θ (again typical of rotating turbulence, in particular a situation between Fig. 4.33b and Fig. 4.33c). The limited large scale resolution prevents us from checking the existence of a range of the type of Fig. 4.33(d), in which $\mathcal{F}_r$ increases with θ. $-\Pi(\boldsymbol{r})$ is affected by inhomogeneity at large scales, and we restricted our analysis to small scales in its distribution. Surprisingly, $-\Pi(\boldsymbol{r})$ resembles rotating turbulence

in regions closer to the middle horizontal plane (compare Figs. 5.7 and 4.27), while in upper sub-domains its trend is in opposition to rotating turbulence (compare Figs. 5.13 and 4.27).

One possible explanation for the fact that the trends typical of rotating turbulence are observed in some statistics computed in the von Kármán flow, but they are not for others (the nonlinear term $-\Pi$), is that the effect of the average rotation rate in the mean flow can overcome mechanisms depending on inhomogeneity for the formers, while it does not for the statistics more sensitive to inhomogeneity.

Conclusion

In turbulent flows of practical interest, turbulence interacts with confinement and external forces, leading to statistical inhomogeneity and anisotropy. Isolating their contributions to some targeted statistics are the indispensable steps towards the understanding of the underlying physical phenomena. We have chosen in this thesis to focus mainly on the role of anisotropy, and discarded the explicit contribution of inhomogeneity, even in the von Kármán flow. After assessing the anisotropy induced by the forcing of turbulence at large scales, we have introduced a background rotation as seen in several instances of geophysical, astrophysical or industrial flows. We have therefore addressed the question of identifying the detailed anisotropic features specifically induced by the Coriolis force.

The aim of this thesis has therefore been to gain further insight into direction- and scale-dependent anisotropy in a set of idealized and realistic contexts, with the additional objective of contributing to the detailed picture of rotating turbulence which is drawn by existing theoretical, experimental and numerical results. Our original approach has been to use both spectral space and separation space statistical characterizations. The spectral characterization concerns the anisotropic statistics of turbulence under the form of directional energy, polarization and helicity spectra. The separation space characterization is built on two-point second- and third-order velocity increment moments, and two-point velocity correlations. These quantities describe the structure of the flow and its dynamics by two equations: the Lin-type equation for the energy spectral density and the Kármán-Howarth-Monin equation in separation space, the former being the Fourier transform of the latter. Hence, our description of the flow dynamics is rather complete, and we are able to close the balance equations by computing all the terms involved in them. This brings additional information with respect to experimental results. For instance, we have shown that projection in the azimuthal plane of the third-order vector moment causes the loss of important information in the distribution of its divergence, which is the dual of the

energy transfer term in spectral space.

Our systematic careful study of forced rotating turbulence anisotropy has started with an inspection of the effect of large-scale spectral forcing, as a pre-requisite before considering rotation effects. The considered forcing methods are the non-helical and the helical Euler scheme, and the ABC-scheme. Although both were known and employed by previous research groups, we have maybe been first to implement and exploit an Euler scheme in which the range of forced wavenumbers can be chosen in a sphere of arbitrary diameter, and in which the amount of injected helicity can be controlled. We showed that both forcings have a drawback in that, if the number of sufficiently excited modes is too low, anisotropy is bound to arise even at small scales. In the case of Euler forcing, this depends on both the range of forcing wavenumbers and its helicity contents. The ABC forcing, for which the amount of injected helicity cannot be controlled, excites only six modes and therefore always generates anisotropy at all resolved scales. In terms of simulation technique, we conclude from our work that producing isotropic turbulence in pseudo-spectral simulations with spectral forcing has to be considered with care, lest unwanted anisotropy rears its head.

Our second step was to analyze the scale- and direction-dependent anisotropy of homogeneous rotating turbulence. We were confronted with the presence of an inverse cascade in the ABC-forced simulations, which was already found and characterized by [72]. Therefore, ABC-forced rotating simulations should be handled with care since an accumulation of energy in the smallest resolved wavenumbers can occur due to confinement. This energy accumulation does not correspond in general to a real physical phenomenon, since in actual flows such a backscatter of energy can be compensated by other mechanisms dissipating energy or it can feed other fluid motions, for instance a mean flow. We have then focused on Euler-forced simulations, which involve by construction only a forward cascade, the largest-scale dynamics corresponding to an energy conserving system. The cascade of energy towards small scales is ensured by a coupling of the Euler system with the Navier-Stokes equations expressed for larger wavenumbers. Surpringly, anisotropy arises at all scales even at low rotation rate. We have here to be rather specific, so that we identified two anisotropic ranges with different features. In the large scales, directional anisotropy is larger and decreases with wavenumber. At smaller scales, it is much weaker—although still significant—and slowly increases with wavenumber all the way to the dissipative scales. Another interesting and original conclusion of this part of the work concerns the role of the Zeman scale and its link with the flow scale-dependent anisotropy. The Zeman scale was previously argued to be the characteristic lengthscale separating rotation-affected scales

from isotropic ones, so that scales larger than the Zeman one were highly anisotropic under the effect of rotation whereas smaller ones should recover isotropy. Upon closer investigation using several simulations at different parameters, we found that the separating scale between large and weak anisotropy is rather the characteristic lengthscale at which rotation and dissipation effects balance. This conclusion concerns the large Rossby number regime. However, our results do not contradict Zeman's argument about isotropy recovery in the asymptotic limit of vanishing viscosity, since the separating scale vanishes at infinite Reynolds number, and therefore only the decreasing anisotropy range should persist and scales much smaller than the Zeman one may recover isotropy. In other words, the fact that isotropy is not recovered at the smallest resolved scales can possibly be a low Reynold number effect. Of course, higher Reynolds number simulations are called for to investigate this further, but, as for the $-4/5$-th law convergence at increasing Reynolds number, the return to isotropy of forced turbulence may require higher Reynolds numbers than initially thought.

We also investigated the flow dynamics through the dissipative, nonlinear, and forcing terms appearing in the Kármán-Howarth-Monin equation. We therefore plotted distributions in the separation space of all these quantities, thus producing complete axisymmetric maps. The third-order vector moment confirmed the results obtained through the spectral analysis about the presence of anisotropy at all scales and the existence of two qualitatively different anisotropic ranges. We found that the features of the large-scale range are consistent with Galtier's inertial law [30] for the third-order vector moment, while the anisotropic characteristics displayed in experiments by Cortet & Moisy [21] correspond to the anisotropic dissipative range in our DNS data. From a practical point of view, our simulations permitted to confirm the regime achieved in the experiment, and to point out what additional measurements should be considered for a full characterization.

Finally, we considered the von Kármán flow between two counter-rotating bladed disks in a cylindrical cavity. We have chosen this flow because it is widely used in experiments to produce high Reynolds number turbulence, although it is inhomogeneous. We repeated the separation space analysis in different small sub-regions, in order to question the possible analogies in the flow dynamics with that of homogeneous rotating turbulence. The motivation of this is to investigate possible similar mechanisms that could persist in a variety of flow configurations, independently of the specifics of the energy injection mechanism. We found that, in the regions of the domain where the mean flow has a larger average rotation rate, the distributions of the statistics in separation space display some of the features typical of rotating turbulence. In

particular, the velocity correlation is stronger at separations closer to the vertical direction, and the cyclone-anticyclone asymmetry is visible in the azimuthal component of the third-order vector moment. Moreover, the two anisotropic ranges already detected in homogeneous rotating turbulence can be observed as well. This suggests that the mean flow rotation rate can overcome inhomogeneity effects in some regions of the von Kármán flow.

In this work we have found original results about anisotropy in turbulence, both from the point of vue of large scale forcing anisotropy and regarding the effect of rotation. As mentioned, some of the results have to be examined when higher resolution DNS data is available, especially the puzzling phenomenon of persistent anisotropy at the smallest scales. The extension of our preliminary analysis of the von Kármán flow can be envisaged for other more or less inhomogeneous flows. The Kármán-Howarth-Monin equation can be completed with the terms accounting for inhomogeneity, and the computation of the corresponding statistics should be possible from DNS fields.

Bibliography

[1] K. Alvelius. Random forcing of three-dimensional homogeneous turbulence. *Physics of Fluids*, 11(7):1880–1889, 1999.

[2] P. Angot, C.-H. Bruneau, and P. Fabrie. A penalization method to take into account obstacles in incompressible viscous flows. *Numerische Mathematik*, 81(4):497–520, 1999.

[3] R. Antonia and P. Burattini. Approach to the 4/5 law in homogeneous isotropic turbulence. *Journal of Fluid Mechanics*, 550:175–184, 2006.

[4] R. A. Antonia, M. Ould-Rouis, F. Anselmet, and Y. Zhu. Analogy between predictions of Kolmogorov and Yaglom. *Journal of Fluid Mechanics*, 332:395–409, 1997.

[5] E. Arquis and J. Caltagirone. Sur les conditions hydrodynamiques au voisinage d'une interface milieu fluide-milieu poreux: application à la convection naturelle. *CR Acad. Sci. Paris II*, 299:1–4, 1984.

[6] Y. B. Baqui and P. A. Davidson. A phenomenological theory of rotating turbulence. *Physics of Fluids*, 27(2):025107, 2015.

[7] P. Bartello, O. Métais, and M. Lesieur. Coherent structures in rotating three-dimensional turbulence. *Journal of Fluid Mechanics*, 273:1–29, 1994.

[8] G. K. Batchelor. Note on a class of solutions of the navier-stokes equations representing steady rotationally-symmetric flow. *The Quarterly Journal of Mechanics and Applied Mathematics*, 4(1):29–41, 1951.

[9] P. Boronski and L. S. Tuckerman. Poloidal–toroidal decomposition in a finite cylinder. i: Influence matrices for the magnetohydrodynamic equations. *Journal of Computational Physics*, 227(2):1523–1543, 2007.

[10] P. Boronski and L. S. Tuckerman. Poloidal–toroidal decomposition in a finite cylinder: Ii. discretization, regularization and validation. *Journal of Computational Physics*, 227(2):1544–1566, 2007.

[11] W. J. Bos and J.-P. Bertoglio. Dynamics of spectrally truncated inviscid turbulence. *Physics of Fluids*, 18(7):071701, 2006.

[12] W. J. Bos, L. Shao, and J.-P. Bertoglio. Spectral imbalance and the normalized dissipation rate of turbulence. *Physics of Fluids*, 19(4):045101, 2007.

[13] J. G. Brasseur and S. Corrsin. *Spectral Evolution of the Navier-Stokes Equations for Low Order Couplings of Fourier Modes*, pages 152–162. Springer Berlin Heidelberg, Berlin, Heidelberg, 1987.

[14] J. G. Brasseur and P. K. Yeung. Large and small-scale coupling in homogeneous turbulence - Analysis of the Navier-Stokes equation in the asymptotic limit. In *8th Symposium on Turbulent Shear Flows, Volume 1*, volume 1 of *Thin Solid Films*, pages 16–4, 1991.

[15] C. Jause-Labert, F.S. Godeferd and B. Favier. Numerical validation of the volume penalization method in three-dimensional pseudo-spectral simulations. *Computers and Fluids*, 67:41 – 56, 2012.

[16] C. Cambon and L. Jacquin. Spectral approach to non-isotropic turbulence subjected to rotation. *Journal of Fluid Mechanics*, 202:295–317, May 1989.

[17] C. Cambon, N. N. Mansour, and F. S. Godeferd. Energy transfer in rotating turbulence. *J. Fluid Mech.*, 337:303, 1997.

[18] C. Cambon, R. Rubinstein, and F. Godeferd. Advances in wave turbulence: rapidly rotating flows. *New Journal of Physics*, 6(1):73, 2004.

[19] S. Childress and A. D. Gilbert. *Stretch, twist, fold: the fast dynamo*, volume 37 of *Lecture Notes in Physics Monographs*. Springer, 1995.

[20] C. Cichowlas, P. Bonaïti, F. Debbasch, and M. Brachet. Effective dissipation and turbulence in spectrally truncated Euler flows. *Phys. Rev. Lett.*, 95:264502, Dec 2005.

[21] P.-P. Cortet and F. Moisy. Scale-dependent anisotropy in decaying rotating turbulence. *Private communication, unpublished*, 2013.

[22] A. Craya. Contribution à l'analyse de la turbulence associée à des vitesses moyennes. *P. S. T.*, 345, 1958.

[23] S. B. Dalziel. The twists and turns of rotating turbulence. *Journal of Fluid Mechanics*, 666:1–4, 2011.

[24] P. Davidson, P. Staplehurst, and S. Dalziel. On the evolution of eddies in a rapidly rotating system. *Journal of Fluid Mechanics*, 557:135–144, 2006.

[25] A. Delache, C. Cambon, and F. Godeferd. Scale by scale anisotropy in freely decaying rotating turbulence. *Physics of Fluids*, 26(2):025104, 2014.

[26] V. Eswaran and S. B. Pope. An examination of forcing in direct numerical simulations of turbulence. *Comput. Fluids*, 16(3):257–278, June 1988.

[27] B. Favier, F. S. Godeferd, C. Cambon, A. Delache, and W. J. T. Bos. Quasi-static magnetohydrodynamic turbulence at high Reynolds number. *Journal of Fluid Mechanics*, 681:434–461, 2011.

[28] U. Frisch. *Turbulence: The Legacy of A. N. Kolmogorov*. Cambridge University Press, 1995.

[29] B. Gallet, A. Campagne, P.-P. Cortet, and F. Moisy. Scale-dependent cyclone-anticyclone asymmetry in a forced rotating turbulence experiment. *Physics of Fluids*, 26(3):035108, 2014.

[30] S. Galtier. Exact vectorial law for homogeneous rotating turbulence. *Phys. Rev. E*, 80:046301, 2009.

[31] S. Galtier. Kolmogorov vectorial law for solar wind turbulence. *The Astrophysical Journal*, 746(2):184, 2012.

[32] S. Galtier. Theory for helical turbulence under fast rotation. *Phys. Rev. E*, 89:041001, Apr 2014.

[33] F. Godeferd and F. Moisy. Structure and dynamics of rotating turbulence: A review of recent experimental and numerical results. *ASME. Appl. Mech. Rev*, 67(3):030802–030802–13, 2015.

[34] F. S. Godeferd and C. Staquet. Statistical modelling and direct numerical simulations of decaying stably stratified turbulence. Part 2. Large-scale and small-scale anisotropy. *Journal of Fluid Mechanics*, 486:115–159, Jun 2003.

[35] S. Goto and J. Vassilicos. Energy dissipation and flux laws for unsteady turbulence. *Physics Letters A*, 379(16–17):1144 – 1148, 2015.

[36] E. Hopfinger, F. Browand, and Y. Gagne. Turbulence and waves in a rotating tank. *Journal of Fluid Mechanics*, 125:505–534, 1982.

[37] J. Jiménez, A. A. Wray, P. G. Saffman, and R. S. Rogallo. The structure of intense vorticity in isotropic turbulence. *Journal of Fluid Mechanics*, 255:65–90, Oct 1993.

[38] Y. Kaneda and T. Ishihara. High-resolution direct numerical simulation of turbulence. *Journal of Turbulence*, 7:N20, 2006.

[39] A. N. Kolmogorov. Dissipation of energy in locally isotropic turbulence. *Proceedings of the Royal Society of London A: Mathematical, Physical and Engineering Sciences*, 434(1890):15–17, 1991.

[40] A. N. Kolmogorov. The local structure of turbulence in incompressible viscous fluid for very large reynolds numbers. *Proceedings of the Royal Society of London A: Mathematical, Physical and Engineering Sciences*, 434(1890):9–13, 1991.

[41] D. Kolomenskiy and K. Schneider. A Fourier spectral method for the navier–stokes equations with volume penalization for moving solid obstacles. *Journal of Computational Physics*, 228(16):5687–5709, 2009.

[42] R. H. Kraichnan. Helical turbulence and absolute equilibrium. *Journal of Fluid Mechanics*, 59(4):745–752, 1973.

[43] S. Kreuzahler, D. Schulz, H. Homann, Y. Ponty, and R. Grauer. Numerical study of impeller-driven von karman flows via a volume penalization method. *New J. Phys.*, 16:103001, 2014.

[44] S. Kurien. *Anisotropy and the universal properties of turbulence.* PhD thesis, Yale University, 2001.

[45] C. J. Labert. *Simulation numérique d'écoulements turbulents en rotation, confinement et forçage à l'aide d'une méthode de pénalisation.* PhD thesis, Ecole Centrale de Lyon, 2012.

[46] C. Lamriben, P.-P. Cortet, and F. Moisy. Direct measurements of anisotropic energy transfers in a rotating turbulence experiment. *Phys. Rev. Lett.*, 107:024503, Jul 2011.

[47] M. Lighthill. *An Introduction to Fourier Analysis and Generalised Functions*. Cambridge University Press, 1958.

[48] J. L. Lumley and G. R. Newman. The return to isotropy of homogeneous turbulence. *Journal of Fluid Mechanics*, 82(1):161–178, Aug 1977.

[49] J. Mathieu and J. Scott. *An Introduction to Turbulent Flow*. Cambridge University Press, 2000.

[50] M. Meldi and P. Sagaut. Turbulence in a box: quantification of large-scale resolution effects in isotropic turbulence free decay. *Journal of Fluid Mechanics*, 818:697–715, 2017.

[51] P. D. Mininni, A. Alexakis, and A. Pouquet. Non-local interactions in hydrodynamic turbulence at high reynolds numbers: the slow emergence of scaling laws. *Phys. Rev. E*, 77:036306, 2008.

[52] P. D. Mininni and A. Pouquet. Helicity cascades in rotating turbulence. *Phys. Rev. E*, 79:026304, Feb 2009.

[53] P. D. Mininni, D. Rosenberg, and A. Pouquet. Isotropization at small scales of rotating helically driven turbulence. *Journal of Fluid Mechanics*, 699:263–279, 005 2012.

[54] H. K. Moffatt. The degree of knottedness of tangled vortex lines. *Journal of Fluid Mechanics*, 35(1):117–129, 01 1969.

[55] H. K. Moffatt and A. Tsinober. Helicity in laminar and turbulent flow. *Annual Review of Fluid Mechanics*, 24(1):281–312, 1992.

[56] F. Moisy, C. Morize, M. Rabaud, and J. Sommeria. Decay laws, anisotropy and cyclone–anticyclone asymmetry in decaying rotating turbulence. *Journal of Fluid Mechanics*, 666:5–35, 2011.

[57] R. Monchaux, P.-P. Cortet, P.-H. Chavanis, A. Chiffaudel, F. Daviaud, P. Diribarne, and B. Dubrulle. Fluctuation-dissipation relations and statistical temperatures in a turbulent von kármán flow. *Physical review letters*, 101(17):174502, 2008.

[58] A. Monin and A. Yaglom. *Statistical fluid mechanics*. M.I.T. Press, Cambridge, 1975.

[59] C. Morize, F. Moisy, and M. Rabaud. Decaying grid-generated turbulence in a rotating tank. *Physics of fluids*, 17(9):095105, 2005.

[60] A. Naso. Cyclone-anticyclone asymmetry and alignment statistics in homogeneous rotating turbulence. *Physics of Fluids*, 27(3):035108, 2015.

[61] A. Naso and F. S. Godeferd. Statistics of the perceived velocity gradient tensor in a rotating turbulent flow. *New Journal of Physics*, 14(12):125002, 2012.

[62] C. Nore, L. Tuckerman, O. Daube, and S. Xin. The 1 [ratio] 2 mode interaction in exactly counter-rotating von kármán swirling flow. *Journal of Fluid Mechanics*, 477:51–88, 2003.

[63] S. A. Orszag and G. S. Patterson. Numerical simulation of three-dimensional homogeneous isotropic turbulence. *Phys. Rev. Lett.*, 28:76–79, Jan 1972.

[64] C. Peskin. Flow patterns around heart valves: a numerical method. *J. Comput. Phys.*, 10(2):252–271, 1972.

[65] C. Peskin. Numerical analysis of blood flow in the heart. *J. Comput. Phys.*, 25(3):220–252, 1977.

[66] R. Peyret. *Spectral methods for incompressible viscous flow*, volume 148. Springer Science & Business Media, 2013.

[67] S. Poncet, R. Schiestel, and R. Monchaux. Turbulence modeling of the von kármán flow: viscous and inertial stirrings. *International Journal of Heat and Fluid Flow*, 29(1):62–74, 2008.

[68] A. Pumir. A numerical study of pressure fluctuations in three-dimensional, incompressible, homogeneous, isotropic turbulence. *Physics of Fluids*, 6(6):2071–2083, 1994.

[69] A. Pumir. Turbulence in homogeneous shear flows. *Phys. Fluids*, 8:3112, 1996.

[70] A. Pumir and B. I. Shraiman. Persistent small scale anisotropy in homogeneous shear flows. *Phys. Rev. Lett.*, 75:3114, 1995.

[71] L. F. Richardson. *Weather prediction by numerical process*. Cambridge University Press, 2007.

[72] D. L. Rosenberg, R. Marino, P. Mininni, and A. Pouquet. Inverse energy cascades in rotating turbulence. In *Proceedings*, number abstract NG14A-02 in Fall Meeting. American Geophysical Union, 2013.

[73] P. Sagaut and C. Cambon. *Homogeneous Turbulence Dynamics:*. Cambridge University Press, Jun 2008.

[74] X. Shen and Z. Warhaft. The anisotropy of the small scale structure in high Reynolds number ($R_\lambda \sim 1000$) turbulent shear flow. *Phys. Fluids*, 12:2976, 2000.

[75] P. Staplehurst, P. Davidson, and S. Dalziel. Structure formation in homogeneous freely decaying rotating turbulence. *Journal of Fluid Mechanics*, 598:81–105, 2008.

[76] N. P. Sullivan, S. Mahalingam, and R. M. Kerr. Deterministic forcing of homogeneous, isotropic turbulence. *Physics of Fluids*, 6(4):1612–1614, 1994.

[77] B. Thornber. Impact of domain size and statistical errors in simulations of homogeneous decaying turbulence and the richtmyer-meshkov instability. *Physics of Fluids*, 28(4):045106, 2016.

[78] L. Van Bokhoven, C. Cambon, L. Liechtenstein, F. S. Godeferd, and H. Clercx. Refined vorticity statistics of decaying rotating three-dimensional turbulence. *Journal of Turbulence*, (9):N6, 2008.

[79] J. Vassilicos. *Dissipation in Turbulent Flows*, pages 95–114. ANNUAL REVIEWS, 2015.

[80] A. Vincent and M. Meneguzzi. The spatial structure and statistical properties of homogeneous turbulence. *J. Fluid Mech.*, 225:1–20, 1991.

[81] F. Waleffe. Inertial transfers in the helical decomposition. *Physics of Fluids A: Fluid Dynamics*, 5(3):677–685, 1993.

[82] J. D. Woods. Diffusion due to fronts in the rotation sub-range of turbulence in the seasonal thermocline. *La Houille Blanche*, 29:589–597, 1974.

[83] P. Yeung and Y. Zhou. Numerical study of rotating turbulence with external forcing. *Physics of Fluids*, 10(11):2895–2909, 1998.

[84] P. K. Yeung and J. G. Brasseur. The response of isotropic turbulence to isotropic and anisotropic forcing at the large scales. *Physics of Fluids A: Fluid Dynamics*, 3(5):884–897, 1991.

[85] P. K. Yeung, J. G. Brasseur, and Q. Wang. Dynamics of direct large–small scale couplings in coherently forced turbulence: concurrent physical- and Fourier-space views. *Journal of Fluid Mechanics*, 283:43–95, Jan 1995.

[86] K. Yoshimatsu, M. Midorikawa, and Y. Kaneda. Columnar eddy formation in freely decaying homogeneous rotating turbulence. *Journal of Fluid Mechanics*, 677:154–178, 2011.

[87] P. Zandbergen and D. Dijkstra. Von kármán swirling flows. *Annual review of fluid mechanics*, 19(1):465–491, 1987.

[88] O. Zeman. A note on the spectra and decay of rotating homogeneous turbulence. *Phys. Fluids*, 6:3221, 1994.